

Synthesis and characterization of multiwall carbon nanotube reinforced yttria stabilized zirconia composites

Soukaina Lamnini

Ph. D. dissertation

Supervisors:

Dr. Csaba Balázs

Dr. Katalin Balázs



Óbudai Egyetem

Doctoral School of Materials
science and technology
Óbuda University

Thin Film Physics Department
Institute of Technical Physics and Materials Science
Centre for Energy Research

Budapest, 2020

Acknowledgement

This work was performed with the support of numerous people i want to acknowledge hereby:

First and foremost, I would like to express my deepest gratitude to my dear supervisors: **Dr. Katalin Balázs**i, Head of Thin Film Physics Department, and **Dr. Csaba Balázs**i, Scientific advisor in the Centre for Energy Research, for welcoming me in their laboratory and awarding me the great opportunity to work under their supervision. I greatly appreciate the freedom you have always given me to find my own path and the support you offered me when needed. Thanks for your precious help, advices in attaining the established objectives, as well as for the fruitful discussions during my PhD work.

Many thanks goes to **Dr. Judit Borsa**, from the Doctoral School of Material Science and Technologies at Óbuda University for her remarkable kindness, human qualities and for facilitating all difficulties related to administrative works during my PhD studies.

I am thankful to the Director General of EK, **Dr. Ákos Horváth** and Director of MFA, **Dr. Béla Pécz** for all the opportunities and support through these years.

My thanks also go to **Viktor Varga**, **Andor Kovács**, **Tamás Zagyva**, **Levente Illés**, **Dr. Sára Tóth**, **Dr. Eszter Bódis**, **Dr. Zsolt Horváth Endre**, **Dr. Zoltán Károly**, **Dr. Zsolt Fogarassy** and **Dr. Radnóczy György Zoltán**, for their valuable collaboration and technical assistance to perform the different characterization analysis and measurements.

I would further like to thank my pervious professors, **Pr. Mohamed Regragui** and **Pr. Jamal Sebbani** from **University Mohammed V-Morocco**, whom have taught me a lot in science which allowed me to develop myself as a researcher in the best possible way.

Finally, I am grateful to Ministry of Education and Culture of Hungary (Tempus Public Foundation) for the financial support.

Dedications

I dedicate this dissertation to my dear father and beloved mother who have always supported and encouraged me.

I undoubtedly could not have done this without you.

To my dear brothers and whole family members for all the blessed and cheerful moments we have spent together.

To my dear and lovely nephew Mohamed Majd.

To all my dear friends and all peoples who know me.

Table of Content

List of Acronymes.....	7
1. INTRODUCTION.....	7
2. LITERATURE OVERVIEW.....	8
2.1 Ceramic Matrix Composites.....	8
2.2 Zirconia based ceramics.....	11
2.2.1. Phase diagram of zirconia.....	12
2.2.2 Transformation toughening zirconia.....	13
2.2.3. Ionic conductivity of yttria stabilized zirconia (YSZ).....	15
2.3 Carbon nanotubes (CNT).....	16
2.3.1 Synthesis of CNTs.....	19
2.4. Powders processing techniques.....	21
2.4.1 Dispersion of MWCNT into YSZ matrix using ball milling technique.....	21
2.4.2 Spark plasma sintering (SPS).....	23
2.5 Mechanical behaviour of ceramic matrix composites (CMC).....	27
2.5.1 Stress strain-curves of pure ceramics via CMC.....	27
2.5.2 Ceramic matrix composites: challenges.....	29
2.5.3 Fracture toughness of ceramic composites.....	30
2.5.4 Hardness of ceramic composites.....	30
2.5.5 Indentation fracture toughness of ceramic composites.....	32
2.5.6 Vickers indentation fracture toughness of ceramic composites.....	34
2.6 Tribological properties of ceramic matrix composites.....	36
2.7 Application of yttria stabilized zirconia in energy sector.....	38
2.8. Aim of PhD work.....	42
3. MATERIALS and EXPERIMENTS.....	44
3.1 Materials.....	44
3.2 Powder milling and sintering.....	45
3.3 Microstructural analysis, density and porosity measurements.....	48
3.4 Mechanical and tribological testing methods.....	49
3.4.1 Vickers hardness and indentation fracture toughness.....	49

3.4.2 Bending strength.....	50
3.4.3 Wear test.....	52
3.5. Structural characterization of samples	53
3.5.1 Scanning electron microscopy.....	53
3.5.2 Transmission electron microscopy	55
3.5.3 Digital microscopy	56
3.6. Phase analysis of samples	57
3.6.1 X-Ray Diffraction.....	57
3.6.2 Raman spectroscopy	59
4. RESULTS.....	60
4.1 Structural properties of the milled 8YSZ / MWCNTs powders.....	60
4.1.1 Structural study of the as-received 8YSZ powder before and after milling	60
4.1.2 Structural analysis of 8YSZ reinforced MWCNT powder after milling process	62
4.1.3 Phase analysis of 8YSZ / MWCNTs milled powders	66
4.2 Structural properties of the milled and sintered 8YSZ / MWCNTs composites.....	68
4.2.1. Density and microstructure of the sintered 8YSZ / MWCNTs composites	68
4.2.2. Phase analyses of 8YSZ / MWCNTs sintered composites.....	71
4.2.3. Stability of MWCNTs in 8YSZ sintered composites	72
4.2.4 Conclusion.....	74
4.3. Mechanical properties of the sintered 8YSZ / MWCNTs composites.....	76
4.3.1. Crack propagation modes and toughening mechanisms in the sintered 8YSZ/MWCNTs composites.....	76
4.3.2 Vickers hardness and indentation fracture toughness measurements of the sintered 8YSZ / MWCNTs composites.....	79
4.3.3 Microstructure and fractographic test of the sintered 8YSZ / MWCNTs composites	81
4.3.4 Conclusion.....	85
4.4 Wear mechanism of sintered MWCNTs reinforced zirconia composites under dry sliding conditions	86
4.4.1. Average friction coefficient and wear rate	86
4.4.2 Wear (W) damage mechanism	89
4.4.3 Elemental composition of wear track in 8YSZ / MWCNT composites	94
4.4.4 Conclusion.....	97
5. GENERAL CONCLUSION.....	98

6. THESIS.....	99
7. PUBLICATIONS	101
7.1 Publications related to the thesis	101
7.2 Other publications.....	101
7.3 Conferences	101
8. REFERENCES	103

List of Acronyms

8YSZ	8 mol % yttria-stabilized zirconia
CNB	Chevron notched beam
CNFs	carbon nanofiber
CNPs	graphene nanoplatelets
CTE	thermal expansion coefficient
CVD	chemical vapor deposition
EDS	energy-dispersive spectroscopy
FCC	face centred cubic
FSZ	fully stabilized zirconia
IFT	indentation fracture toughness
MWCNTs	multiwall carbon nanotubes
PSZ	partially stabilized zirconia
Ra	average arithmetic roughness
RGO	reduced graphene oxide
SEM	scanning electron microscopy
SENB	single edge notched beam
SEVNB	single edge V-notched beam
SOFC	solid oxide fuel cells
SPS	spark plasma sintering
SWCNTs	single wall carbon nanotubes
TBCs	thermal barrier coatings
TEM	transmission electron microscopy
TPB	triple phase boundary
TZP	tetragonal zirconia polycrystal
VIFT	Vickers indentation fracture toughness
vol. %	volume percentage
wt. %	weight percentage
XRD	X-ray diffraction

1. INTRODUCTION

Zirconia (ZrO_2) based composites are one of the most promising ceramic materials with possible applications in diver fields related to energy sector (in solid oxide fuel cells, oxygen sensors, ceramic membrane oxygen separation technology i.e.) or in the field of tribology and mechanical engineering (cutting tools, bearings, nozzle, brakes, i.e.).

Nowadays, MWCNT reinforced ZrO_2 composites are attracting growing interest, thanks to their ability of crack self-healing and the possibility to tailor the desired nanostructured properties. However, although the expansive interest in the research and development of ceramic composites with nano-fillers, only a very few new technologies and novel processing techniques have been discovered and properly implemented. Further, the clear understanding of the wear response and tribological features such as wear mechanism, friction and wear rates evaluation has been not yet achieved or well documented in the literature.

Therefore, to get a deep insight into their behaviour and to completely benefit from their outstanding properties a deep understanding of the material's behaviour across length scales is required. Principally, the relationship between composition and preparation, and the composite's microstructure and its mechanical and tribological properties should be thoroughly investigated.

2. LITERATURE OVERVIEW

2.1 Ceramic Matrix Composites

Due to their great potential and unique properties, ceramic matrix composites (CMCs) afford a new generation of technical applications with excellent efficiency. Typical applications are designed to withstand severe environment and to increase the worldwide clean energy demand. In fact, CMCs are extensively used for electrical energy generation either as an electrochemical power devices or as a thermal barrier coating in engines. In addition, CMCs are known to be robust, lightweight and highly wear resistant, which make them a proper material in automotive applications (oxygen sensors, brake systems), aerospace engineering (hot structures) and remarkable tribological applications [1–3] .

Ceramics and their composites have shown a great advance in most of tribological applications and have replaced metals and conventional materials such as grey cast iron or carbon/carbon composites used in the fabrication of brake systems. High wear resistance allied with a low friction coefficient are desirable for reducing the losses in moving of the rotating parts and increasing the lifetime of the components respectively. A wide range of factors influence the wear properties of ceramic composites namely applied load, sliding speed, time of contact, temperature, lubrication and surface characteristics such as: composition and

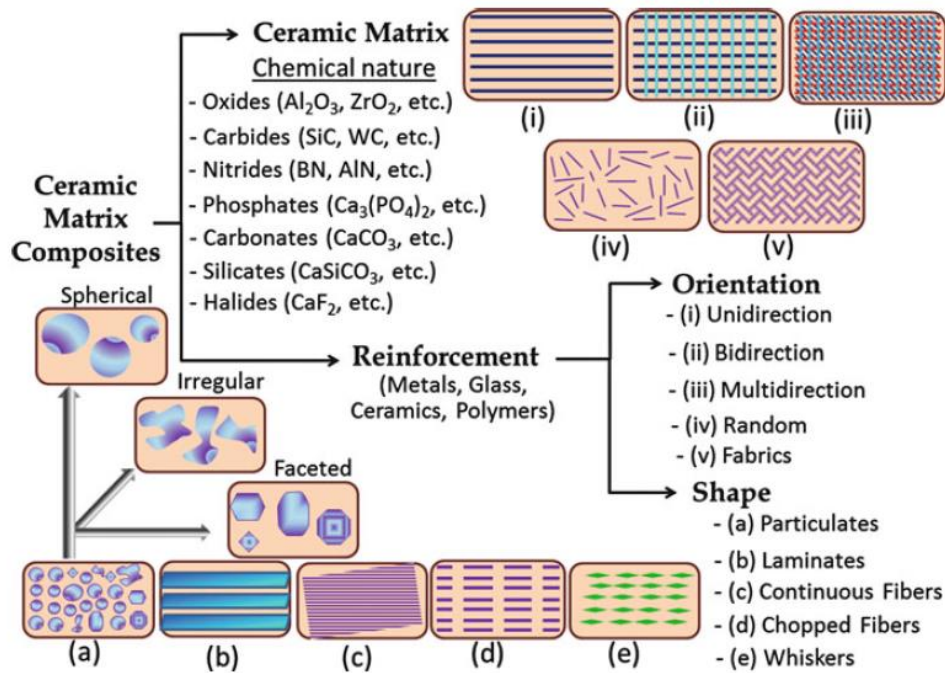


Fig. 2.1. Schematic of CMC classifications, the orange background represents the matrix and the front colours indicate reinforcing materials [7].

roughness.

Further, advanced ceramic composites are attractive because of their prominent properties namely: low density, chemical inertness, high stiffness, high strength, high hardness, and high-temperature stability [4,5]. However, although CMCs possess various interesting properties, they often present a brittle behaviour at the monolithic state, which constitutes a major issue [6]. To overcome this issue, several attempts have been developed to improve the fracture behaviour of CMCs and maintain all the other advantages of the monolithic ceramics. CMCs are produced from at least one nanophase embedded in a ceramic matrix as illustrated in Fig. 2.1 [7]. The nanophase can be one of the ceramic nanoparticles (SiC , Si_3N_4), nanotubes (carbon nanotubes (CNTs)), nanoplatelets (graphene) or hybrids of these materials.

Niihara et al. were the pioneers who introduced the concept of ceramic nanocomposites in 1991 [4,8,9]. Their work consisted on SiC nanoparticles incorporation as a second phase into (Al_2O_3 , Si_3N_4 , MgO) ceramic matrix. After reporting significant improvement, a series of research works have been succeeded with different nanoparticles including SiC, Si_3N_4 , TiN, TiC, TiO_2 , ZrO_2 , Cr_3C_2 in various ceramic matrix, such as Al_2O_3 , Si_3N_4 , MgO, SiAlON, etc...).

With the introduction of nanotechnology, reinforcing ceramic matrix with CNT has gained much interest after its discovery by *Iijima* [10]. Thanks to their one-dimensional nanostructure, CNTs provides incredible mechanical, electrical (10^7 S/m) and thermal properties (1800–6000 W/mK) compared to nanoparticles [11].

Hence, CNT incorporation not only increased ceramic matrix toughness but also have added the advantage of improving their functional properties namely electrical and thermal properties.

In order to produce CMC / CNTs composites with improved mechanical and functional properties, appropriate interfacial bonding between ceramic matrix and CNTs, besides uniform CNTs dispersion along the grain boundaries is required. However, due to their high aspect ratio, CNTs tend to agglomerate leading to stress concentration and thereby the overall properties of the composites are reduced. The preparation process and choosing the appropriate sintering technique, play an important role to define the final mechanical as well as tribological and functional properties of the composites [4,8].

YSZ nanocomposite is one representant of CMCs, which own an important interest during the last decades among all ceramic nanocomposite materials. In fact, YSZ nanocomposites are widely employed as a structural materials or functional materials as oxygen ion carriers mainly in power generation and environment protection. Besides its high thermal stability at high temperatures and proper mechanical properties, YSZ possess the advantage to present phase transformation from tetragonal to the monoclinic under applied stress, this mechanism is usually referred as transformation toughening zirconia. The resultant strain that is associated with the transformation relieves the stress field and therefore increases the intrinsic toughness [9].

2.2 Zirconia based ceramics

Zirconium dioxide (ZrO_2) named also zirconia is the mineral of baddeleyite and chemically is inert. In its pure form zirconia (ZrO_2) exhibits a polymorphic configuration and exists in three distinct phases at ambient pressure. Monoclinic phase is stable at room temperature to 1170 °C. Tetragonal with distorted fluorite structure is stable at intermediate temperature between 1170 °C and 2370 °C while the cubic fluorite phase is stable at very high temperature from 2370 °C to its melting point (2750 °C)[12,13]. The crystal structures of these three zirconia phases are presented in Fig. 2.2, where the large red spheres correspond to oxygen and the small green ones refers to zirconium. The higher the temperature, the better is the symmetry. The ability of phase transition makes zirconia the most studied ceramics material over the last decades and an important candidate for diverse areas of structural applications [14].

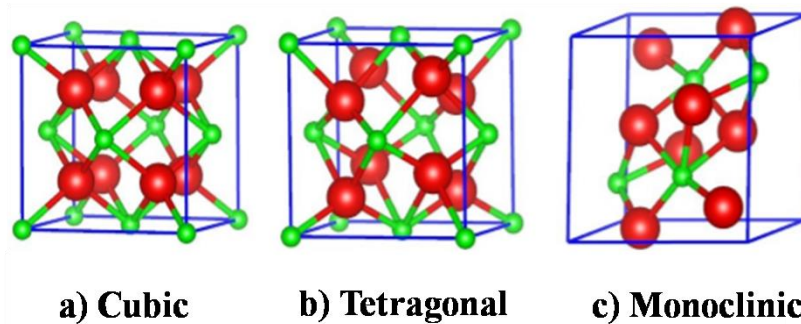


Fig. 2.2. Crystal cell of pure zirconia phases [15] (Red – oxygen, green – zirconium).

The structure of the cubic zirconia can be represented by a face centered cubic (FCC) structure similar to fluorite. The eight oxygen ions occupy the tetrahedral (0:25, 0:25, 0:25) sites, and are surrounded by Zr^{4+} cations which occupy the summits of the cube and the centers of each faces (Fig. 2.2a). Tetragonal phase of zirconia is represented by a straight prism with rectangular sides (Fig. 2.2b). Similarly, to the cubic structure zirconium (Zr) ions are coordinated to eight oxygen atoms and the oxygen atoms are coordinated to four Zr ions. However, the distorted shape of the tetragonal phase is linked with the alternative oxygen ions displacement along the c-axis. Resulting in the formation of two tetrahedron planes where one is elongated and rotated by 90° due to different distance of each four oxygen ions from Zr^{4+} (2.065Å and 2.455Å respectively)[16].

In its natural form, zirconia exhibits the monoclinic phase at low temperature known as baddeleyite. It contains about 2% of HfO₂ (hafnium oxide) having high chemical and structural similarity to zirconia. In the monoclinic phase, Zr⁴⁺ ions are coordinated to seven oxygen ions residing in tetrahedral interstices (Fig. 2.2c). The Zr ions are coordinated to three and four oxygen at an average distance of 2.07 Å and 2.21 Å respectively. Therefore, one of the angles (134.3°) differs considerably from the tetrahedral value (109.5°) [17].

2.2.1. Phase diagram of zirconia

Processing pure ZrO₂ is quite critical due to its polymorphic configuration. Indeed, during cooling, phase transformation from tetragonal to monoclinic occurs at temperature between 850 and 1000 °C. Consequently, a large volume expansion (5~7 vol%) is released which promotes the risk of brittle failure or generation of cracks and flaws within the ceramic matrix [18].

Therefore, the manufacturing of pure zirconia is not useful due to the impulsive failure. To retain the tetragonal form to room temperature after sintering, typical oxide dopants are added to pure zirconia, such as: yttria (Y₂O₃), calcium oxide (CaO) and ceria (CeO₂). However, yttria is the most common stabilizing oxide employed since lower amount are needed [19]. The phase diagram of ZrO₂/Y₂O₃ presented in Fig. 2.3 illustrates the stability regions of different phases according to the amount of yttria added to stabilize pure zirconia. It's shown that the reverse phase transition from monoclinic to tetragonal occurring at approximately 1170 °C decreased to <600°C with the addition of ~ 4.8 mol% yttria. The coexistence of a multiphase structure (cubic + tetragonal, cubic + monoclinic, cubic and tetragonal + monoclinic) is seen in the solid solution regions separated by the single phases. Hence, partially stabilized zirconia (PSZ) with cubic and tetragonal structures as major phase and monolithic precipitated in small amounts is produced [20]. These materials are stable at temperatures between 600 °C and 2000 °C with yttria content in the range of 3-8 mol% and manifest exceptional resistance to high thermal shock [17,21].

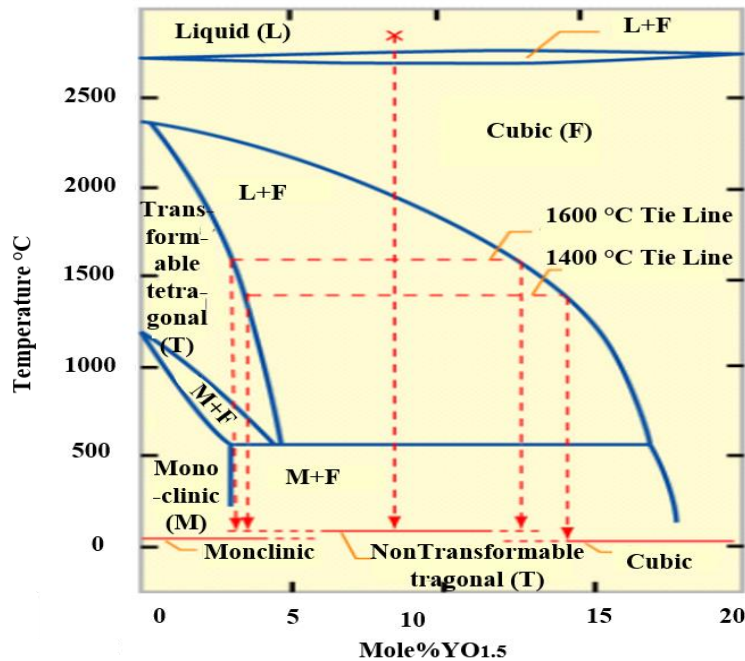


Fig. 2.3. Phase diagram of ZrO_2 - Y_2O_3 system [22].

Furthermore, retaining the tetragonal phase at room temperature in tetragonal zirconia polycrystals (TZP) formed by single phase metastable structure or fully stabilized zirconia (FSZ) with full cubic structure, stable at high temperature with higher yttria content (approximately +8 mol %) are the most useful state of zirconia [21]. Some studies claimed that the presence of small carbon fraction into cubic zirconia composite may boost its stability at room temperature [23]. In fact, TZP materials exhibit good comprehensive mechanical properties at both room and high temperatures, mainly attributed to the ferroelastic toughening mechanism, while FSZ are generally employed in electrochemical applications due to their high ionic conductivity [24,25].

2.2.2 Transformation toughening zirconia

The concept of stress-induced transformation from tetragonal to monoclinic is mostly occurred in TZP and PSZ ceramics, where the tetragonal phase is in its metastable state at room temperature. This concept based on change in grain shape accompanied with volume increase has been discovered at the first time in mid 1970s by *Garvie et al.* and led to considerable fracture toughness enhancement of zirconia composites as pointed out earlier [21]. This mechanism is known as transformation toughening zirconia and involves microcracked process zone at the crack

tip, as shown schematically in Fig. 2.4. As result of crack propagation, a stress field is procreated around the crack tip and contributes in phase transformation of the surrounded particles that occurs at a speed close to the speed of sound propagation in solids [17]. This phenomenon led in turn to the formation of transformed process zone constrained by the neighbour particles of a matrix.

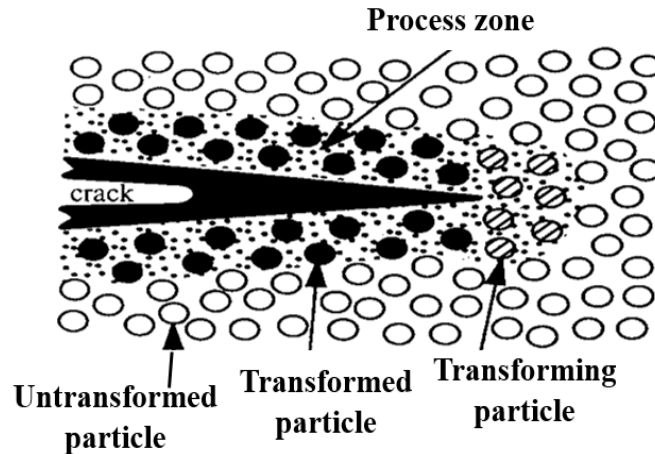


Fig. 2.4. Schematic view of transformation toughening process [26].

Indeed, the surrounding untransformed particles opposes to the dilated transformed zone and presses back with residual stresses that causes the generation of closure forces from each side of the crack tip and hence, retard crack extension. The transformation is called stress induced because an external applied stress is performed to help preceding the transformation due to matrix stretching. According to *Wolten*, phase transformation from tetragonal to monoclinic in zirconia is martensitic of nature similar to martensite transformation in quenched steels that is used to increase their hardness by particular heat treatments [27].

In ceramic, martensitic transformation occurs between the parent tetragonal phase and the product through nucleation and structural growth. This transformation is generally adiabatic, athermal and involves the atomic motion over distances less than an interatomic spacing, resulting in microscopic changes of shape of the transformed regions, which is associated with transformation toughening [28–31]. Furthermore, transformation toughening in partially stabilized zirconia is critically constrained by the particle size, which should be ranged in between 0.2 μm and 1 μm for 2 mol% to 3 mol%, yttria concentrations; otherwise the transformation to the monoclinic phase can be inhibited [32,33].

2.2.3. Ionic conductivity of yttria stabilized zirconia (YSZ)

Fully stabilized zirconia (FSZ) with cubic fluorite structure is commonly known as a solid electrolyte that possesses high oxygen ionic conductivity extended to wide ranges of temperature and oxygen partial pressure, and it is extensively employed as an oxygen sensor to control the emissions of automotive systems, combustion control for furnaces and engines, solid electrolyte for high-temperature fuel cells and hydrogen production. The dopant trivalent cations require a minimum activation energy. The cubic fluorite structure of zirconia becomes stable at room temperature with high Y_2O_3 addition and present high ionic conductivity at high temperatures [34–36]. The doping of ZrO_2 with Y_2O_3 , the Y^{3+} cations replace Zr^{4+} cations as shown in Fig. 2.5. This fact induces the formation of oxygen vacancies that maintain charge neutrality in the lattice.

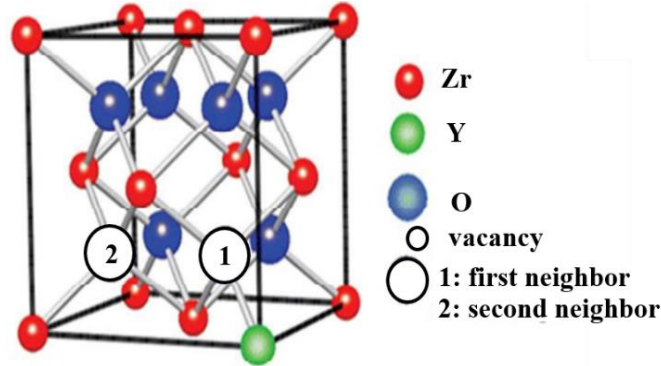


Fig. 2.5. Schematic structure of YSZ cubic fluorite [37].

Two types of interactions are established by the oxygen vacancies in the lattice. Repulsion with themselves and attraction toward the acceptor (Y^{3+} cations). Since yttria has one less valence electron than zirconium, one oxygen vacancy is created for two substituted Y^{3+} cations. Consequently, the oxygen ions are free to move from vacancy to vacancy in the lattice thereby, increasing the ionic conductivity of zirconia. The corresponding reaction in Kroger-Vink notation is described as follow [34]:



The maximum ionic conductivity is reached when doping zirconia with 8 to 9 mol% Y_2O_3 . However, higher doping rates will result in reduced mobility of the oxygen vacancies and the

creation of complexes with positive effective charge due to the bonding between an oxygen vacancy and one cation according the following notation [35].



The mobility of oxygen vacancies diminishes sharply with higher yttria concentrations, since one oxygen vacancy is bonded to two cations, leading to the formation of clusters and more complex associations as shown by the following Eq. 2.3 [36].



2.3 Carbon nanotubes (CNT)

The discovery of carbon in the form of graphite has been achieved in 1779, followed by diamond after 10 years later. These two enormous discoveries in the field of nanotechnology generally and carbon structure specifically, stimulates researchers worldwide to increase their interest in finding other forms of carbon more stable and structurally ordered. In 1985, a new form of carbon known as fullerenes has been accidentally discovered by *Kroto*, *Smalley* and *Curl* (Nobel prize in chemistry in 1996) [11]. The structure of fullerenes is almost similar to a single sheet of graphite (graphene) with a planar honeycomb lattice, in which each atom is attached to three neighbouring atoms (hexagonal rings) via a strong chemical bond. However, fullerenes sheet is practically not planar as graphene, which is linked to existence of additional pentagonal or sometimes heptagonal rings.

A few years later, in 1991 the Japanese scientist *Iijima* [10] discovered multiwall carbon nanotubes (MWCNTs) with an outer diameter ranged from 3 nm to 30 nm and at least two layers. Later in 1993, he discovered a new class of CNT with single wall carbon nanotubes (SWCNTs). SWCNTs tend to be curved rather than straight with a typical diameter in between 1–2 nm. The different types of CNTs are presented in Fig. 2.6. Carbon nanotubes (CNTs) are cylindrical fullerenes with nanometric diameter and micrometer sized length, which lead to a high length to diameter ratio exceeding 10^7 . Carbon nanotubes align themselves into chains by van der Waals forces, where the carbon atoms are sp^2 bonded with length of approximately 0.144 nm. In

MWCNTs the interlayer distance between two successive CNT is similar to the interspaces between two successive graphene layers in graphite about 3.4 Å.

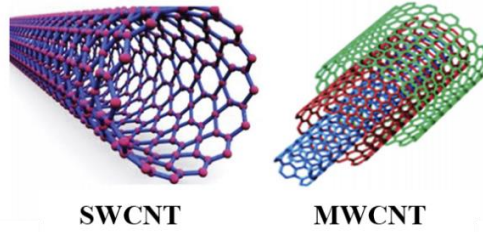


Fig. 2.6. Schematic diagrams showing different types of CNTs: single wall CNT and multiwall CNT (MWCNT)[38].

Since their discovery, MWCNTs open an incredible range of promising applications in nanocomposites, nano-electronics, medicine, energy and construction. Indeed, CNTs led to novel and unique properties, namely very high tensile (≈ 100 GPa) and Young's modulus (≈ 1500 GPa), high thermal conductivity and chemical stability and excellent electrical conductivity similar to silver and platinum [11, 40, 41].

Several carbon nanotubes structures can be produced depending on graphene sheet orientation on the rolling. The tremendous ways to roll fullerene into cylinders are specified by chiral vector \vec{c}_h determined by two integers (n, m) and chiral angle (θ) located between the chiral vector and zig-zag nanotube axis as shown in Fig. 2.6 and can be described in Eq. 2.4 and 2.5.

$$\vec{c}_h = n\vec{a}_1 + m\vec{a}_2 \quad (2.4)$$

$$\theta = \tan^{-1}(m\sqrt{3})/(m + 2n) \quad (2.5)$$

where, a_1 and a_2 are the unit cell vectors of the two-dimensional lattice formed by the graphene sheets.

As the chiral vector C is perpendicular to CNT axis, its length forms the CNT circumference and can be calculated according to Eq. 2.6.

$$\vec{c}_h = |C| = a\sqrt{n^2 + nm + m^2} \quad (2.6)$$

The length a is calculated based on the length of carbon–carbon bond a_{cc} generally approximated to 0.144 nm for graphene sheet as given by the following relation:

$$a = |a_1| = |a_2| = a_{cc}\sqrt{3} \quad (2.7)$$

The diameter can be deduced from the chiral vector c length as follow:

$$d = c/\pi \quad (2.8)$$

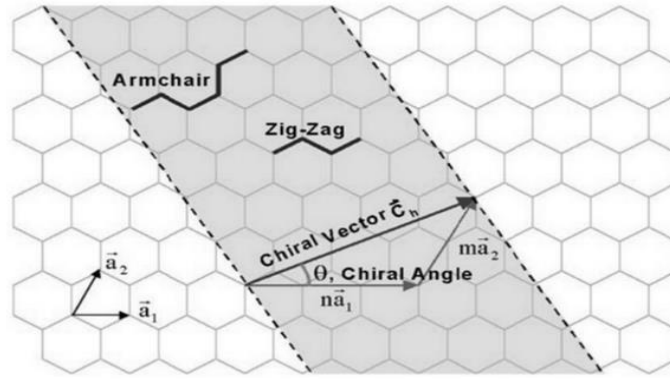


Fig. 2.7. Schematic diagram showing chiral vector and angle used to define CNT structure on hexagonal sheet of graphene [40].

CNTs can be classified either as armchair, zig-zag or chiral tube according to the pair of integers (n, m) in the chiral vector relation (Fig. 2.7). In armchair and zig-zag carbon nanotube the structure follows mirror symmetry in both axes (longitudinal and transverse) due to the arrangement of hexagons around the circumference. Whereas, the chiral carbon tube is characterized by non-symmetric structure and therefore, the mirror symmetry is not realized. These three different structures and enrolment of graphene sheet to form carbon nanotubes are shown in Fig. 2.8. Furthermore, the values of the integers (n, m) influence the optical, mechanical and the electronic properties of CNTs. CNTs are considered as semiconductors when $|n - m| = 3i \pm 1$ and metallic when $|n - m| = 3i$ [11,40].

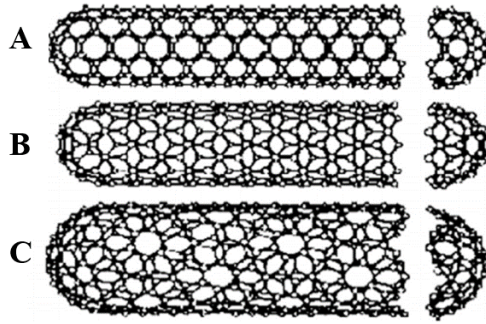


Fig. 2.8. CNT structure based on the chirality. The structure of CNT is easily determined by the terminations so called caps or end caps. (A) armchair structure, (B) zig-zag structure, (C) chiral structure [11].

2.3.1 Synthesis of CNTs

There are diverse synthetic routes to produce carbon nanotubes in which the quality depends on the preparation method. High-temperature evaporation methods such as arc discharge or pulsed laser deposition (PLD) yield to considerably manufacture low defect CNTs with high mechanical properties. However, these methods require a lot of purification from unwanted carbonaceous impurities and are generally operating at the gram scale, hence drive a quite expensive process. Nevertheless, scientists are researching more economical ways to produce CNT without complicated purification steps and easy to scale up. Chemical vapour deposition (CVD) or catalytic growth processes operate at lower temperatures and enables high CNT purity with controllable orientation and density. This method favourites large scale production for composite manufacture, both in academia and in industry and satisfy the low cost production. However, CNT produced by CVD usually present a lack of perfect structure which often degrades the intrinsic properties. Hence, the diverse synthetic routes should be taken into account when interpreting the CNTs performance in a given application [41].

Carbon nanotubes were initially detected in 1991 during an arc discharge which was planned to produce fullerenes (Fig. 2.9a). This technique is quite simple and involves DC arc discharge between two graphite electrodes under a current of 100 A, in inert atmosphere with or without catalyst. At high temperature (3000 °C or 4000 °C), carbon particle sublimates then self-assemble at the negative electrode or the walls of the chamber (Fig. 2.9a). Pure graphite electrodes allows

the synthesis of MWCNTs while SWCNTs requires a mixture of graphite and metal catalyst such as: Y, Mo, Fe, Co, Ni[10, 41]. The first growth of SWCNTs dates back to 1995 at Rice University, where SWCNTs with about (5–20 μm) in length and from 1 to 2 nm in diameter has been synthesized using PLD. In this method, carbon atoms are vaporized from a graphite pellet containing nickel or cobalt as catalyst material under laser beam (Fig. 2.9b). This process is maintained at high temperatures (about 1200 $^{\circ}\text{C}$) under constant flow of inert gases. Generally, this technique is considered as an excellent method to synthesize SWCNTs with high purity and controllable size[42].

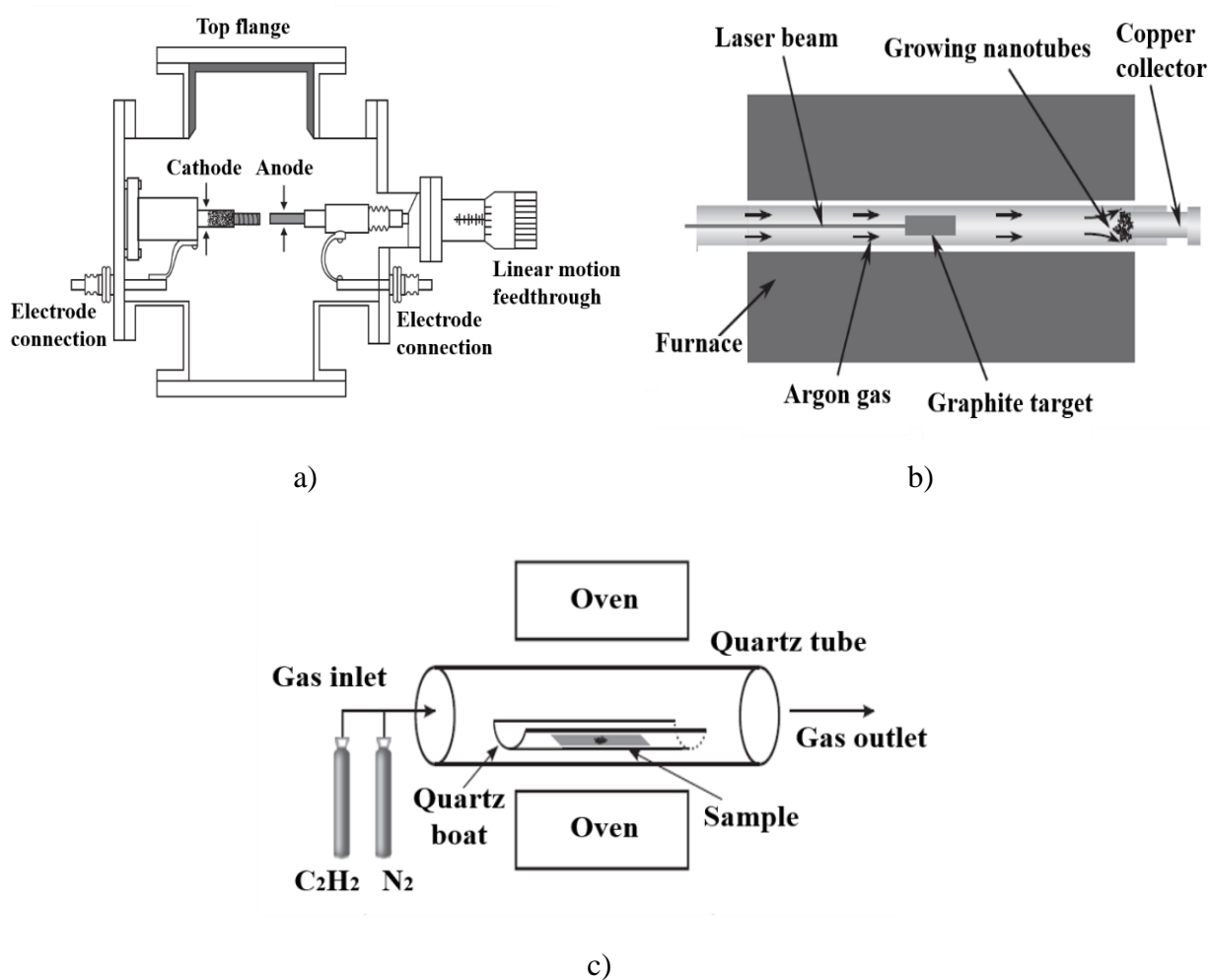


Fig. 2.9. Schematic illustration of the techniques used to synthesis carbon nanotube, a) arc discharge, b) pulsed laser deposition (PLD), c) chemical vapor deposition (CVD) [39,42].

On the other hand, in CVD the carbon source contains hydrocarbons such as acetylene, ethylene or ethanol, while the metal catalyst particles are usually cobalt, nickel, iron or a combination of these such as cobalt/iron or cobalt/ molybdenum (Fig. 2.9c). The catalyst tends to decompose the carbon from the gas in the presence of plasma irradiation or heat (600–1200 °C) and to assess the nucleation of CNTs. consequently, the free carbon atoms recombine in the form of CNTs on the substrates (commonly used are Ni, Si, SiO₂, Cu, Cu/Ti/Si, stainless steel or glass) [39].

2.4. Powders processing techniques

2.4.1 Dispersion of MWCNT into YSZ matrix using ball milling technique

Powder metallurgy techniques including ball milling method are considered as a major tool to produce homogeneous and uniform dispersion of advanced ceramic powders and their composites. Particle agglomeration prevention, homogeneous and uniform dispersion of MWCNT into structural ceramics matrix, presents a crucial challenge during the mixing process. In fact, the powder mixture features influence largely the final composite's properties such as: strength, density, wear resistance, friction ...). Ball milling synthesis for ceramic matrix/ MWCNTs powder is the most popular approach due to its simplicity and energy efficiency that promote high grain refinement and particular phase homogenization. High milling energies are essential to break the interlayer Van der Waal's forces between carbon surfaces that cause agglomeration and led to high MWCNTs surface energy. High rotational speed of the ball milling devices enables the balls to strike with the walls of the jar where high-energy collision arises [43]. The ceramic crystalline lattice undergoes severe mechanical deformation (fractures) and stress concentration (Fig. 2.10). The combined powders are reached after further milling time of grinding balls the combined powders tend to decrease until they are able to sustain deformation without any fracture. As the milling time increases, powder refinement takes place resulting in significant reduction of the particles size. Ball milling using liquid media proved higher efficiency in inhibiting agglomeration compared to dry media, as reported by several studies.

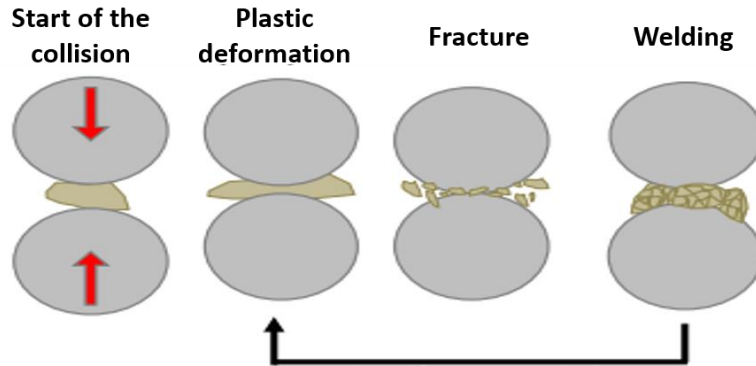


Fig. 2.10. Schematic illustration of the plastic deformation, fracture and welding of powder between the balls. The black arrow shows the repetition of the three processes.

On the other hand, powder contamination can be an issue with ball milling. This is why a protective atmosphere and ceramic milling jars and balls are recommended when milling hard ceramic particles. A good example of ceramic milling jars and ball is tungsten carbide which demonstrated almost no contamination in the final powders [43, 44]. *Decker et al.* examined the influence of high-energy ball milling on Mg-PSZ-reinforced TRIP steel matrix composites at different rotational speed of 100 rpm and 250 rpm [45]. It was found that at the rate of 250 rpm intensive deformation of the steel powder and mechanical interlocking between the steel and ceramic powder have been occurred, while the milling process at 100 rpm resulted in a homogeneous distribution without significant powder particles deformation. It was suggested to further increase the milling time for better distribution of the Mg-PSZ particles. In another work [46] performed by *Konga et al.*, a successful synthesization of nanosized Lead lanthanum zirconate titanate (PLZT) powders using high-energy ball milling and raw oxides as starting materials has been experimented. The PLZT powders with different dopant concentration exhibited a variety of ferroic phases such as ferroelectric (FE), antiferroelectric (AFE) and paraelectric (PE) phases and indicated superior sintering behaviour than those prepared via the conventional solid-state reaction process. Further, *Liu et al* synthesized and studied graphene platelet / zirconia-toughened alumina (GPL/ZTA) composites [47]. GPL-ZrO₂-Al₂O₃ powders were obtained by mixing graphene platelets and alumina powders using high energy ball milling and yttria stabilized ZrO₂ balls at 300 rpm. It was proved that the ball milling process provides the positive thermodynamic driving force to reverse martensitic transformation i.e. monoclinic to tetragonal

transformation, which provokes a cracking phenomenon during the cooling stage. Moreover, after 10 h milling the composite powder was nanostructured with grain size range of 35–60 nm and 25–54 nm for alumina and zirconia, respectively.

2.4.2 Spark plasma sintering (SPS)

Spark plasma sintering (SPS) is a powder metallurgy process enabling the rapid synthesis of a wide range of advanced materials with small grain sizes and at relatively low temperatures. SPS uses high pulsating DC current to heat directly the specimens simultaneously with application of uniaxial pressure to consolidate powders into a bulk material [48,49]. The first SPS machine based on pulsed current was developed by *Inoue et al.* in the early 1960s [50]. Their invention was based on the idea of sintering under an electric current patented firstly in 1906. However, reaching high efficiency with reasonable equipment cost was a critical point that limited its wider commercialization [51]. The advantages of SPS process over other traditional sintering methods such as hot-pressing and hot-isostatic pressing are the ability to consolidate high temperature ceramics, metals and composites in a few minutes with 1000 °C/min heating rate, resulting in reduced duration and energy costs [48, 51], high thermal efficiency due to the absence of any heating elements. SPS heats by passing a high- pulsed direct current through a graphite die and the sample to be sintered. Typical SPS configuration [52] is illustrated in Fig. 2.11. The powder is inserted into a conductive graphite die in a water cooled SPS chamber. During the sintering a uniaxial pressure is applied to the die by an upper and a lower punch. Then, a pulsed current is directed through the punch and the die for thermal heating under vacuum or protective gas evacuated and filled through the water cooled chamber. Sintering temperature can be adjusted to high value 2400 °C using either thermocouples or axial/radial pyrometers. SPS process enables uniform Joule heating conditions especially for conducting samples. Further, the current enhances largely the mass transport mechanism through electro-migration, which contributes to obtaining dense samples with finer grain structures despite the low sintering times and temperatures [53–55]. Furthermore, high mechanical pressure in the range of 50 - 250 kN can be applied to enhance the densification by increasing the contact between grains and breaking-down the agglomeration, especially for large particles [49].

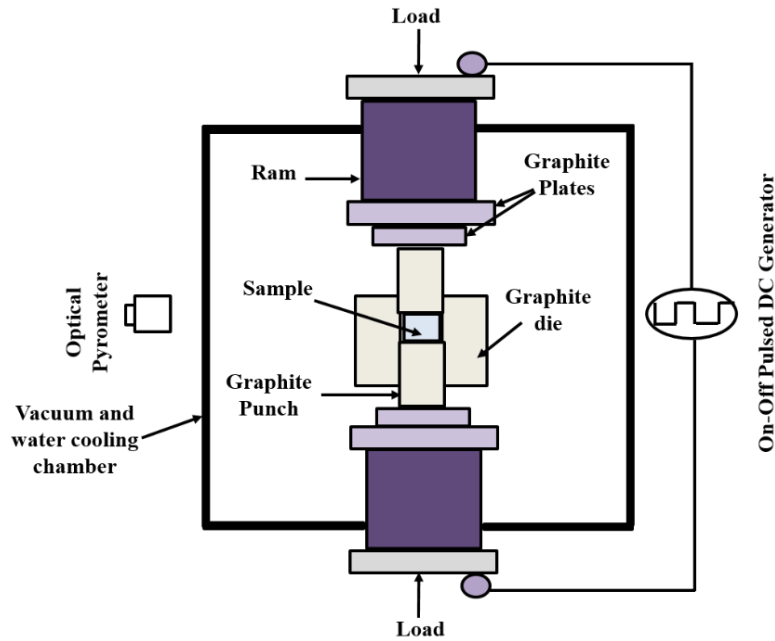


Fig. 2.11. A typical SPS chamber setup.

In fact, considerable improvement of particle rearrangement can be obtained with uniaxial pressure due to superplastic flow generation via grain boundary sliding. In this context, *Anselimi-Tamburini et al.* elucidated the pressure effect on the densified specimens based on the driving force for initial densification [53]. According to Eq. 2.9 the driving force for densification increase proportionally with the applied pressure [56].

$$\text{Driving force} = \gamma + \frac{P \times r}{\pi} \quad (2.9)$$

where: γ is the surface energy, P is the applied pressure and r is the particle radius.

However, based on experimental demonstration *Skandan et al.* proved that beneficial pressure effect on the densification occurs only if the pressure effect exceeds that of the surface energy [57]. In other words, the small are the particles the high is the pressure required to enhance densification. The effect of temperature and pressure on the grain size of zirconia samples sintered with SPS technique is presented in Fig. 2.12. It is shown that applying high pressure simultaneously with low temperature is efficient to produce grains with minimal size. Hence the optimization of pressure and temperature is a key factor in the fabrication of dense zirconia samples [58].

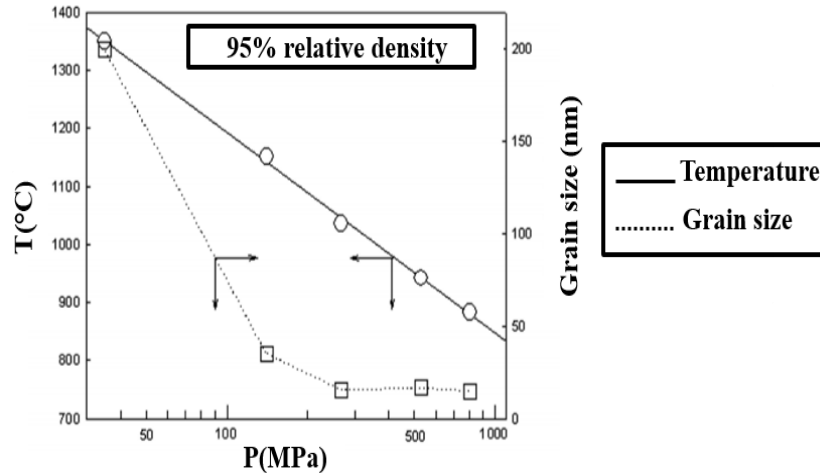


Fig. 2.12. Influence of sintering pressure on the temperature required for 95% TD in zirconia with corresponding grain size [54].

The apparition of spark discharges caused by alternative switching on and off the DC current creates hot regions where the impurities located between particles are melted and vaporized. This process has been advocated mainly to the generation of weak plasma through the powder sintered under pulsed current and causes a phenomenon referred to as “necking” leading to high purification and joining of the densified particles. The detailed steps of the process are shown in Fig.2.13. However, the concept of plasma still remains not adequately understood, without providing direct justification of its existence. Thus, plasma generation represent an important objective of struggle to establish an implicit understanding of the process.

D. Robles Arellano et al investigated the effect of sintering techniques on the densification behaviour of 8 mol% yttria stabilized zirconia (YSZ) based composites with the addition of 11.6, 21.6 and 30.5 wt% La_2O_3 [59]. Their work draw clearly the advantage of SPS to attain high densification level (~92 – 96%) in La_2O_3 +YSZ composites at significantly lower time, pressure and temperature process conditions (1500 °C, 50 MPa and 10 min) compared to pressureless sintering with lower relative density of about (82%) at 1600 °C held for 2 h and HIP sintering technique with relative density of 99.7% performed at 1500 °C, 196 MPa for 2 h.

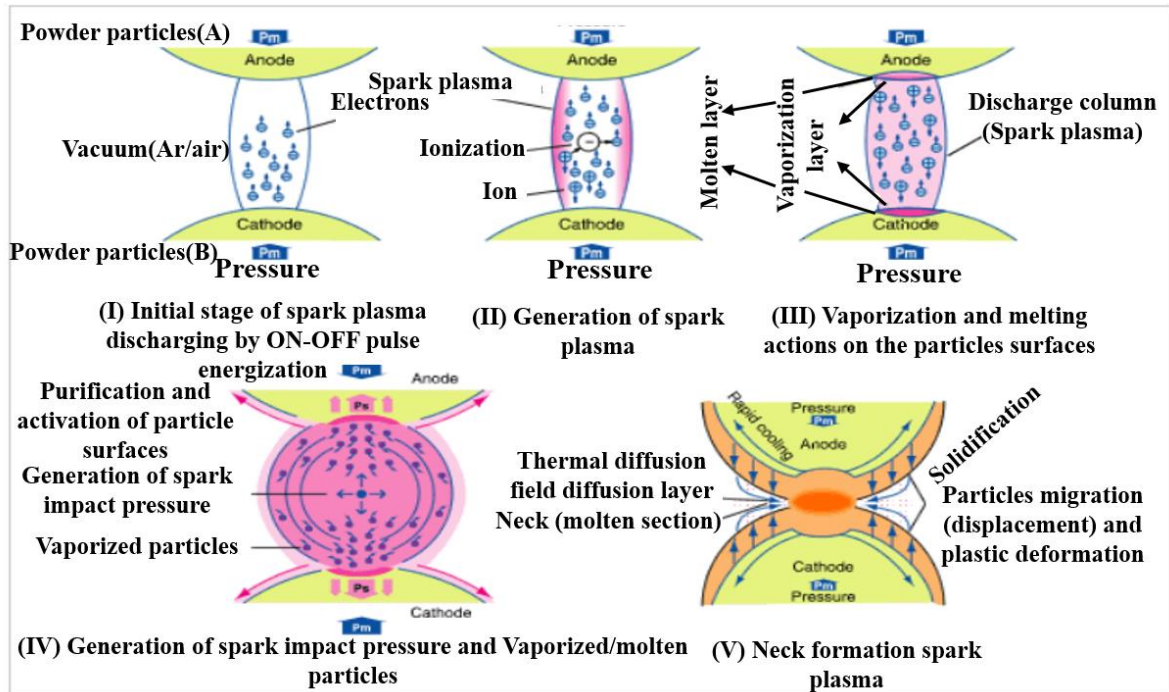


Fig. 2.13. Detailed steps of neck formation during SPS due to the spark discharges [52].

In addition, *M. Mazaheri et al* investigated the processing features of yttria stabilized zirconia reinforced with multiwall carbon nanotubes sintered by SPS [60]. It was found that SPS is an efficient way to produce fully dense composites with the ability to reduce CNTs structural damages at high temperature contrary to the conventional sintering methods. It also enabled a strong bonding between MWCNT and the ceramic matrix, which is a prerequisite for enhanced mechanical properties. In a similar work performed by *Karanam et al.* regarding the investigation of densification behaviour in 0.2, 0.5, and 1 wt% YSZ / CNT ceramic composites processed via SPS [61]. The detailed interpretation of the advantageous role of SPS process and CNT in enhancing the hardness and resistance to crack propagation in YSZ / CNT ceramic composites was presented. Indeed, it was found that the presence of CNTs within YSZ matrix led to a delayed densification and grain growth during SPS processing, which in turn reduce the density of the composite. However, during SPS processing CNTs helps to pin grain boundaries which resulted in enhanced mechanical properties.

2.5 Mechanical behaviour of ceramic matrix composites (CMC)

2.5.1 Stress strain-curves of pure ceramics via CMC

The strength of ceramic materials is most commonly measured using tensile test, where the external forces tend to elongate the specimens. Typical stress–strain curves comparing the tensile behaviour of pure ceramics with different types of reinforced CMCs is depicted in Fig. 2.14. In pure ceramics (illustrated by the black curve), brittle fracture generally arises before the occurrence of plastic deformation. In fact, in pure ceramic material, the binding orbital of electrons are localized around the corresponding ion cores restricting the movement of electrons. As a result, very high energy is required to generate the movement of dislocations and therefore make the plastic deformation possible [62, 63].

Contrary to pure ceramics, ceramic matrix reinforcement with the help of fibers such as carbon nanotubes (CNTs), boron nitride nanotubes (BNNTs) or whiskers of titanium carbide (TiC), silicon carbide (SiC), silicon nitride (Si_3N_4), boron carbide (B_4C) led to a significant enhancement in fracture toughness, wear resistance and strength behaviour [64]. Indeed, at lower applied stress as shown in Fig. 2.14, both pure ceramics and CMC shares similar elastic mechanical response, which means that the material regains its initial state when the stresses are removed.

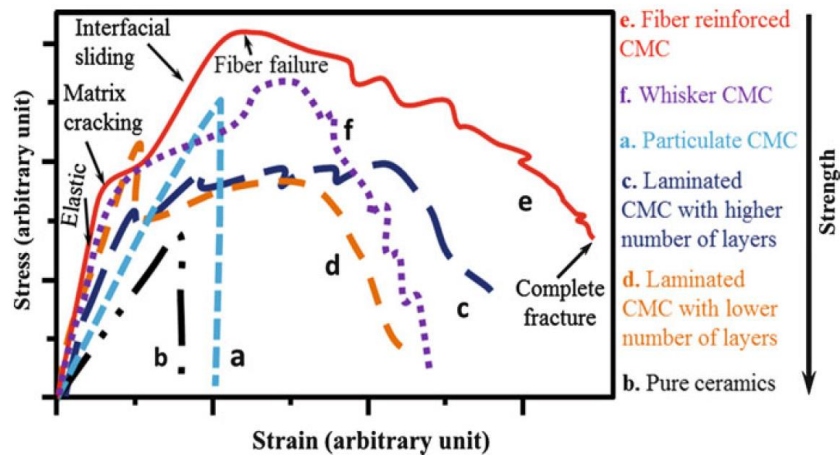


Fig. 2.14. Schematic of typical stress strain curves of pure ceramics and different types of reinforced CMCs [7].

This region is characterized by the elastic modulus most commonly designated as E and can be determined mechanically from the linear region where the stress and strain exhibit a proportional relationship. E is mechanically reversible and can be characterized by the ratio of stress to strain that is equal to the elastic modulus constant according to *Hooke's Law* [65].

$$\sigma = E \cdot \varepsilon \quad (2.10)$$

where σ is the measured stress (Pa), E is elastic modulus (Pa), and ε is the strain (mm/mm) [66–68].

In addition, E can be determined also using the sonic technique. This method involves a piezoelectric transducer that measures the time of flight of transverse and shear waves. As a result, the recorded voltage as a function of time can be plotted. Due to the minimal sensitivity to internal defects the sonic technique is mainly employed to distinguish between the materials [69, 70].

When the applied stress increases, a plastic deformation occurs due to matrix cracking. As a result, the stress–strain curve of CMC follows a nonlinear behaviour as can be seen from Fig. 2.14. At even higher stress, the cracks reach the saturation and remains nearly constant. The end of the final step is characterized by material failure, where the stress–strain curve follows linear behaviour but with lower tangential modulus compared to initial modulus.

In fact, the fibers and whiskers form an additional resistance barrier when the stress is applied resulting in pull-out, crack bridging and crack deflection [71]. As a consequence, these mechanisms lead to crack self-healing, strong bonding within the ceramic matrix. Thus higher tensile strength is achieved in CMC compared to pure ceramics. Generally, the tensile strength of ceramics composites is much lower than their compressive strength (about ten times). This is due to the external forces applied during the compressive test that tend to decrease the specimen volume and then limiting the flaw propagation. Indeed, in compressive loading plastic deformation such as glide bands and the pile-up of dislocations at grain boundaries, micro cracks take place at very high loading to conduct to the fracture [62,63]. Consequently, ceramics are usually used in applications where loads are compressive.

2.5.2 Ceramic matrix composites: challenges

Despite, the major advantages and unique properties achieved with the fabrication of CMC materials, the recent literatures reported several dissimilarities of the nanomaterials effectiveness dispersed within the ceramic matrix or at the grain boundaries. Indeed, this has been suggested to be in link with several issues due to the choice of synthesis techniques or sintering treatment.

A. Gallardo-López et al. prepared 3 mol% yttria tetragonal zirconia polycrystals (3YTZP) composites with 1, 2.5, 5 and 10 vol% nominal contents of graphene nanoplatelets (GNPs) [72]. The mixture was synthesized using ultrasonic probe agitation of GNPs. Fully dense composites were obtained after SPS sintering at 1250 °C for 5 min. Further, Vickers hardness decreased with GNP content from 13.9 GPa in 3YTZP to 8.1 GPa in 3YTZP with 10 vol% GNPs. Moreover, significant hardness anisotropy was obtained in the perpendicular plane to the sintering compared to the cross section. This anisotropy augmented with GNPs content. *Zahedi et.al.* compared the effectiveness of CNT dispersion in wet and dry media to avoid agglomerations [73]. The density of the samples prepared in wet media was generally higher compared to dry media samples. This was attributed to high CNT homogeneity found in wet media method. *Melka et.al* studied tetragonal zirconia polycrystals doped with 3 mol% yttria (3Y-TZP) and multiwall carbon nanotubes (MWCNTs) content from 0.5 to 4wt% [74]. A strong increase in the electrical conductivity for the sintered composite with 0.5 wt% MWCNTs content has been claimed. *Xu et al.* used boron nitride nanotubes (BNNT) instead of CNT or graphene to improve zirconia fracture toughness [75]. BNNTs with 0.5, 1 and 2 wt% were added to zirconia matrix. The highest flexural strength and fracture toughness were found in the composite with 1 wt% of BNNT (1143.3 MPa and 13.13 MPam^{1/2} respectively). *Duszova et al.* studied the effect of CNTs content on the mechanical and electrical properties of monolithic zirconia [76]. The addition of the CNTs decreased the hardness and indentation toughness from 1297 kg/mm² to 830 kg/mm² and from 8.01 MPam^{0.5} to 5.6 MPam^{0.5} respectively. This fact was attributed mainly to the residual porosity remained in the material after sintering. CNT and graphene can be easily damaged by the high sintering temperature and therefore, react with the oxide matrix [77]. Spark plasma sintering (SPS) has been emphasized by all to enable high ceramic consolidation with minimal damage [78].

2.5.3 Fracture toughness of ceramic composites

The use of ceramics and composites in any successful application requires a careful investigation and design of the crack propagation mechanism and its occurrence. The spontaneous extension of cracks can be described by the Griffith/Irwin criterion (Eq. 2.11) and refers to the stress intensity factor (SIF) (K , $\text{MPa}\cdot\text{m}^{0.5}$) described as the material ability to adhere the loading at the presence of intrinsic flaws [79,80].

$$K = \sigma Y \sqrt{\pi a} \quad (2.11)$$

where σ (MPa) is the stress in the uncracked body, Y is a dimensionless geometric factor describes the preexisting flaw geometry and the specimen and a (m) is the crack length.

Failure occurs if the stress intensity factor (SIF) reaches or exceeds the fracture toughness K_{Ic} (which is the resistance of the material against crack extension).

$$K \geq K_{Ic} \quad (2.12)$$

The determination of fracture toughness based on conventional methods such as single edge notched beam (SENB), the single edge V-notched beam (SEVNB), Chevron notched beam, surface crack in flexure (CNB and SCF), single edge pre-cracked beam (SEPB), and other conventional methods is hardly assessed on the brittle ceramics or composites because of their notable brittleness (the hard phase and high elastic modulus) and the difficulty to create a sharp pre-cracked specimen. In addition, these methods require arduous sample preparation and a particular notch geometry control to get only one result for each sample. Therefore, a significant time consumption and expensive procedures are crucial [81–84].

2.5.4 Hardness of ceramic composites

The hardness of materials is considered as a key parameter in the field of material science, engineering design and analysis of structures. The principal aim of the hardness test is to develop more sophisticated devices and machines suitable for a given application or a particular treatment. As a general definition, hardness refers to material quality rather than a physical property and is defined as the resistance to plastic deformation or penetration namely by indentation, wear, abrasion or scratch. In 1900, the Swedish engineer *Brinell* was the first who invented an effective and modern method using hard steel ball as the indenter to measure the hardness of a given

material. His method entitled Brinell hardness testing presented an alternative to: 1. Traditional resistance test, which used to measure the scratch resistance in Mhos. 2. The destructive and high time-consumption of the tensile test, besides, its difficulty to be performed on several small sized new materials. Therefore, Brinell hardness testing using a hard steel ball as the indenter has been often the only solution [63, 67, 85, 86].

Meanwhile, several authors discussed the hardness testing on ceramics through discussion of indentation fracture or as a fundamental description. Among them, the most influencing ones were *McColm* (1990), *Lawn* (1993) *Tabor* (1951) and *Chandler* (1999) [85]. Today, several hardness testing variants exist, where the most common are Rockwell and Brinell test usually used to evaluate the hardness of soft to medium hard metals and material with non-uniform microstructures. On the other hand, other hardness testing methods such as Vickers and Knoop are usually applied on ceramics [67, 80]. According to the applied loads on the indenter, hardness testing can be divided into two groups: macro-hardness and micro-hardness. When the applied load exceeds 1 kg, the test is known as macro-hardness and usually performed on large sized material such as testing tools, dies etc. Below 1 kg applied loads, the test is considered as microhardness, mainly devoted to small scale material which includes thin films, small parts and individual constituents of materials [63,86]. The geometry of the indenter, load, dwell time besides the means of result interpretation are the key factors to differ between the mentioned hardness testing methods.

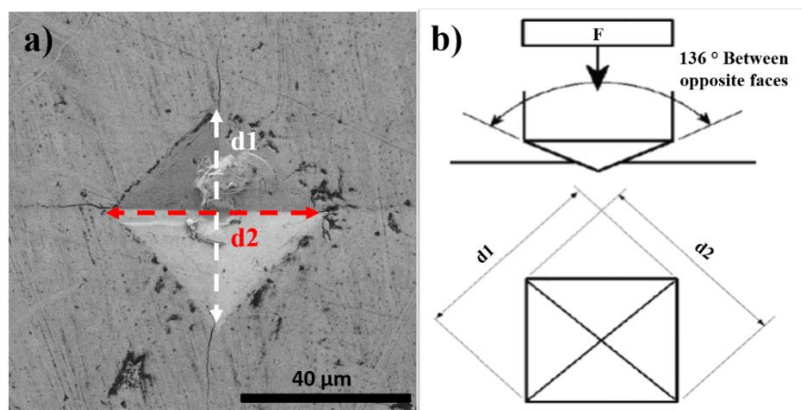


Fig. 2.15. Hardness test. a) Vickers indentation under 19.6 N load in SPS sintered zirconia [84], b) Schematic of Vickers hardness principle.

Vickers hardness test is the most preferred one due to several advantages. Indeed, in addition to the extremely high precision Vickers hardness test uses only one type of indenter that is adaptable to all types of materials including the softest and hardest ones (Fig. 2.15). However, the Vickers machine is more expensive than the Brinell or Rockwell machines [67,87]. Generally, in ceramics hardness is closely related to yield strength and can reflect the material's resistance to wear. The most cited empirical equation in the literature [80,88], that describes Vickers hardness/yield strength relationship follows approximately the form as below:

$$H_V \approx 3. \sigma_y \quad (2.13)$$

where σ_y is the yield strength.

2.5.5 Indentation fracture toughness of ceramic composites

To overcome these difficulties several simple techniques have been established for this purpose. The most attractive one is referred to as indentation fracture toughness that involves the measurements of the emanated crack lengths from the corners of Vickers indentation diagonals. This method basically enables easy, fast and cheap experimental procedure in addition to the non-destructive test since only small sample size is required. Vickers and Knoop indentation hardness tests are the most commonly used techniques to create an indentation mark on the well and smoothly polished sample. In these methods, the indenter is forced into the surface at high testing load until a plastically deformed region is formed below and around the indentation, resulting in cracks emanated from the four corners of the impression zone and residual stresses according to the material features. The indentation fracture toughness method involves the crack length and shape, load, impression size, hardness, calibration constant and sometimes the elastic modulus [81, 89 –91]. Numerous studies performed on polycrystalline ceramics describe the Palmqvist crack as the four independent radial cracks which do not connect to each other under the indentation. This type of crack is mostly formed at low and intermediate load. Above a characteristic generally quite high threshold load, the cracks merge to a median type where the cracks are interconnected in the sample depth [79, 95, 96].

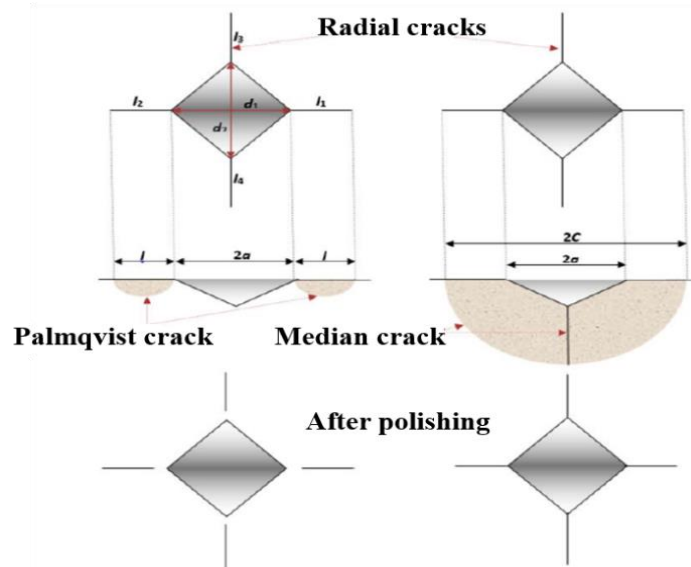


Fig. 2.16. Type of cracks in ceramic material.

The two models referring to Palmqvist and median crack under Vickers indentation are illustrated in Fig. 2.16. Indeed, the geometry of the crack can be affected by crack growth mechanism that is associated with the presence of a complex residual stress network around the indentation in some material. Therefore, in some cases it can be hard to approve if the median crack shape is an extension of Palmqvist cracks due to residual stress or its formed directly at the beginning from the indenter [40]. The two crack shapes can be identified by several methods. A formal commonly used criterion relies on measuring the crack-length/indent diagonal ratio. Indeed, when the ratio is larger than 2 the crack geometry is attributed to the median shape, else it is Palmqvist. Other experimental techniques known as decoration [97–102], process and serial sectioning technique [79, 83, 103, 104] are widely used. The decoration of the indentation cracks method proposed by *Jones et al.* requires a saturated lead acetate solution which is soaked into the polished tensile surface of flexural specimens [105]. In this method, the crack path can be observed under SEM micrographs after fractographic test (taking into consideration the original indentation crack as failure origin) and the completed drying of the excess lead acetate solution usually by using an oven.

In addition, the crack shape can be determined by serial sectioning method based on layer-by-layer material removal by ceramographic polishing. At the end of surface polishing, the cracks

remain connected to the inverted pyramid of the indentation in case of median shape, while the Palmqvist cracks exhibits a detached radial crack as displayed in Fig. 2.16.

2.5.6 Vickers indentation fracture toughness of ceramic composites

By far, most of the studies cited in the literature use the Vickers indenter to determine the fracture toughness directly from indentation mark. Different models (more than 30 equations) have been developed by a large number of authors either by empirical or experimental processes, some of which involves the Young and Poisson modulus in addition to the hardness test results. Most of the equations are a reformulation of the previous equations with novel calibration constants depending on the crack type (Palmqvist or radial-median), crack length, and material properties.

As mentioned earlier, the conventional techniques are hardly applicable to large scale samples due to the laborious crack measuring, robust equipment and the requirement of a very precise notch geometry control [106]. Furthermore, the raised residual stresses and the hard surface preparation can influence largely the final results.

As consequence, in 1970, *Evans* and *Charles* were the pioneer who developed the Vickers indentation fracture technique to assess the fracture toughness of ceramics and their composites. In 1976, they published a short communication, where they presented a normalized calibration curve fitting to correlate the crack length (c) and indentation size (a) to estimate the indentation fracture toughness. In their paper, a generated equation has been provided that seems to be used regardless the crack shape (Palmqvist or with median) as illustrated below [40,106]:

$$K_{IC} = 0.16(c/a)^{-1.5} \left(H_V \cdot a^{1/2} \right) \quad (2.14)$$

Afterwards, the indentation method has successively received much interest because of its expediency. However, the indentation fracture toughness scientist community assumes that it's important to establish new models for each crack type to obtain accurate fracture toughness values.

Consequently, in 1981 *Marshall* and *Evans* [107] simplified and corrected the formula of indentation given by *Evans* and *Charles* applied to median crack, while *Anstis et al.* proposed additional modifications to the proposed equation as presented below [108]:

Marshall and Evans [107,109]:

$$K_{IC} = 0.036E^4P^6a^{-7}(c/a)^{-1.5} \quad (2.15)$$

Antis, Chantikul, Lawn, and Marshall [108, 109]:

$$K_{IC} = 0.016 \left(\frac{E}{H_V} \right)^{0.5} \frac{P}{C^{1.5}} \quad (2.16)$$

Other reformulations of the previous equations for median crack were established by Lauginer, Casselas and Nihara as cited below:

Lauginer [81, 109]:

$$K_{IC} = 0.010 \left(\frac{E}{H_V} \right)^{0.6} \frac{P}{C^{1.5}} \quad (2.17)$$

Casselas [81, 109]:

$$K_{IC} = 0.024 \left(\frac{E}{H_V} \right)^{0.5} \frac{P}{C^{1.5}} \quad (2.18)$$

Nihara, Morena, and Hasselman [81, 109]:

$$K_{IC} = 0.0309 \left(\frac{E}{H_V} \right)^{0.4} \frac{P}{C^{1.5}} \quad (2.19)$$

The models assume that the residual stress formed underneath the indentation in the plastically damaged zone proceeds as expanding cavities that pulls the median cracks apart. Subsequently, different authors successively described the Palmqvist cracks models to estimate the indentation fracture toughness. All the equations applied to Palmqvist crack type use the Exner crack resistance (W)[83], defined by the ratio between indentation load (P) and the sum of the cracks length at the corners of the Vickers hardness impression using the following Equation:

$$W = \frac{P}{\sum_{i=1}^4 l_i} \quad (2.20)$$

The most commonly cited equations to describe the Palmqvist crack type are presented as follows:

Warren and Matzke model [81, 109]:

$$K_{IC} = 0.087 \cdot (H_V \cdot W)^{1/2} \quad (2.21)$$

Nihara, Morrena, and Hasselman model [81, 109]:

$$K_{IC} = 0.0246. (E/H_V)^{2/5}. (H_V. W)^{1/2} \quad (2.22)$$

Shetty, Wright, Mincer, and Clauer model [81, 109]:

$$K_{IC} = 0.0889. (H_V. W)^{1/2} \quad (2.23)$$

However, the different proposed equations result in large standard deviation of K_{IC} results. In addition, when the properties are not homogeneously distributed along the sample surface, this method may not represent accurately the indentation fracture toughness due to the small indented zone. Therefore, several tests must be carried out on the same specimens for a better precision.

2.6 Tribological properties of ceramic matrix composites

The optimization of wear resistance and friction coefficient is considered as a preliminary step during the design of a new tribological system, able to withstand severe thermo-mechanical environment. Reinforced ceramic composites appears nowadays commercially competitive to the traditional materials for example: grey cast iron or carbon/carbon used in the fabrication of brake systems which require reduced friction coefficient and high wear resistance [1, 110]. In fact, nano-conductive particles, whiskers or fibres (MWCNTs or graphene) have been in several works endowed as a secondary phase into structural ceramics such as: yttria stabilized zirconia (YSZ), silicon nitride (Si_3N_4), silicon carbide (SiC) or aluminium oxide (Al_2O_3) to improve their mechanical as well as tribological properties. The major advantages of reinforced structural ceramics reside in their greater strength, reduced density, high abrasion/wear resistance and high temperature stability [111]. Indeed, reinforced structural ceramics demonstrated high tribological performance at lab as well as industrial scale, which enable their wide commercialization for short and long operational lifetime applications. Advanced nozzle jet vanes used in missiles or hot structures for spacecraft are good examples of short life time applications where mostly melt infiltrated composites like C/C–SiC coated with a ceramic surface protection take a part [112]. Other typical applications requiring special wear resistance performances for longer structural lifetime are devoted to terrestrial applications including brake systems in cars, trains, aircraft or elevators. In this context, several ceramic matrix composites have been investigated for these purposes [110, 113, 114]. *Kasperski et al* prepared ZrO_2 / MWCNT composites by SPS. Several amounts of MWCNT (0.5, 1, 1.68, 3.24 and 5.16 wt %) have been added to zirconia matrix [115].

The wear test investigation has been performed under a load of 5 and 10 N using alumina ball as a counterpart. The frictional properties were reduced with increasing MWCNT amount from 0.5 to 3.24 wt%. However, the friction coefficient and the wear resistance were significantly improved with 5 wt% MWCNT addition, which was in line with the fainter track and the higher lubricating effect observed on the worn areas. On the other hand, the highest average arithmetic roughness was attributed to the composite with 5 wt% of MWCNT about 0.11 compared to the other composites, where the roughness was located in the range of (0.01- 0.03) causing easier zirconia grains pull-out during polishing. *Hvizdos et al.* investigated the tribological properties of GNPs with 1 and 3 wt% additions into Si_3N_4 matrix under (5 N) load and maximum sliding distance of 300 m [116]. Steady-state of friction coefficient were recorded at short sliding distance followed by more or less higher fluctuation depending on the composite content. According to the results, the best friction coefficient and wear resistance have been obtained in the composite with 3 wt% graphene addition to Si_3N_4 matrix illustrated by remarkable wear rate decreased (about 60 %) compared to Si_3N_4 reference. The microstructural features analysis was related closely to the wear damage mechanism. In fact, it confirmed a strong GNPs interfacial bonding to silicon nitride matrix. This high integration of GNPs into the microstructure prohibited finding a significant lubrication effect during wear test. On the other hand, intensive milling process for more than 10 h played an important role to achieve large distance between graphene multilayers and therefore acquire the expected tribological properties.

Latifa et al studied the friction and wear behaviour of spark plasma sintered 3 mol% yttria stabilized tetragonal zirconia (3Y-TZP) reinforced with up to 2 wt% MWCNTs using zirconia ball with 10 mm diameter as a counterpart [117]. In their study, the friction coefficients (COFs) were evaluated in macro-scratch testing with a sliding Rockwell indenter at increasing loads. Strong oscillations have been recorded in the COF beyond a critical load relatively higher. The oscillations appeared earlier for the composites with larger amount of MWCNT provoking brittle fracture and chipping trend. The origin of the brittle fracture and chipping were supposed to be resulted from the weak zirconia and MWCNTs interface or due to the tensile stresses appeared during the scratch test. However, the effect of MWCNTs addition on COF under low applied loads resided in considerable increases reflecting low wear rate. In another study, the influence of the applied load and sliding speed on the friction and wear behaviour of ZrO_2 with 1.07 wt% carbon nanofiber (CNFs) composite has been investigated by *Hvizdos et al* [118]. A slight variation of the friction

coefficient (0.22– 0.27) for various sliding speeds 2.5, 5, 10, 15 cm.s^{-1} has been found. In addition, a significant increase in the friction coefficient with respect to the applied load from (0.25 to 0.35 via 1 N to 5 N) respectively has been observed. A low amount of debris formed by CNFs and zirconia particles appeared at 1 N applied load. However, at higher load (5 N) zirconia grains and perpendicularly oriented CNFs pull-out to the worn surface were observed. In fact, the mixture formed a transferred film which led to attain a lubricating effect during sliding and therefore enhanced the tribological properties of the composite.

2.7 Application of yttria stabilized zirconia in energy sector

Fuel cells are electrochemical devices that allow the direct conversion of chemical energy of the reactants into electrical energy (Fig. 2.17). Fuel cells, are one of the most promising technologies and environmental friendly power generation devices which are recently an attractive area of continuous development simultaneously with the increasing renewable energy supply. Fuel cells can be classified into two different aspects.

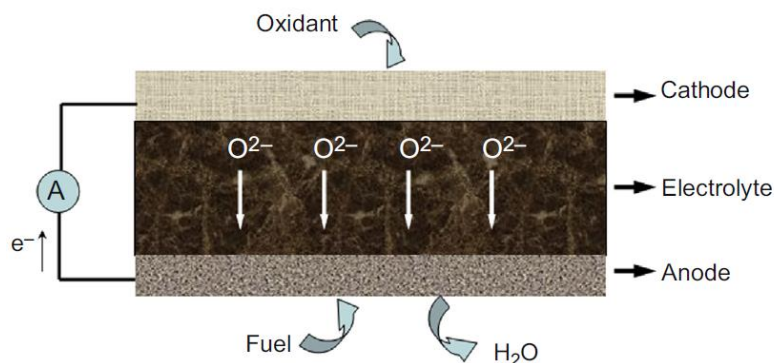


Fig. 2.17. Structure and operating principal of a solid oxide fuel cell [119].

The first aspect of categorization is the nature of the fuels used for power generation [120] which can be hydrogen [121], methanol [122], fossil fuels [121] or biomass-derived materials [123]. The second aspect is the catalysts compounds used to speed up the electrochemical processes regarding the different possible working temperature of the cell [124]. Solid oxide fuel cells (SOFC) are one of the most commonly used and efficient types of the fuel cells that operates at high temperature from 800 $^{\circ}\text{C}$ to 1000 $^{\circ}\text{C}$ [125]. SOFCs consists of a dense electrolyte

sandwiched between two porous electrodes (anode and cathode). State of the art electrolyte, anode and cathode are $ZrO_2/8Y_2O_3$ (YSZ), Ni-YSZ cermet and LSM-YSZ (Lanthanum Strontium Manganite, LSM), respectively [126].

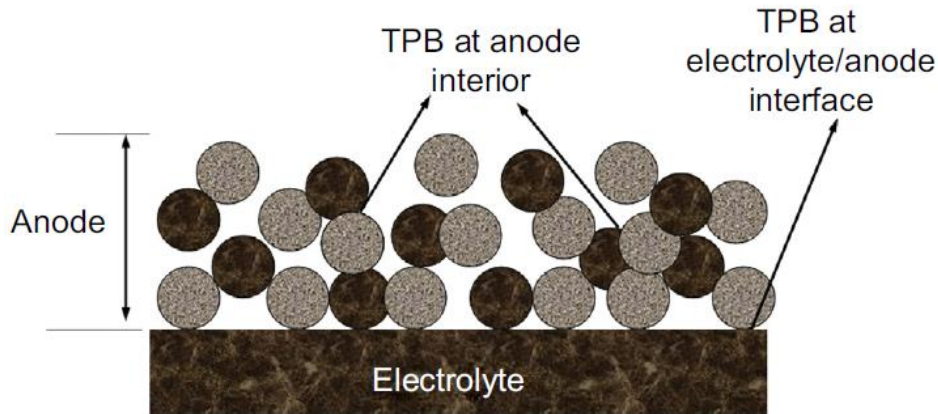


Fig. 2.18. A schematic diagram of triple phase boundary (TPB) at the anode side [119].

On the cathode side the oxygen from air is combined with electron from the external circuit to produce O_2^- ions. The O_2^- ions conductor are then travelling through the YSZ electrolyte towards the anode. On the anode side, the O_2^- ions react with the H_2 to produce water. Electrons are released as a result of this reaction and travel through the external circuit towards the cathode to repeat the same process. These reactions are summarized below:

Cathode reaction:



Anode reaction:



High anodic porosity is required to afford a proper way of gas diffusion throughout the anode. The point where Ni, YSZ and pore connect each other is called triple phase boundary (TPB) where the above electrochemical reactions take place (Fig. 2.18). The produced water molecule is transferred outside of the anode through the pores [127]. The construction aim is to provide a maximum possible number of TPBs to obtain as results the large number of reactions. Besides the

high porosity required for the anodic material, the anode must exhibit high electric conductivity, chemical and mechanical stability and compatibility with the other components. Among the most available metallic and ceramic materials that fulfil these requirements is the common Ni and YSZ cermet. This material is constructed in such a way that YSZ particles are percolating around the Ni particles. Ni / YSZ anode is considered as the most efficient anode material for SOFC for many reasons, first the wide availability of the raw materials Ni and YSZ makes this anode broadly commercialized and decrease the high cost of SOFC. On the other hand, in term of efficiency Ni/YSZ cermet proved high active electro-catalytic properties for hydrogen oxidation at high temperatures. Moreover, Ni has a higher thermal expansion coefficient as compared to YSZ which restricts its use as an anode material for SOFCs. Agglomeration of Ni is prevented by YSZ particles that tend to provide a similar expansion coefficient as that of electrolyte during the high temperature operating conditions [124, 128, 129]. Therefore, a suitable microstructure not only guarantees a high operating voltage but also augments the lifetime. The optimization of the amount and size of the two particles Ni and YSZ is often the main key factor toward achieving such a microstructure. Ni / YSZ cermet enables to reform various kinds of hydrocarbon fuels with steam at high operating temperature. Methane reforming can be fulfilled either internally or externally in SOFC. In the external reforming, the methane is converted to CO and H₂ before these gases are supplied to the fuel cell compartment. While, in case of the internal reforming the methane conversion to CO and H₂ occur inside fuel cell compartment. In fact, this concept has been considered as a more promising and advantageous design because of several reasons: the elimination of pre-reformer as well as the possibility of recuperating the thermal heat resulted from the endothermic steam reforming reaction during the charge transfer reactions that is responsible of electrical energy production [129,130]. The hydrocarbons are heterogeneously reformed within the anode structure by reacting with steam and CO₂ that are produced by electrochemical charge-transfer processes according to the following Eq. 2.26 [130]:



In steam reforming process the H₂ levels are higher because the additional steam produced from the reaction can participate in the reforming process. The CO₂ is available to participate as a

dry-reforming reactant. The kinetics of CO₂-reforming of CH₄ on Ni catalyst can be modelled within the framework of classical Langmuir–Hinshelwood kinetics. Results claimed that the maximization of the rate of the reforming reaction onto the anode results in maximization of the H₂ and CO concentrations at the anodic cell compartment. However, the internal reforming of methane often accompanies impurities such as carbon deposition denoted as cooking or sulphur deposition remain the major issues responsible for the fast anode deterioration. The presence of sulphur and intensive carbon deposition contributed to the delamination of anode layer and block the nickel grains. This fact caused the limitation of the hydrogen atoms movement and thus leads to a significant decrease of the cell efficiency [131]. *Cheng et al.* found that the formation of sulphide (Ni₃S₂, NiS) can be limited by a high cooling rate about 70 °C/min [3]. While the carbon deposition on the porous anode can occur in different forms such as fibers, whiskers or graphitic carbon causing micro morphological changes of the anode resulting in deactivation or breakdown of the catalysts [132]. Many recent studies proved that the temperature of sintering is an important parameter in obtaining a small grained structure for a better performance of SOFC electrolyte [133].

The active sites of the anode are covered with deposited carbon that can conduct to its deactivation, loss of cell performance and reduced SOFC reliability. High operating temperature is another big issue in SOFC and can cause many problems in terms of anode-electrolyte–cathode degradation and lifetime of the cells. The main challenge is the decrease of the high working temperature of fuel cells. *Liu et al.* identified and analyzed the main issues responsible for cathode degradation in SOFC [134]. The structural changes at the interface of LSM ((La_xSr_{1-x})_yMnO₃) / YSZ cathode and YSZ electrolyte introduced a reduction of the LSM craters and the formation of new phases of the insulating zirconate. The lack of oxygen content in the air introduced to the cathode gas was attributed as a major factor responsible of LSM craters reduction. Although, the high advantages arising from the development of fuel cells in term of sustainability and environment protection. We must not neglect the waste generated from hydrogen production during the calculation of the overall environmental impact of fuel cells compared to conventional energy sources. Therefore, the process of hydrogen manufacturing generally involves fossil fuels, biomass, or water. This manufacture costs time, capital, and energy. Then the hydrogen must be transported and stored. This also requires dedicated infrastructure.

Solid oxide-ion conductors are considered as vital components for various energy and environmental technologies. Major applications include solid oxide fuel cells (SOFCs), gas sensors, oxygen sensors for control of automotive emissions, de-oxidation of steel, combustion controls for furnaces and engines. Driving towards owning high efficient energy production and low air pollution, YSZ is regarded as one of the most reliable solid oxide-ion conductors due to its ability to create oxygen ion vacancies and hence enabling the transport of oxygen at high dopant amount (8–10 mol%, fully stabilized into cubic structure). Furthermore, YSZ is the most commonly effective material used as thermal barrier coatings (TBCs) for thermal protection in various technologies such as modern gas turbines, combustion engine components and hot structures (aerospace). The ceramics coatings with low thermal conductivity are good insulators and protect engine components from severe conditions namely high temperature/pressure and corrosive environment and thereby improves the engines efficiency and durability [2, 135, 136].

2.8. Aim of PhD work

Nowadays, MWCNT reinforced ZrO₂ composites are attracting growing interest, thanks to their ability of self-healing of the crack and the possibility to tailor the desired nanostructured properties. The PhD work are based on the following aims and motivations:

- **Synthesis of 8YSZ containing 1, 5 and 10 wt% MWCNTs** and analysing the critical role of milling conditions and spark plasma sintering process in the control of the grain size, density and MWCNT dispersion.
- **Analysing and characterizing of the MWCNT direct and indirect effect** on the microstructure and further on the sintered 8YSZ / MWCNT composites at 1400 °C.
- **Qualitative and quantitative examinations** to reveal the composites phase evolution at powder and sintered states and to further discern whether SPS process has affected MWCNT structure and integrity with respect to its concentration.
- **Evaluation of composite's mechanical properties**, mainly Vickers hardness, indentation fracture toughness and 3-p bending testes.
- Analysing the composites **ability of self-healing** by limiting the crack propagation (toughening mechanism) with respect to MWCNT content after surface indentation and fractographic test.

- **A new interpretation of the complex wear mechanism** reported in 8YSZ / MWCNT composites has been well outlined in function of MWCNT content, wear conditions and the variation of the applied sliding speed.
- **Understanding the complex wear mechanisms** observed in the studied composites at low $V_1 = 0.036$ m/s and high $V_2 = 0.11$ m/s sliding speeds, dry sliding conditions based on analytical studies involving SEM and EDS investigations inside and outside the wear track. Based on the obtained results, the studied composites can be extended towards technical applications where low wear rate associated with good strength and resistant to crack propagation are essential.

3. MATERIALS and EXPERIMENTS

This chapter provides a detailed overview of the composites synthesis procedure based on high energy ball milling and SPS sintering process. It also entails the experimental techniques for mechanical and tribological testing as well as reviews the various characterization methods such XRD, SEM, TEM and Raman spectroscopy.

3.1 Materials

The powder precursor composed of commercially available 8 mol% yttria stabilized zirconia (8YSZ, Sulzer Metco AMDRY 6643, Fig. 3.1a and Fig. 3.1c) with an average grain size of 40 μm was used as base material in the current study. The chemical composition of 8YSZ measured using energy-dispersive spectroscopy (EDS) is provided in Tab. 3.1.

Tab. 3.1. Chemical composition of the as received 8YSZ powder.

Elements	Composition in wt%
O	~ 31.23
Fe	~ 0.45
Y	~ 7.49
Zr	~ 58.45
Hf	~ 2.38

Catalytic chemical vapor deposition (CCVD) process has been employed to manufacture the MWCNTs with average wall numbers of eight, inner / outer diameter of 3.8 nm / 9.13 nm and average length of 1.5 μm (MWCNT, type NC3100TM, Nanocyl). The photos (Fig. 3.1b) as well as SEM micrographs (Fig. 3.1.d), illustrate the as received materials.

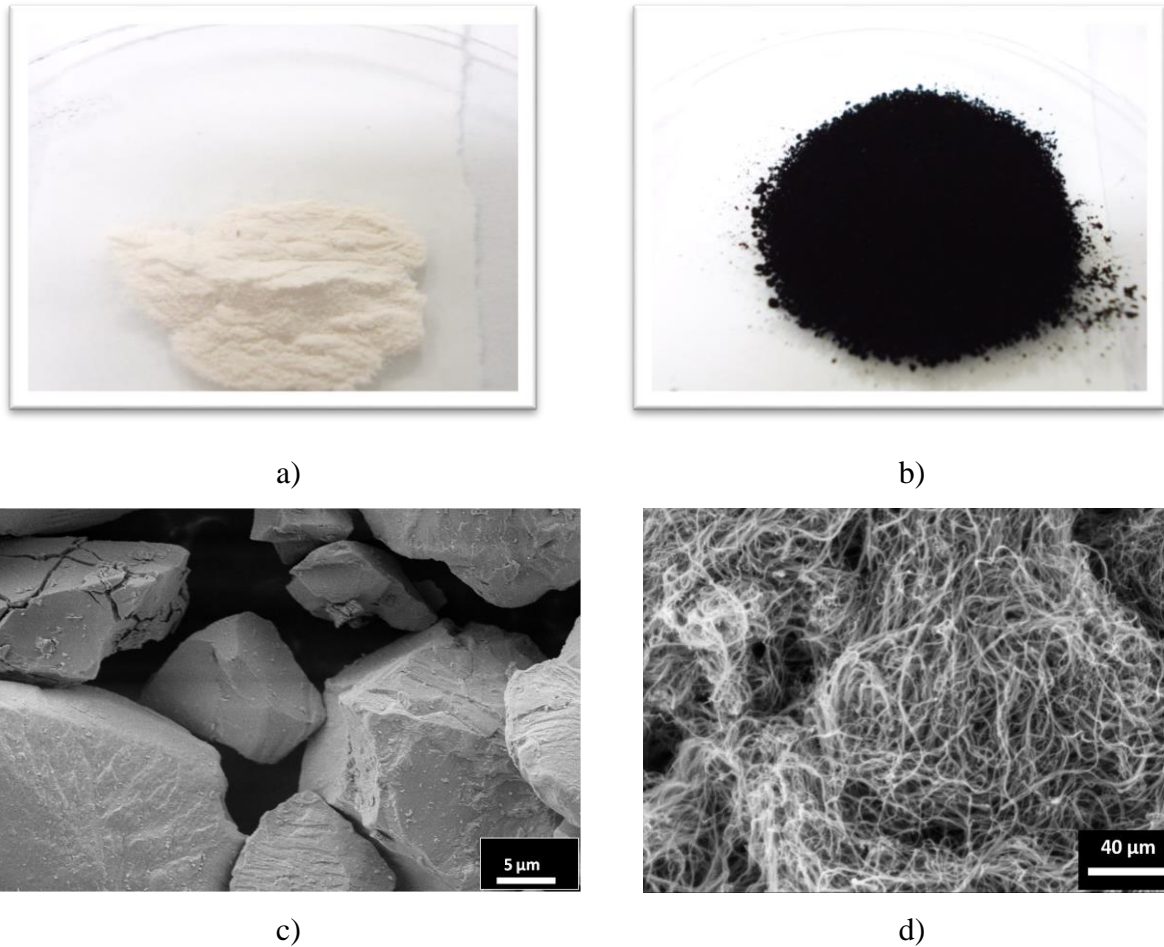


Fig. 3.1. Shape of as received zirconia powder a) photographic picture, b) SEM micrograph and MWCNTs bundles c) photographic picture, d) SEM micrograph.

3.2 Powder milling and sintering

As a first step of composite preparation, appropriate amounts of MWCNTs corresponding to 1 wt%, 5 wt% and 10 wt% (Tab. 3.2) were weighed out by electronic balance and added to zirconia powder. In order to obtain high MWCNTs dispersion and to increase the surface area of the grains by decreasing their size, the composites mixtures were milled for 5 h running at a velocity of 4000 rpm using high efficiency attrition milling (Union Process, type 01-HD/HDDM). Each batch with 80 g final product was mixed in zirconia tank (750 cm³) by 130 g ethanol and 280 mL zirconia balls (each of 1 mm diameter). The obtained milled slurry was then dried at 172 °C

for 25 minutes. Finally, the powder mixture was sieved by 100 μm mesh. The details of preparation are summarized in Fig. 3.2.

Tab. 3.2. Percentage of 8YSZ and MWCNTs in ZR, ZR-1, ZR-5 and ZR-10 composites.

Sample	8YSZ (wt%)	MWCNT (wt%)
ZR	100	0
ZR-1	99	1
ZR-5	95	5
ZR-10	90	10

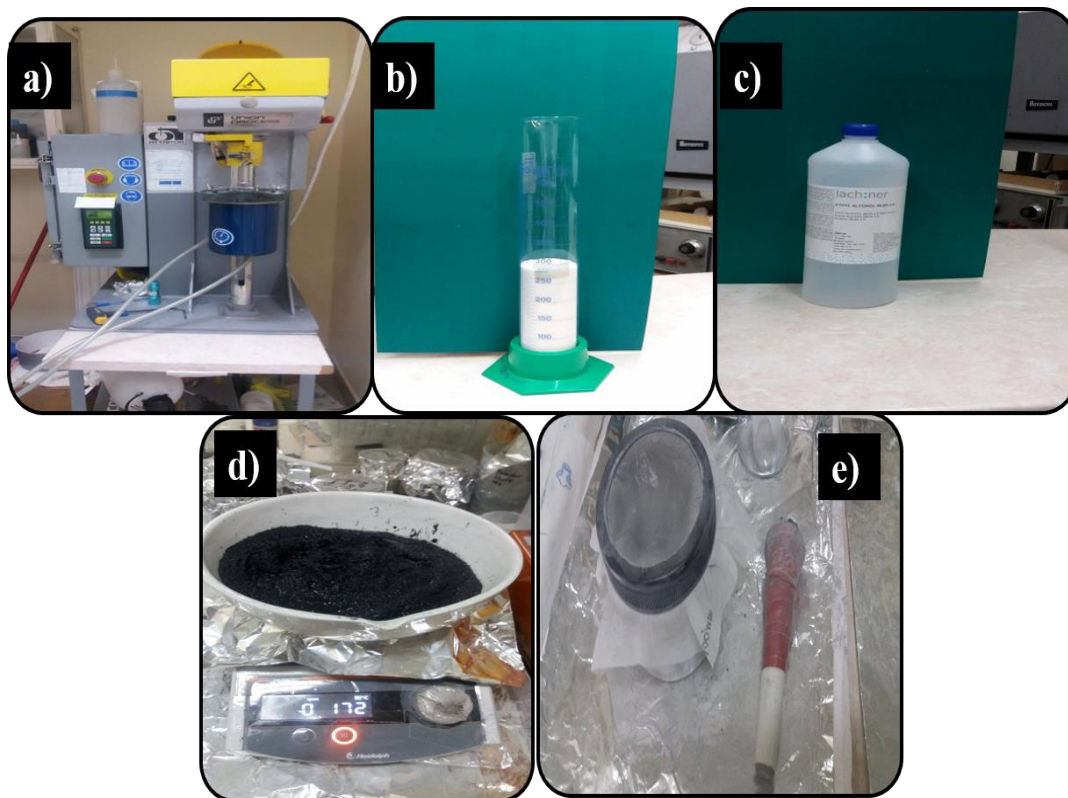


Fig. 3.2. Preparation of 8YSZ/MWCNTs powders using attritor milling technique in wet media. a) high efficiency attrition milling, b) zirconia balls, c) ethanol, d) powder drying and e) powder sieving.

After powder processing, the consolidation of composite powder was assessed by spark plasma sintering (SPS, HD P5 equipment FCT GmbH) (Fig. 3.3a) at 1400 °C using a graphite die. An optical pyrometer positioned on the upper graphite punch has been applied for temperature control. The powder mixtures were then heated under vacuum (1mbar) at a rate of 200 °C/ min⁻¹ with on/off current pulses of 3/1 ms, 2.2kA and 5V. A uniaxial pressure of 50 MPa was maintained during sintering cycle with a dwell time of 5 min. The final sintered pellets size was 30 mm in diameter with a thickness of 5mm (Fig. 3.4a). The pellets were grounded and polished using silicon carbide papers with abrasive grain size from 80 μm to 1200 μm. Additional polishing using polycrystalline diamond suspension has been applied for some samples to ensure the total removal of the graphite foil and to reveal their microstructure. Finally, the specimens were sawed into bars of about (4.8 mm × 4.4 mm × 30 mm) (Fig. 3.4b) by diamond saw (Struers secotom-50, Fig. 3.3b).

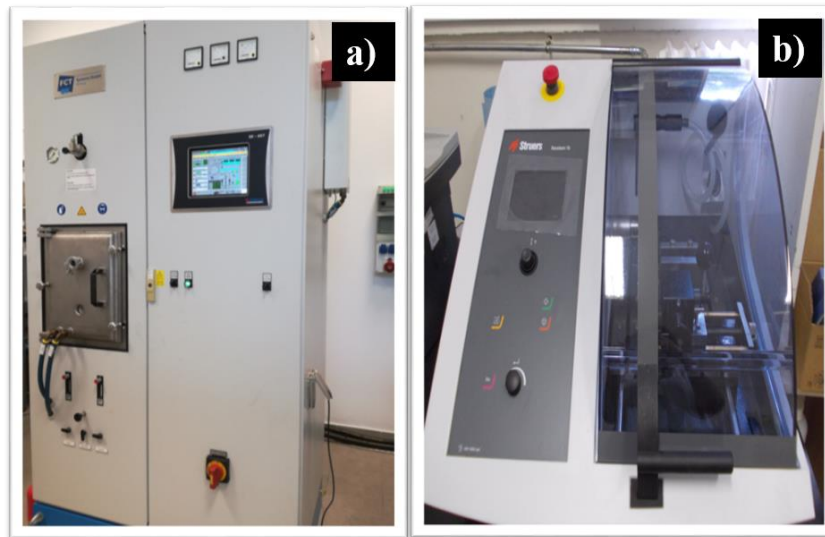


Fig. 3.3. a) Spark Plasma Sintering machine (HD P5 equipment FCT GmbH) and b) diamond cutting machine (Struers secotom-50) used in this work.

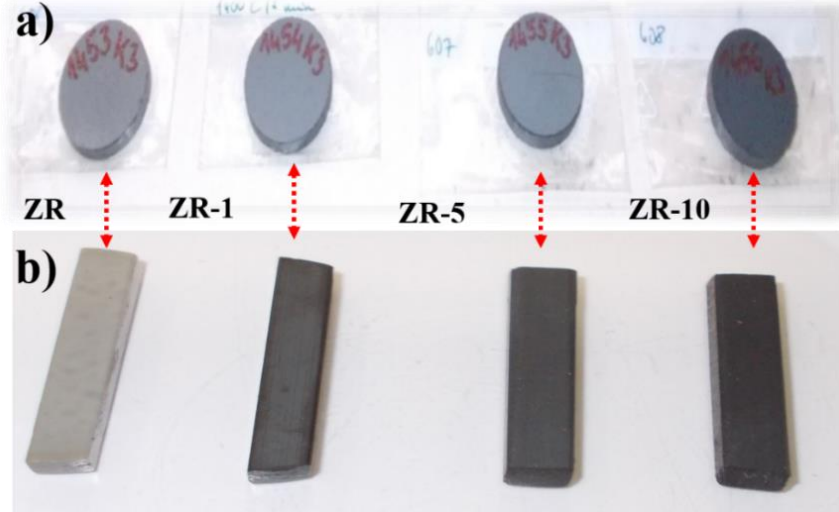


Fig. 3.4. Sintered samples. a) As-received samples after sintering (diameter/ thickness of 30 mm / 5 mm respectively), and b) the samples after a hard polishing and cutting process (bars of 4.8 mm × 4.4 mm × 30 mm).

3.3 Microstructural analysis, density and porosity measurements

The apparent and bulk densities of the composites were measured using Archimedes method (Eq. 3.1 and 3.2 respectively) with distilled water as the immersion medium. The bulk density is the mass divided by bulk volume. The later involves the volume of solid as well as the volume of open and closed porosity. While apparent solid density is the mass divided by apparent solid volume. Composites with high surface porosity containing 5 and 10 wt% (open pores) have been immersed into water + lubricant (soap) for at least 3 days to ensure the total filling of the pores. Further, the apparent porosities is defined as the mass of open pore volume divided by apparent solid volume. The apparent porosities of the composites were calculated according to (Eq. 3.3) [138].

$$\text{Apparent density} = \frac{\text{wt. of dry sample}}{\text{wt. of dry sample} - \text{wt. of soaked immersed sample}} \cdot \rho_{\text{Water}} \quad (3.1)$$

$$\text{Bulk density} = \frac{\text{wt. of dry sample}}{\text{wt. of soaked sample} - \text{wt. of soaked immersed sample}} \cdot \rho_{\text{Water}} \quad (3.2)$$

$$\text{Apparent porosity} = \frac{\text{wt. of soaked sample} - \text{wt. of dry sample}}{\text{wt. of soaked sample} - \text{wt. of soaked immersed sample}} \cdot 100 \quad (3.3)$$

where, ρ_{Water} is water density equal to 1g/cm^3 at room temperature, (wt.) refers to the weight in (g).

3.4 Mechanical and tribological testing methods

3.4.1 Vickers hardness and indentation fracture toughness

Vickers hardness tester (Leitz Wetzi AR Germany, Fig. 3.5) has been used to indent the well-polished specimens surface with applied load of 19.61 N and 30 s a dwell of time. The mean diagonals length (d) has been measured after removing the diamond indenter which is in the form of a square-based pyramid with an angle of 136 degrees between the opposite faces. 7 indents have been performed throughout the sample's surface diagonal with a displacement step of 4 mm, to investigate the hardness homogeneity. The Vickers hardness values were calculated according to the Eq. 3.4 below:

$$H_v = \frac{189 \cdot F \cdot 10^3}{d^2} \quad (3.4)$$

where, F is the applied load (N), d is the diagonal length (μm).

Indentation fracture toughness (K_{IC}) was obtained using the valid equation (5) for Palmqvist crack proposed by Shetty:

$$K_{IC} = 0.0899 \left(\frac{H_v \cdot F}{4l} \right)^{0.5} \quad (3.5)$$

where, l (mm) is the length of the crack from the indentation corner.

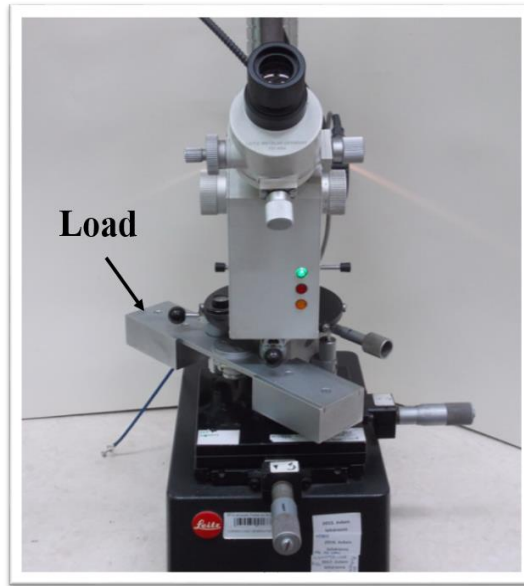


Fig. 3.5. Vickers hardness indenter (LeitzWetzi AR Germany) used in this work.

3.4.2 Bending strength

The 3-point bending test is a classical mechanical testing method commonly used due to its simplicity to determine the bending strength, stress-strain behaviour, and the elasticity modulus of brittle material such as ceramics. The geometry of the tested sample and strain rate are so essential for an easy result analysis. Therefore, the sample should be cylindrical rods or rectangular bars since the sample geometry has to be taken into account in the final calculation. Additionally, the sample should be flat as much as possible to ensure avoiding its rotation when the loading pin contacts the sample. In the 3-point bending tests, the bar-shaped sample is placed on two cylindrical rods (lower supports), while the third rod is placed on the middle of the upper surface of the sample and cause a concentrated load at mid-point and reduced stress elsewhere. This strength testing configuration creates a compression stress in the concave side, tensile stress in the convex side of the sample and shear forces along the middle plane. Hence, to prevent the contribution of the shear stresses primary failure of the material rather from the compressions or tensile stresses, the control of the ratio between the span and depth (height of the sample) is necessary to reduce shear stresses [139–141]. The theoretical model of the 3-point bending is given in Fig. 3.6a.

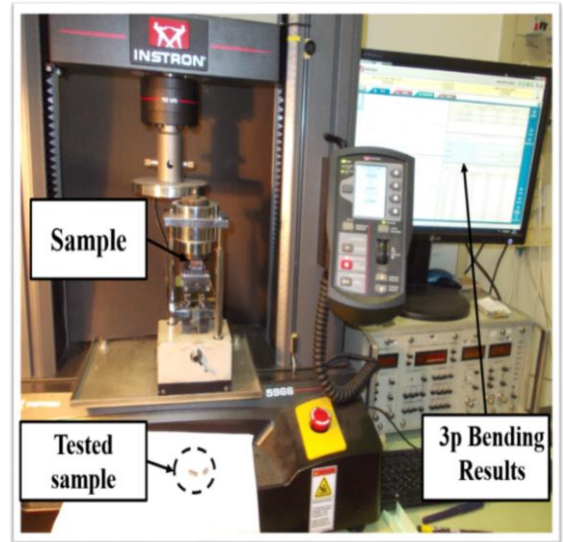
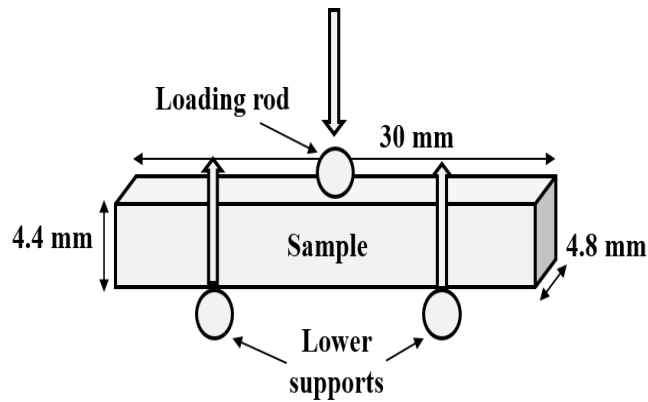


Fig. 3.6. 3-point bending test. a) schematic of the 3-point bending test conducted on the bar shaped used in this work., b) bending strength test set up (INSTRON 5966) used in this work.

In this work, 3-point bending test was conducted using apparatus INSTRON5966 (Fig. 3.6b), a span of 20 mm and rate of 0.0083 mm/s. The flexural test σ_{B3} (maximum stress at break) was calculated as follows:

$$\sigma_{B3} = \frac{3FL}{2bh^2} [\text{MPa}] \quad (3.6)$$

where F is the load at the fracture point (N), L is the length of the support span (mm), b is the width (mm) and h is the thickness (mm) of the specimen. The elastic modulus (E) is determined mechanically from the linear region where the stress and strain exhibit a proportional relationship. In that region, the elastic modulus constant in the 3-point bending strength can be calculated according to Hooke's Law [65].

$$\sigma = E \cdot \varepsilon \quad (3.7)$$

where σ is the measured stress (Pa), E is Young's modulus (Pa), and ε is the displacement (mm/mm). In 3p-bending strength test, the elastic modulus constant can be expressed as follow:

$$E = \frac{\sigma_{B3}}{\varepsilon} = \frac{FL^3}{4bh^3\delta} \quad (3.8)$$

where δ is the deflection corresponding to the load.

3.4.3 Wear test

The analysis of the wear behaviour and friction determination has been conducted on high temperature tribometer THT (CSM, Switzerland) using ball on disk technique at room temperature (25 °C, air humidity 50–65 %) (Fig. 2.8a). This method most commonly used in tribology as an important tool to investigate the maturity of a given material (in term of friction and wear) enables in fact setting up various parameters such as: time, temperature, velocity, contact pressure, lubrication, and humidity, as similar as the real conditions for which the material is designed for.

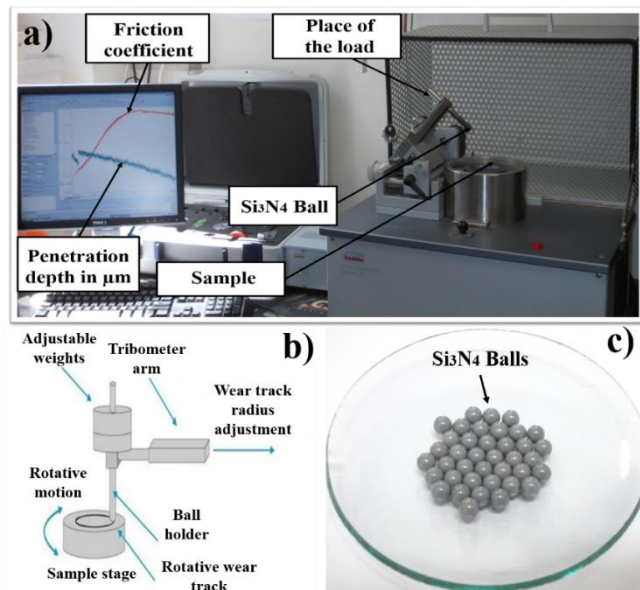


Fig. 3.7. a) High temperature tribometer THT (CSM, Switzerland) machine used in this work, b) schematic of ball-on-disk method, and c) Si_3N_4 balls used as counterpart against the composites surfaces.

The frictional forces between the sample in rotation and the ball are measured with the help of a strain gauge sensor on the arm (Fig. 2.8b). Commercially available Si₃N₄ balls (Fig. 2.8c) with 5 mm in diameter, H_{v10} = 1300 N/mm² in hardness and Ra = 0.025 μm in roughness, were used as counterparts against the sintered 8YSZ and 8YSZ / MWCNT composites surfaces. The friction coefficient (μ) has been recorded throughout the test with acquisition rate of 5.4 Hz at fixed normal load (5 N) and total sliding distance of d = 400 m. The speed velocity has been set up at V1= 0.036 m/s then V2= 0.11 m/s to study its influence on tribofilm formation and friction behaviour. The wear rates (W) were measured based on the volume loss (V) per total sliding distance (d) according to the following Eq. 3.9:

$$W = \frac{V}{d} \left[\frac{\text{mm}^3}{\text{m}} \right] \quad (3.9)$$

3.5. Structural characterization of samples

3.5.1 Scanning electron microscopy

The scanning electron microscopy (SEM) principle is based on using the electron-matter interactions mechanism to visualize and produce high-resolution images. SEM is equipped with electron gun system (to produce high-energy electron beam which enters the electron column), electromagnetic lenses (condenser lenses, objective lenses and scanning coils), vacuum system and detector. The electromagnetic system allows successive interventions to control the beam size, focus and scan the beam on the sample in a small spot. The vacuum system is necessary to avoid contamination and collision, while the detector receives the current of secondary electrons emerged during the beam-sample interaction. In addition, diaphragms of optimum aperture diameter are placed to reduce or exclude dispersed beam electrons. The incident electron beam interacts with the orbiting electrons of the atoms at the surface of the specimens in a variety of ways giving rise to various signals that carry information about the sample namely: secondary electrons, backscattered electrons, Auger electrons, light or X-rays. The various types of specimen out coming derived from electron- specimen interaction are then collected by different the

detectors depending on the types of the generated radiation. The latter, are then converted to signal that is sent to a screen similar to a television screen to form the final image (Fig. 3.8a). The analysis of these alternative energy forms release information about the specimen such as topology, morphology, chemical composition, crystallography and grains orientation.

The most important key advantages of this method are its ability to image bulk samples up to many centimeters in size, besides its great depth of field allowing imaging three-dimensional shapes. Another advantage of SEM is its variety called environmental scanning electron microscope (ESEM), which can produce images of sufficient quality and resolution with the samples being wet or contained in low vacuum or gas [142–146].

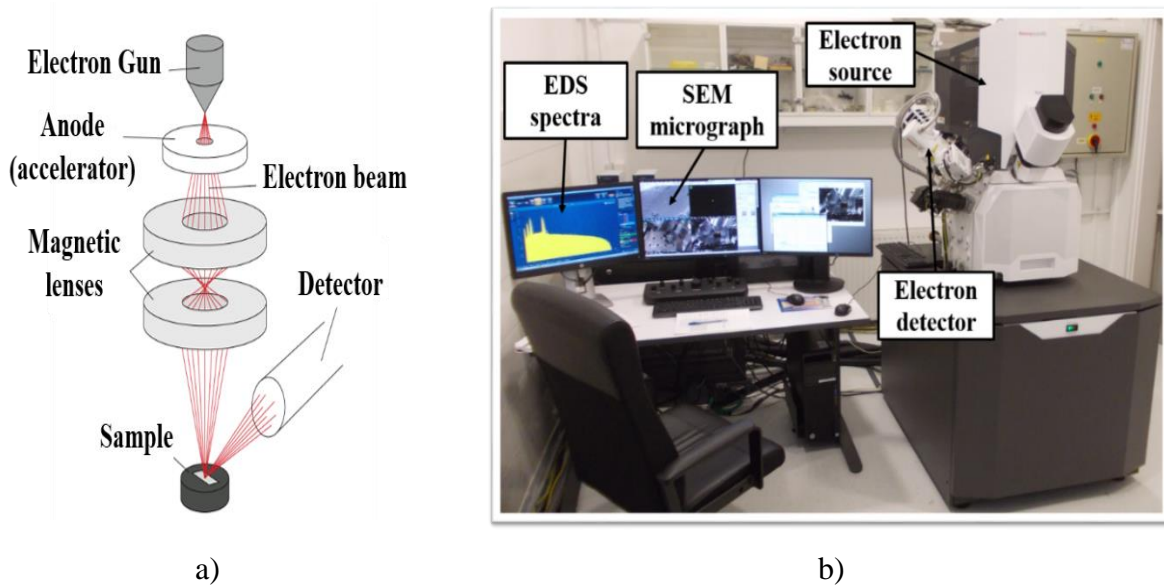


Fig. 3.8. Scanning electron microscope (SEM). a) operating principal, b) working set up.

The microstructural characterization of the studied composites such as: the MWCNTs dispersion, zirconia grain size and morphology, surface porosity and preliminary fractographic examination were investigated by a field emission scanning electron microscope (LEO 1540 XB) equipped with Everhart-Thornley and InLens secondary electron detectors. Additionally, the SEM equipped with ultrathin window Rontec Si (Li) EDS detector and Bruker Esprit 1.9 software, was used for visualizing MWCNT agglomeration and dispersion into the matrix based on elemental maps as well as employed upon the Vickers indentation impression of each sintered sample to confirm the presence of different toughing mechanisms (MWCNT pull-out, crack bridging, crack

deflection). A Thermo Scientific Scios 2 (SEM, Fig. 3.8b) equipped with BSE detector and Oxford X-Max EDS detector were used up on the wear track profile to analyse the wear mechanism and to identify the chemical composition evolution after the wear test.

3.5.2 Transmission electron microscopy

Transmission electron microscopy (TEM) device is constructed by six main components: electron beam cathode (generally: tungsten lanthanum hexaboride (LaB₆ - often called “lab six”), field emission gun (FEG)), magnetic condenser lenses, objective lens, projective lenses, apertures and fluorescent screen. Every component plays an important role in producing images with a higher resolution and magnification as it is described in Fig. 3.9. The role of the condenser lens system is to focus the electron beam onto the specimen. The electron beam passes through the specimen and carries information about its structure at atomic scale. Then, the emerged beam is collected and focused by the objective lens, which is followed by several projection lenses used to focus, magnify, and project the image onto the viewing device at the bottom of the column. The entire electron path from gun to camera must be under vacuum otherwise the electrons would collide with air molecules and be scattered or absorbed. On the way from the source to the viewing device, the electron beam passes through a series of apertures with different diameters. These apertures stop those electrons that are not required for image formation (e.g., scattered electrons)[146–148].

Originally, TEMs used a fluorescent screen, which emitted light when impacted by the transmitted electrons, for real-time imaging and adjustments; modern instruments rely primarily on solid state imaging devices, such as a CCD (charge-coupled device) camera, for image capture. They may still include a fluorescent screen, but it may be observed by a video camera.

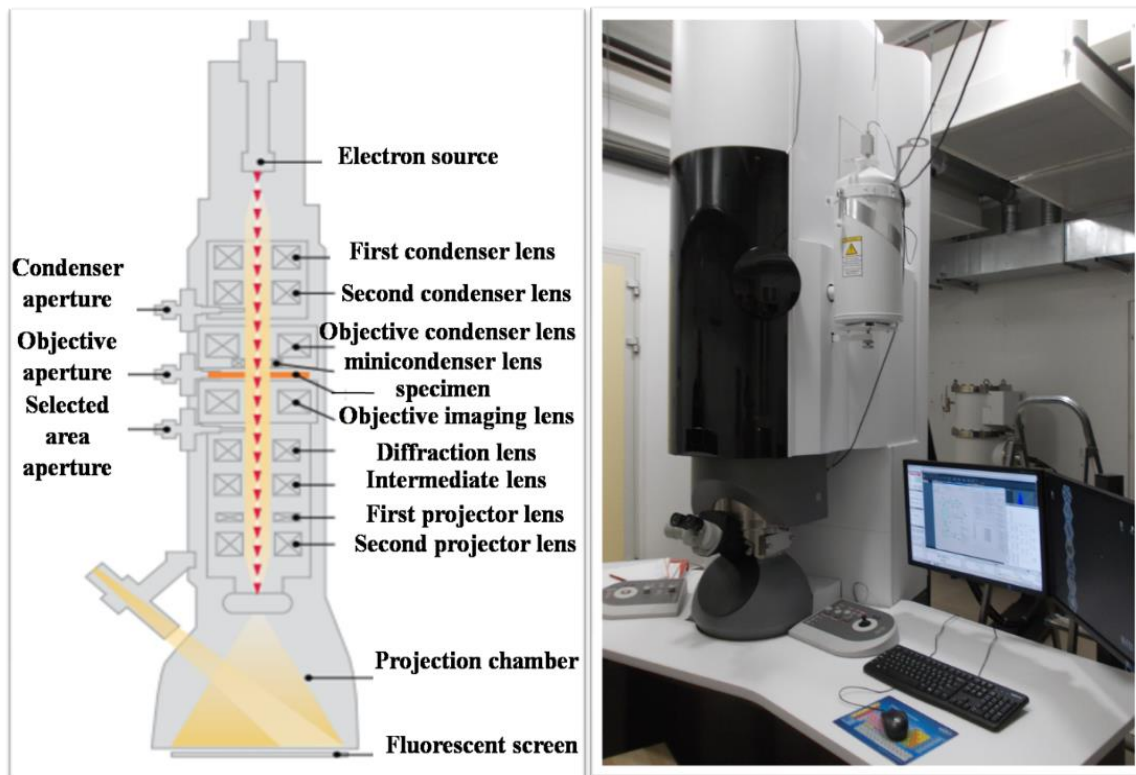


Fig. 3.9. TEM operating principal and the real device used in our laboratory.

The features of the dispersed MWCNTs in 8YSZ powder at different concentrations were examined in detail using transmission electron microscopy (Philips CM-20) and high resolution transmission electron microscopy (JEOL 3010 with 300 kV accelerating voltage and Cs- corrected Themis with 200 kV accelerating voltage). The evaluation of SAED images was done in process diffraction software with the help of a free crystallographic database.

Only the powder samples were studied by TEM. The Cu grid was used for sample preparation.

3.5.3 Digital microscopy

KEYENCE VHX-950F digital microscope equipped with a high-sensitivity, high-speed CMOS camera with a framerate of 50 frames/sec was used to evaluate the wear track profile of samples after the wear test. Depth composition images were obtained of the uneven surfaces by compiling images at different focal planes. Therefore, the average arithmetic roughness (Ra) could be measured.

3.6. Phase analysis of samples

3.6.1 X-Ray Diffraction

X-ray diffraction (XRD) technique is a non-destructive method to analyse and characterise all kinds of matters (fluids, powders and crystals). In fact, X-ray diffraction technique allows an easy and rapid identification of a specific phase, the orientation of grains or single crystals, atomic arrangement (material structure), grain size or internal stress. These important features enable researchers to understand a behaviour and function of a specific or unknown material. The principle of X-ray diffraction lies on the elastic scattering of an incident X-ray beam by atoms in a periodic structure. The X-ray beams are diffracted at specific angle 2θ and interfere either constructively or destructively. Constructive interference occurs when the scattered rays have a path difference of $S=n\lambda$ (n is an integer), so-called in phase. Otherwise, the scattered rays interfere

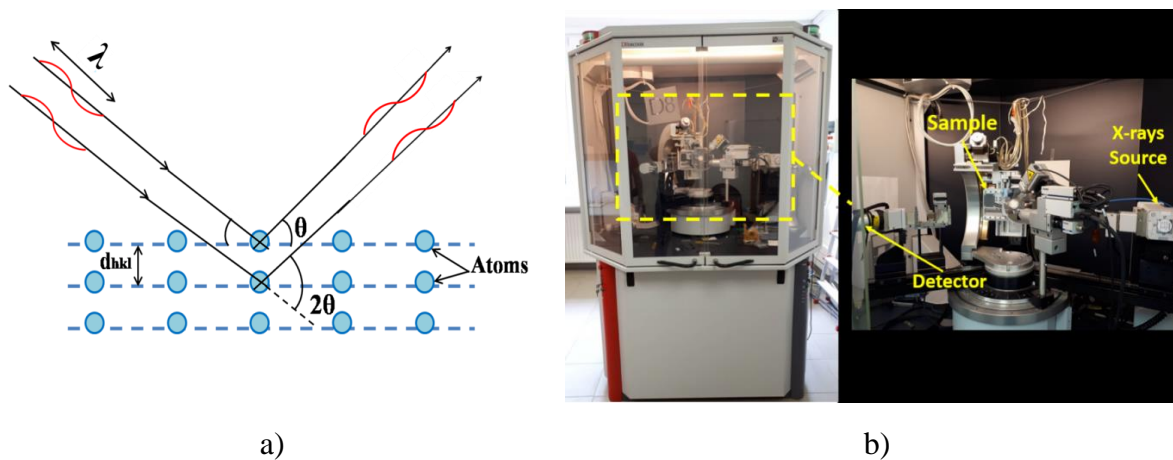


Fig. 3.10. XRD measurement. a) Principle of the X-Ray diffraction technique b) Picture of X-Ray device used during this work: Bruker D8 discover in the Bentano configuration using Cu K-alpha radiation ($\lambda = 1.54060 \text{ \AA}$).

destructively when they have a path difference of $S \neq n\lambda$, the so-called out of phase. The only considered scattered X-ray beams are the constructively diffracted ones which denotes the crystallographic structure of the matter by reflecting all the parallel planes of atoms intersecting the axes of the crystallographic unit cell, symbolized by the Miller indices (hkl) as illustrated in

Fig. 3.10a. In fact, the constructive interference of the reflected X-rays only occurs when Bragg's law is satisfied according to the following Eq. 3.10:

$$n\lambda = 2d \sin \theta \quad (3.10)$$

where n is an integer called the order of reflection, λ is the wavelength of X-rays, d is inter-planar spacing and θ is the angle between the incident beam and the normal to the reflecting lattice plane. Based on this relationship, the inter-planar spacing d can be calculated after measuring the angles θ under which the constructively interfering X-rays leave the crystal. The corresponding d -values together with the relative intensities of the recorded diffraction pattern are then compared with known standards line patterns in the JCPDS database. Further, a prior knowledge of the chemical features and the class of the tested material can be valuable. On the other hand, the peak angles and profiles can be used to quantify the average crystallite size and degree of crystallization as well as micro strain.

The Scherrer equation relates crystallite size to the peak width at half maximum according to the following Eq. 3.11:

$$\langle L \rangle = \frac{K \lambda}{\beta \cos \theta} \quad (3.11)$$

where $\langle L \rangle$ is the crystallite size, λ is the x-ray wavelength, β is the peak width at half maximum, K is a constant which is often taken as unity [149–151].

In this study, X-ray diffraction (XRD) was carried out on the composites at powder as well as sintered state to identify the existent phases and to quantify the crystallite size and phase composition. For this, XRD with parallel beam geometry and Cu $K\alpha$ radiation using a Bruker AXS D8 Discover diffractometer equipped with Göbel-mirror and a scintillation detector has been used. The corresponding XRD equipment is illustrated in Fig. 3.10b. Furthermore, the crystallite size and amount of phases existing in the composites has been preceded based on A standard less quantitative analysis of the composites was performed using the Bruker Diffract. EVA software based on the ICDD JCPDS 2003 database. Standardless quantitative analysis method is based on the comparison of the peak intensities of the identified phases to the intensities of a corundum standard [152].

3.6.2 Raman spectroscopy

Raman spectroscopy provides a qualitative and quantitative information in a host of materials and different physical states by exploring their molecular vibrations. The spectral patterns is the unique fingerprinting of a given material which permit to find out the constituent particles in a sample. In addition, further properties can be derived from Raman spectrum for instance the quantity which is proportional to peak intensity, strain/stress states, and quality of crystal.

Raman effect arises when the inelastic scattering of monochromatic light occurs. In other words, when the frequency of the incident laser beam changes upon interaction with a sample. The interaction can be observed as a perturbation of the molecule's electric field and associated with a change in vibrational, rotational or electronic energy of a molecule. The elastic scattering of light known as Rayleigh scattering occurs when the excited electron within the material return back to the same energy level and therefore in this case the scattered photons have exactly the same frequency as the incident photon. Most of the sample-laser beam interactions (about 99.999% of all incident photons) undergo an elastic scattering (Rayleigh scattering) which is useless for Raman chemical characterization. However, a small fraction of the incident light (approximately 0.001%) produces the Raman effect by inelastic scattering at optical frequencies higher or lower than original incident monochromatic frequency. Stokes frequency is the frequency of the scatter photon shifted to lower value compared to the incident photon, while Anti-Stokes frequency is the inverse situation when the resulted frequency of the scatter photon is shifted to higher values. The Raman spectrum consists of a plot of intensity of scattered light versus energy difference the incident and the scattered photons [153].

In this work, Renishaw 1000 B micro-Raman spectrometer attached to a Leica DM/LM microscope was used to produce Raman spectra at room temperature in the wave number range of 150–3500 cm^{-1} with 488 nm laser excitation. The spectral resolution of the system is 2.5 cm^{-1} and the diameter of the excitation spot is 1 μm .

4. RESULTS

This chapter reports on the microstructural, mechanical and tribological characterization of the 8YSZ composites containing 0, 1, 5, 10 wt% of MWCNTs addition. In the first part, the role of high efficient attrition milling on the microstructure, homogeneity and grain size of 8YSZ / MWCNTs powder was investigated in details. Further, the morphology and the distribution of MWCNTs in these powder mixtures was systematically researched. Additionally, the effect of SPS process at 1400 °C and MWCNT content on the microstructural features including density, phase transition, crystal size and composites cross sectional surfaces is reported. The second part will also focus on the mechanical characterization of the sintered 8YSZ / MWCNTs. The Vickers hardness and indentation fracture toughness distribution was evaluated based on seven indentations along the surface diagonal of the composites. Further, the crack propagation mechanism as well as the different toughening mechanisms associated with MWCNT reinforcement was deeply identified and analysed. Fractographic characterization based on SEM micrographs was accomplished on the composites subjected to 3-point bending test. The third part presents the wear test results conducted against Si₃N₄ balls at two different sliding speed namely (V1= 0.036 m/s and V2= 0.11 m/s). A novel interpretation of the wear mechanism is reported based SEM and EDS investigations.

4.1 Structural properties of the milled 8YSZ / MWCNTs powders

4.1.1 Structural study of the as-received 8YSZ powder before and after milling

The characterization of the as received material before and after milling involves as a first step the evaluation of the grain size and their distribution, besides the determination of the particle's morphology by SEM, TEM and EDS. The High energy ball milling process is a popular mechanical technique used to obtain a reduced and homogeneous particles size and shape. In fact, the process acts as a good mechanical dispersive tool to achieve a uniform MWCNT dispersion into matrix phase as well as minimizing their agglomeration especially when a fairly ductile binder is used to broke these agglomerations. The milling parameters such as time, speed, ball to powder

ratio and milling medium are of a great importance to control the microstructural features and milling efficiency [154].

The as-received 8YSZ powder presents generally a coarse microstructure with inhomogeneous particle size: bigger particle with an average of $33.48 \pm 7.45 \mu\text{m}$ and an average of $16.22 \pm 3.5 \mu\text{m}$ in case of the small ones (Fig. 4.1a). Furthermore, it can be observed that different morphologies are existing, but the majority of particle shapes seems to be irregular with significant sharpness at the edges. This particle shape arrangement gives the evidence of high separation between particles edges as well as a good dispersion. According to SEM micrograph illustrated in Fig. 4.1b, 8YSZ powder morphology has been modified after milling process. In fact, the grain size falls moderately to nanocrystalline structure due to many factors resulted from high milling speed during 5 h such as: grain dislocation, generation of grain strain and particles fracturing.

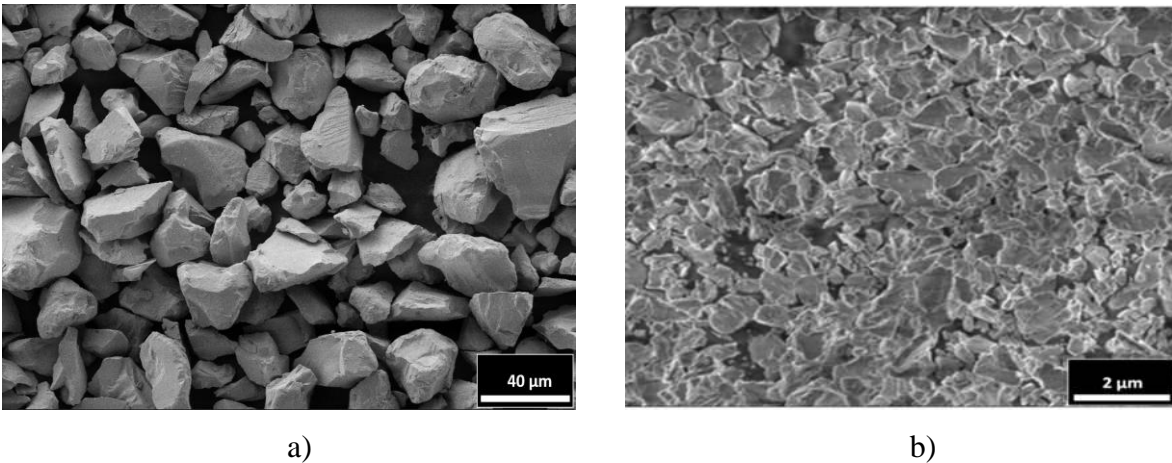


Fig. 4.1. Structural investigation of 8YSZ base material. a) SEM micrograph of the as received 8YSZ before and b) after milling process.

The particles disintegrated into fine grains with an average size approximately about 400 nm. Further, the milled grains appear softer at edges compared to the as received structure and tend to form low-angle grain boundaries due to repeated welding during the milling.

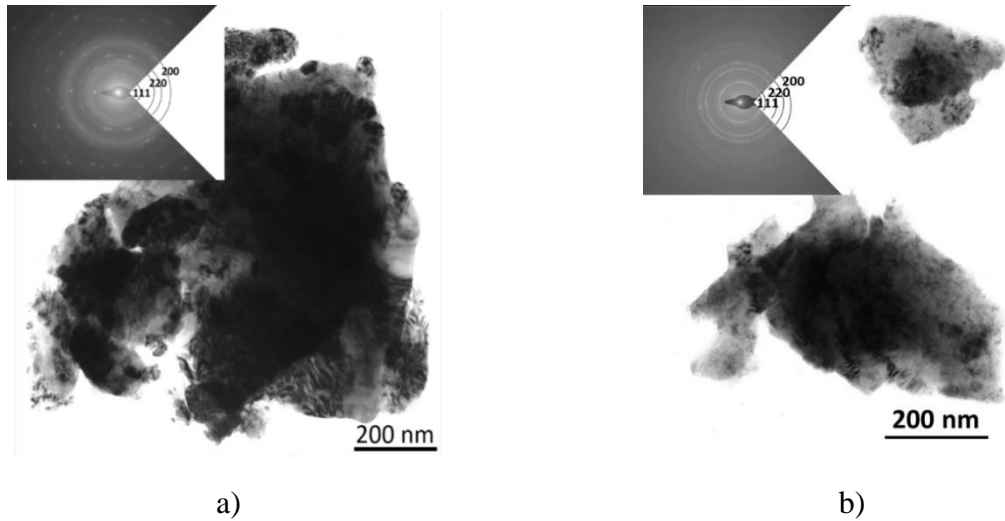


Fig. 4.2. TEM images of 8YSZ with SAED diffraction in detail. a) 8YSZ before milling, b) 8YSZ after milling. The SAED confirmed the cubic zirconia (111, 220, 200) in both cases.

Structural analysis conducted up on a fraction of 8YSZ powders before and after milling (Fig. 4.2) confirmed the previous SEM observations residing in obvious particle size decrease. Additionally, the phase analysis (Fig. 4.2) of powders indicates that milling effect did not result in phase transformation (cubic zirconia (111, 220, and 200) in both cases) but only grain decrease.

4.1.2 Structural analysis of 8YSZ reinforced MWCNT powder after milling process

In the composites containing MWCNTs the microstructure undergoes a substantial modification from zirconia particle sizing view and their surface topology in comparison with the milled reference (ZR) as discussed previously. Structural investigations (SEM, Fig. 4.3 and TEM, Fig. 4.4) of the milled 8YSZ / MWCNT powders (ZR-1, ZR-5, and ZR-10) showed the evidence of higher grain refinement resulted from MWCNTs addition. Moreover, zirconia grains tend to contact each other owing to the presence of MWCNT fibers on their surfaces. In ZR-1 composite, an enhanced MWCNT dispersion along the contact edges of the grains was observed. However, small spherical particles with diameters of about $1.42 \pm 0.4 \mu\text{m}$ corresponds to MWCNT agglomeration that could not be suppressed by ball milling were still visible. These agglomerations of MWCNT were bigger in case of ZR-5, and ZR-10 composites about $1.87 \pm 0.39 \mu\text{m}$ and $2.5 \pm 0.2 \mu\text{m}$ respectively. This resulted in the formation of small zirconia grains ($< 100 \text{ nm}$) and particles ($> 200 \text{ nm}$) embedded into MWCNTs agglomerations and networks. The agglomeration,

the damage or structural defect of MWCNTs has been reported as significant issue responsible for a reduction in the reinforcement of ceramic / MWCNT composites. On the other hand, the current findings are in good accordance with the study performed by *Melka et al* [155]. The refinement of the YSZ grain sizes up to 2 wt% of MWCNT used for powder mixture processing was confirmed. Indeed, when the agglomeration of MWCNT occurs, the real amount of MWCNTs located in the grain boundaries is decreasing. Therefore, the agglomerated CNTs introduce heterogeneity and in most case decrease in the functional properties of the composites [156–158].

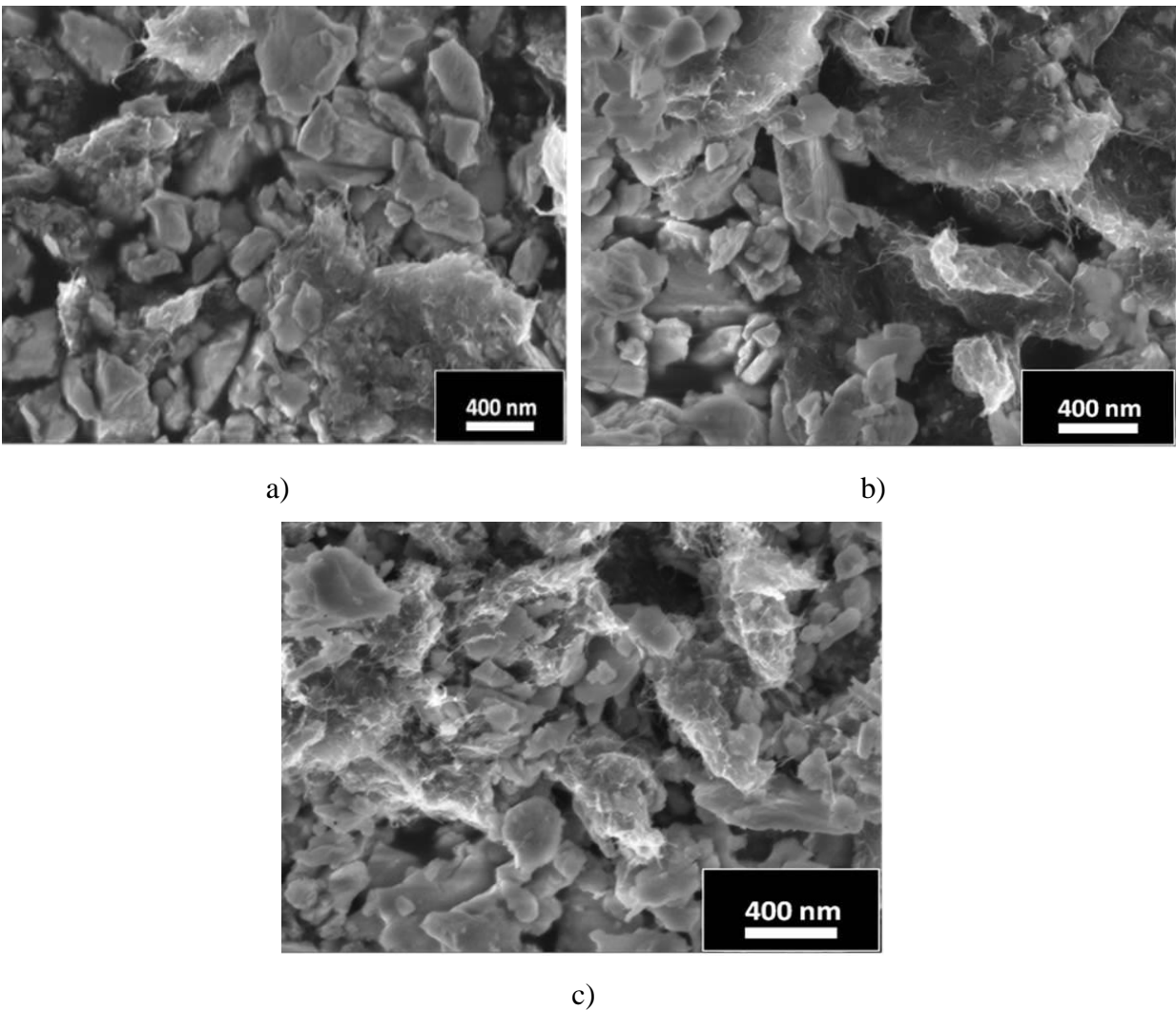


Fig. 4.3. SEM micrographs of milled composites. a) ZR-1, b) ZR-5 and c) ZR-10.

From the point of MWCNTs structure, non-destructive milling process is confirmed by HRTEM image illustrated in (Fig. 4.4a-c). The MWCNTs appeared as fine fibers forming several

bundles. The MWCNTs have an average inner diameter 3.8 nm, an average outer diameter 9.13 nm and the number of layers varied from 7 to 9.

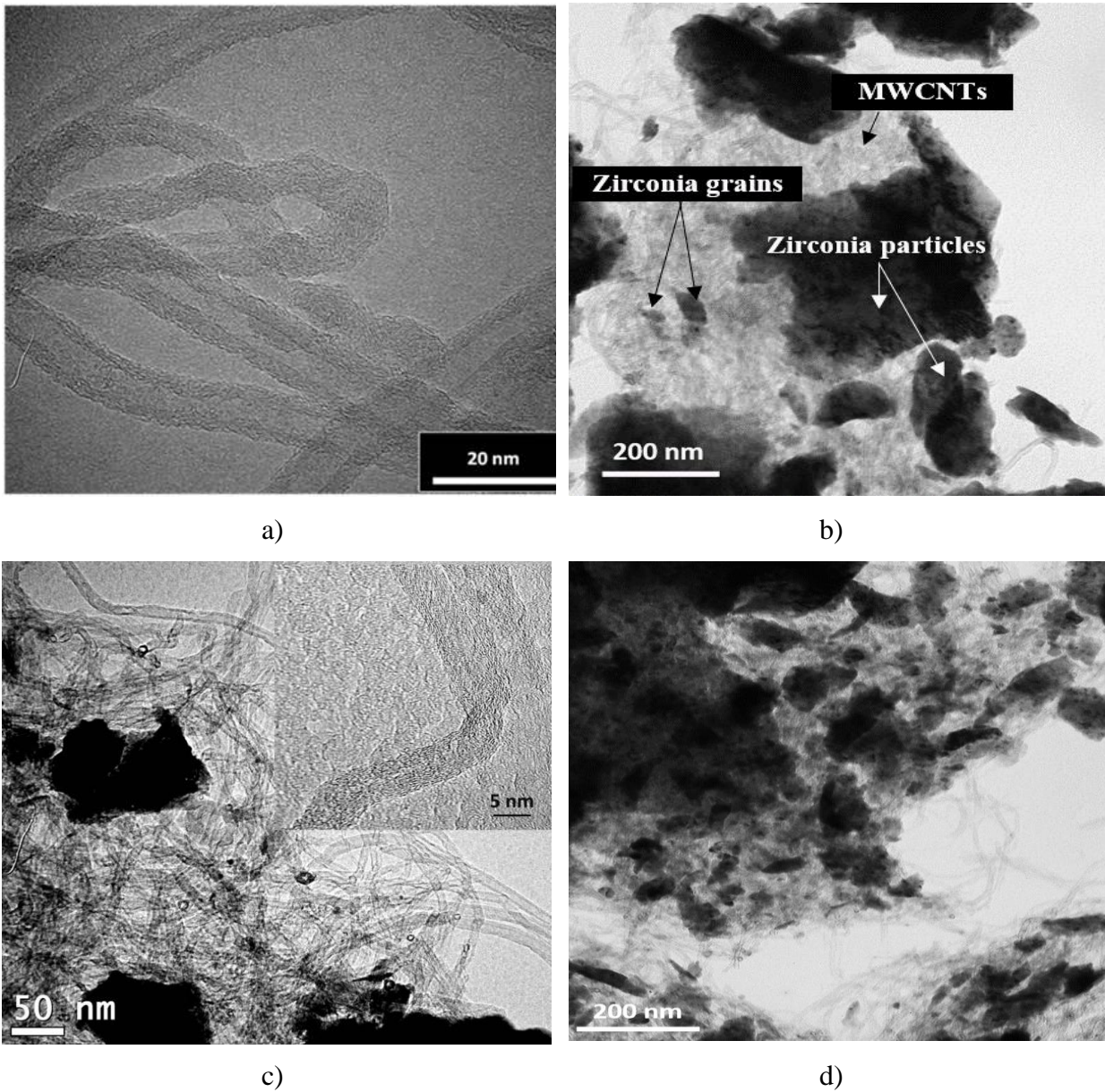


Fig. 4.4. Structure of milled composites. a) TEM images of MWCNT, b) ZR-1, c) ZR-5 with detail of MWCNT and d) ZR-10.

EDS elemental analysis illustrated the features of MWCNTs distribution in zirconia matrix (Fig. 4.5). This study confirmed the SEM and TEM results showing the increase of MWCNTs agglomerations proportionally with concentration (ZR-1 → ZR-5 → ZR-10) as well as their dispersion into 8YSZ phase. The MWCNTs agglomerations (C-red) were surrounded by ultrafine rounded zirconium (Zr-blue).

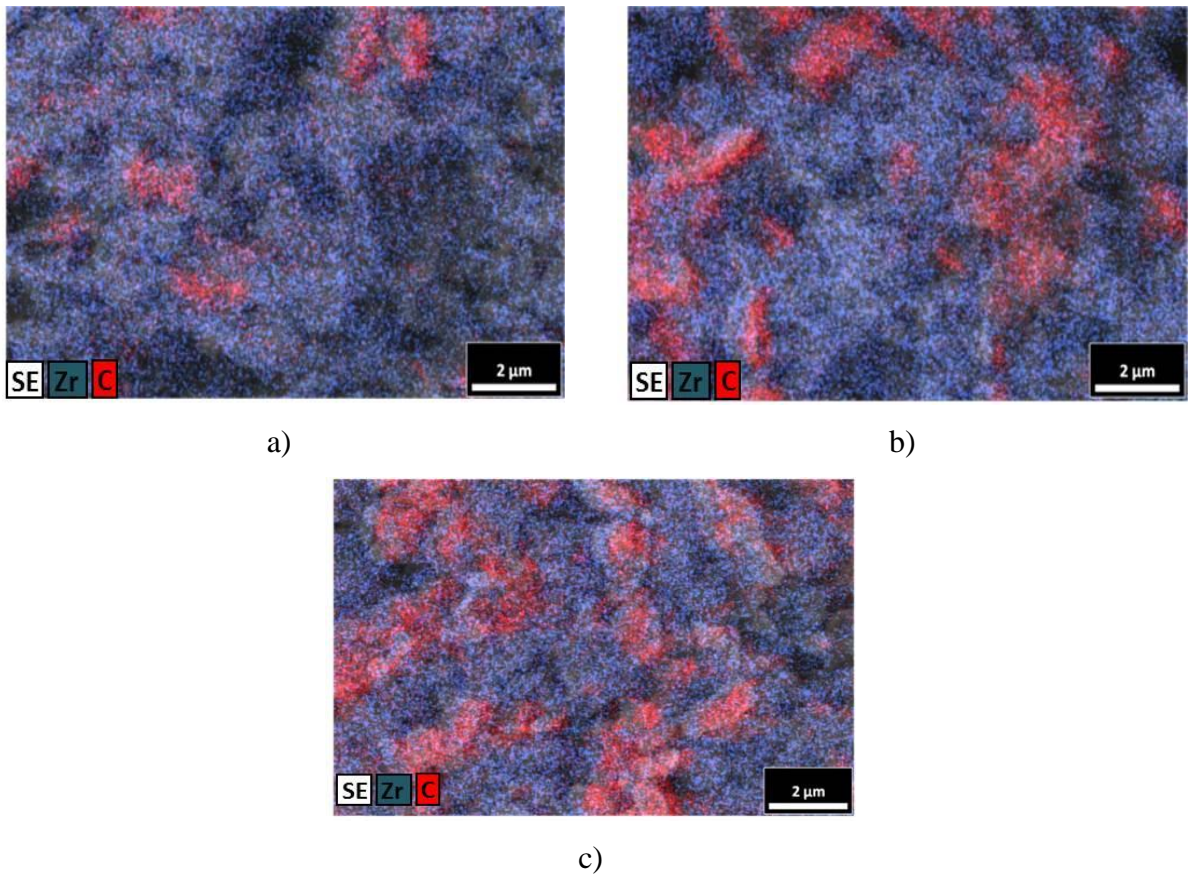


Fig. 4.5. Elemental mapping showing MWCNT dispersion into 8YSZ. a) ZR-1, b) ZR-5 and c) ZR-10. (Zr -blue, C – red).

4.1.3 Phase analysis of 8YSZ / MWCNTs milled powders

Phase analyses of 8YSZ reference and 8YSZ / MWCNT composites after milling were performed (Fig. 4.6). All milled composites indicate the presence of cubic zirconia (JCP2:00-049-1642) as a main phase and monoclinic zirconia (JCP2:00-037-1484) as minor phase. Cubic zirconia phase is approved by the main lines appearing at 2Θ of 30.24° , 34.88° , 50.17° and 59.69° . While, the monoclinic phase is observed at 2Θ of 28.36° and 31.12° .

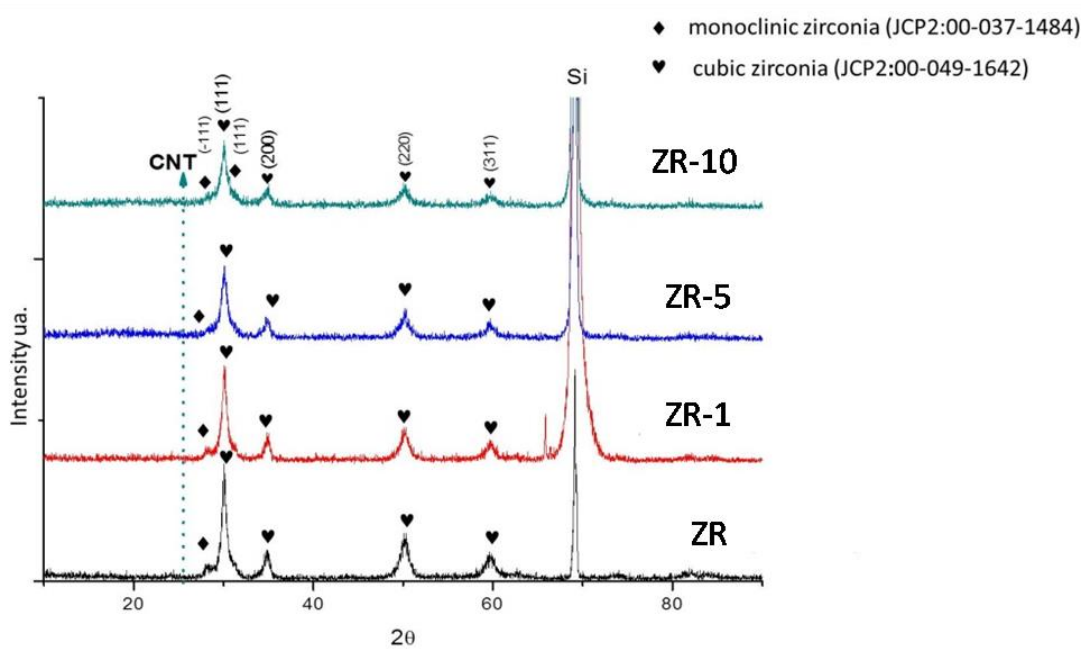


Fig. 4.6. XRD patterns of 8YSZ reference and 8YSZ /MWCNT powders after milling.

To confirm the structural integrity of MWCNT after milling Raman spectroscopy measurements were conducted upon 8YSZ /MWCNT powders as shown in Fig. 4.7. Four Raman spectra are shown in the $150 - 3500 \text{ cm}^{-1}$ wavenumber region, which were measured on powder mixtures with different MWCNT content (0, 1, 5 and 10 wt%). Typical yttria stabilized zirconia fingerprint bands were scattered at 189 cm^{-1} , 268 cm^{-1} , 341 cm^{-1} , 380 cm^{-1} , 483 cm^{-1} , 633 cm^{-1} in ZR composite powder as illustrated by the black line. These data were consistent with several literature works as mentioned elsewhere [157, 158]. Characteristic Raman peaks of 8YSZ are less intensive or completely absent in the wavenumber region from 100 to 700 cm^{-1} in case of ZR-1, ZR-5, ZR-10 powder composites. Raman absorption signals associated with multi-wall carbon nanotubes are observed at 1590 cm^{-1} (G band) and 1355 cm^{-1} (D band) [161]. The intensity of

these bands are used to indicate the CNT quality and purity. In fact, the G band is associated with the stretching in-plane vibration of the sp^2 C-C bonds and carbon crystallinity. While, D band is assigned to the structural defects in carbon systems and activated by the presence of out plane vibrations. This band is also visible in case of amorphous carbon.

Raman spectra also show a wide band at higher wavenumbers, the so called 2D band, which appears at 2687 cm^{-1} , 2684 cm^{-1} and 2690 cm^{-1} in case of 1, 5 and 10 wt % MCWNT content, respectively. The 2D band features originate in a two-phonon, second-order Raman scattering process in carbon nanotubes [162].

The intensity ratio of D and G band (I_D/I_G) has been widely used to investigate the structural purity, structural defects or MWCNTs disordering namely the presence of vacancies, grain boundaries, agglomerations or other types of defects[161, 162]. In principle, the larger the number of defects, the higher the D band intensity. Peak positions and intensity of distinct scattering bands were determined by Lorentzian fitting of Raman spectra. Although such procedure has some uncertainty because of the number of free parameters, it can provide additional structural information about the 8YSZ / MWCNTs powders.

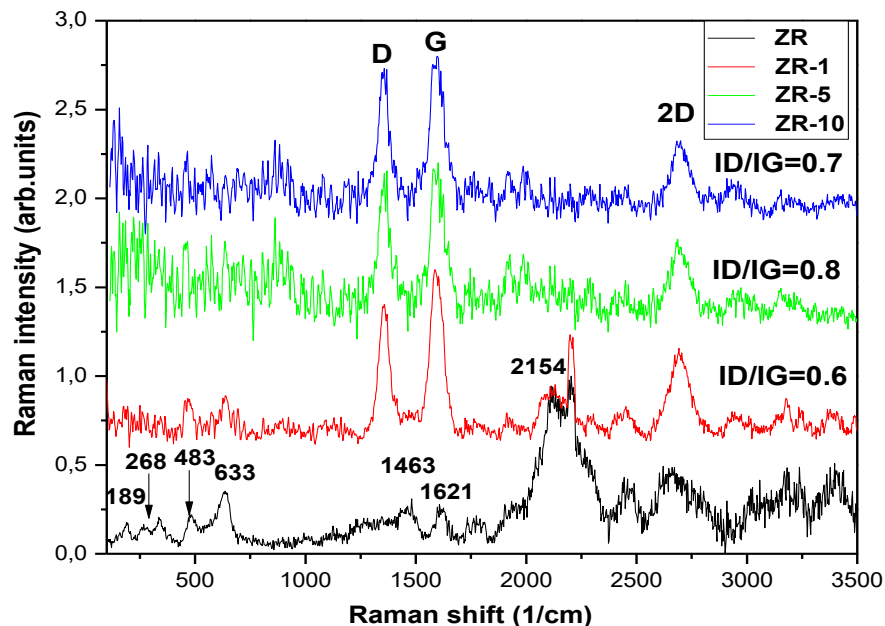


Fig. 4.7. Raman spectra using a laser excitation wavelength at 488 nm conducted upon the 8YSZ (ZR) and 8YSZ / MWCNTs powders (ZR-1, ZR-5, ZR-10).

According to the current results, the I_D/I_G ratio reached its highest value (0.8) with ZR-5 followed by (0.7) in ZR-10 composites and (0.6) in ZR-1. The results suggest that although MWCNTs exhibits defects, their structure is preserved since I_D/I_G is <2 in all the composites. This has been approved from the previous HRTEM images on the milled composite showing non-destructive milling on MWCNTs structure and increase of MWCNTs agglomeration with respect to their content.

4.2 Structural properties of the milled and sintered 8YSZ / MWCNTs composites

4.2.1. Density and microstructure of the sintered 8YSZ / MWCNTs composites

The apparent and bulk density measurements of the sintered composites are illustrated in Fig. 4.8. The highest apparent density was achieved in ZR-1 (6.76 g/cm^3) followed by 6.02 g/cm^3 found in ZR reference composite. However, the apparent density dropped to lower values with increasing MWCNTs content. Inversely the bulk density showed a slight rise in the case of ZR-5 and ZR-10 composites compared to their apparent density from 4.97 g/cm^3 to 5.44 g/cm^3 and from 4.36 g/cm^3 to 5.02 g/cm^3 , respectively. However, the bulk density of ZR-1 decreased to 5.80 g/cm^3 and standalone ZR composite maintained practically the same relative density. The increase in bulk density at high amount of MWCNTs could be attributed to the additional pores volume between and inside the particles taken into consideration during its evaluation. A detailed graph considering the apparent porosity of the composites is illustrated in Fig. 4.8c. The apparent porosity revealed close results between (ZR / ZR-1) composites on one hand and between (ZR-5/ ZR-10) composites on the other hand. Therefore, the four composites can be divided into two categories.

The first category is the so-called close pore composites referring to ZR and ZR-1 composites and having minimal/maximal porosity of ($\sim 33 \%$, $\sim 16.5 \%$) respectively. While, the second category is considered as composites with open pores (ZR-5 and ZR-10) with minimal/maximal porosity of ($\sim 41.6 \%$, $\sim 50 \%$) respectively.

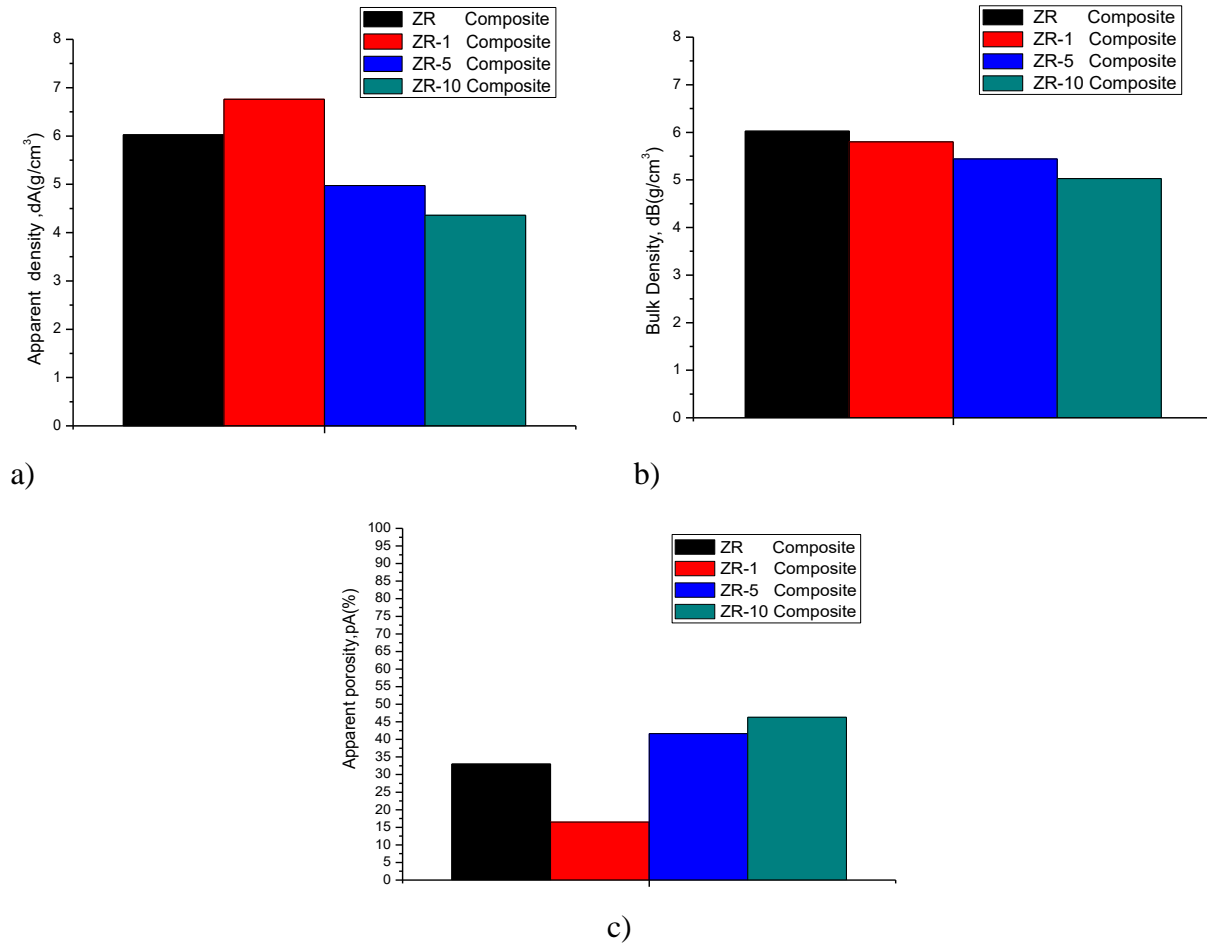


Fig. 4.8. Summarized density of ZR, ZR-1, ZR-5 and ZR-10 composites. a) Apparent density, b) Bulk density, c) Apparent porosity.

Morphological investigations performed on the polished cross sections surface for both category of samples with closed and open pore are depicted in Fig. 4.9. The detailed surface morphology in the inset image revealed at first sight a smooth, homogeneous and tenacious surface for standalone ZR (Fig. 4.9a). The surface area of ZR-1 composite (Fig. 4.9b) was mainly predominated by nanometric areas reflecting a good MWCNTs distribution in 8YSZ matrix and a high interfacial bonding resulting in a microstructure refinement.

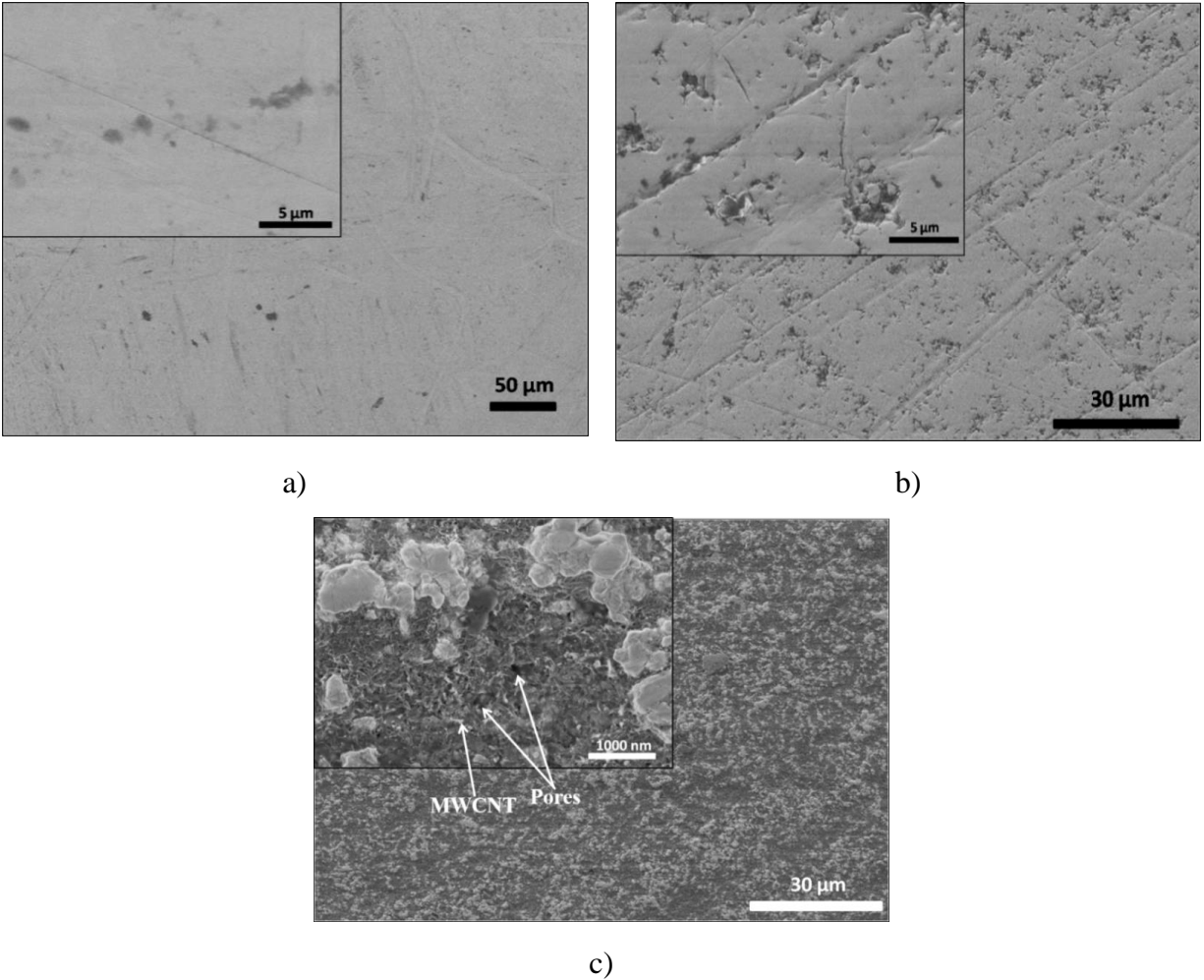


Fig. 4.9. SEM micrographs showing the morphological differences between composites. a) ZR, b) ZR-1 and c) ZR-10.

By contrast, it is most remarkable that the surface morphology of ZR-10 (Fig. 4.9c) exhibits a reduced interfacial bonding between 8YSZ and MWCNTs, a deep superficial porosity and high agglomeration of MWCNTs. These effects, led to the formation of a rough surface and discontinuous 8YSZ particles embedded in a dark phase composed by MWCNT agglomerations.

4.2.2. Phase analyses of 8YSZ / MWCNTs sintered composites

XRD analysis was performed on the sintered samples to determine the phase composition. XRD patterns (Fig. 4.10) revealed the presence of cubic and tetragonal zirconia phases in all the composites including reference and the monoclinic phase only in the composites with MWCNTs. The strongest peak can be identified as the peak of both cubic (PDF89_9069) and tetragonal (PDF80_2155) phase appearing at 2Θ of 30.119° and 30.270° , respectively. The following two intense peaks refer to the tetragonal phase at 2Θ of 50.424° and 59.816° . Other peaks of cubic phase with minor intensity were seen at 2Θ of 34.918° , 62.617° and 81.669° . The 8YSZ monoclinic (PDF65_1023) phase was perceived mainly at high amounts of MWCNTs (ZR-5 and ZR-10) with peak at 2Θ of 28.06° and 31.3° .

Tab. 4.1. Structural phases and crystal size parameters calculated with Standard less quantitative analysis method for ZR, ZR-1, ZR-5 and ZR-10 composites prepared by SPS at 1400°C .

Sample	Cubic phase. (%)	Crystal Size (nm)	Tetragonal phase. (%)	Cryst. size (nm)	Monoclinic Phase. (%)	Cryst. size (nm)
ZR	24.8	50.4	75.2	43.4	0	0
ZR-1	34.6	41.8	63.1	41.9	2.4	37.1
ZR-5	28.4	41.7	67.3	36.4	4.3	24.6
ZR-10	37.4	48.7	58.4	53.2	4.2	27.4

At the powder form, the cubic phase was recorded as a main phase composing ZR, ZR-1, ZR-5 and ZR-10. The phase analysis investigations revealed the appearance of new phases namely tetragonal and monoclinic resulting from sintering process by SPS at 1400°C . In the case of ZR composite, a huge percentage of phase transition from cubic to tetragonal was found, about 24.8 % cubic via 75.2 % tetragonal. The proportion of cubic phase was higher, while the amount of tetragonal phase decreased in ZR-1, ZR-5 and ZR-10 compared to 8YSZ ceramic. Hence, the proportional increase of monoclinic phase with MWCNTs content, is originated from tetragonal phase transition during cooling stage. The high t→m phase transformation promotes the risk of flaw and material cracking due to volume expansion[18].

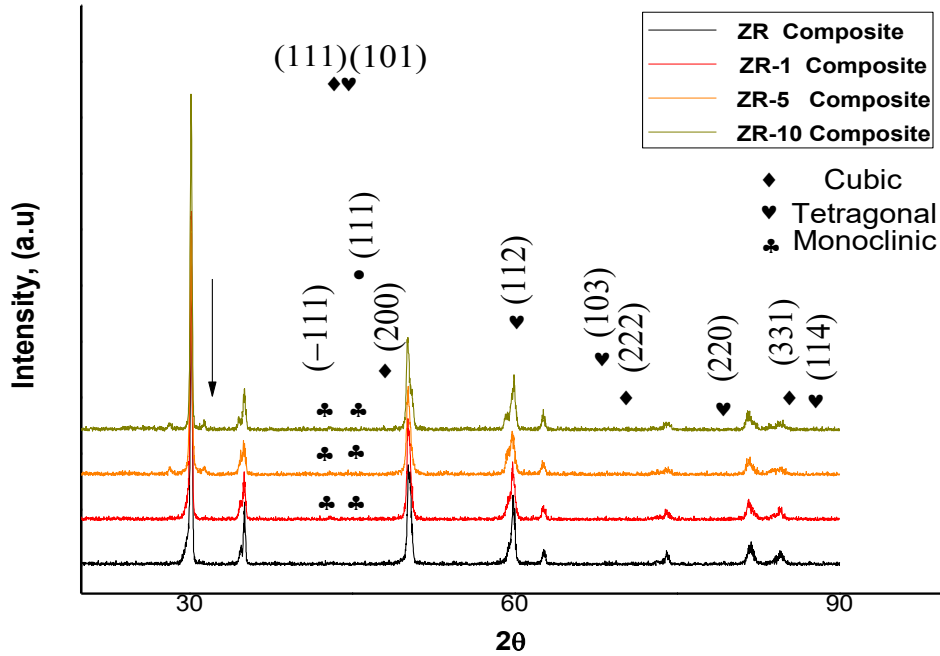


Fig. 4.10. XRD pattern for ZR, ZR-1, ZR-5 and ZR-10 composites.

4.2.3. Stability of MWCNTs in 8YSZ sintered composites

Raman spectroscopy measurements were conducted on the sintered 8YSZ / MWCNTs composites as well as ZR composite for several reasons. First, to show up the new spectral features in ZR composite that confirm the growth of tetragonal phase as displayed by XRD after SPS, and to further discern whether SPS process has affected MWCNT structure and integrity with respect to its concentration. The Raman spectrum of ZR sintered composites displayed in (Fig. 4.11). (black line) exhibits a sharp and narrowed bands with shifted position compared to milled powders (Fig. 4.7). Typical bands appear at 260, 318, 461, 625 and 641 cm^{-1} . Further, the peak positions at 260, 318, 461 and 641 cm^{-1} are found to be the main characteristic bands of tetragonal ZrO_2 as reported in [165]. On the other hand, the bands at 625 cm^{-1} and 641 cm^{-1} largely overlap and shows highly intense configuration with quite broad shape. These peaks belongs to cubic and tetragonal zirconia phases respectively [165,166]. Hence, we conclude that the Raman spectrum of ZR are in quite accordance with XRD experiments confirming the presence of tetragonal and cubic phases. However, XRD analysis remains the most accurate in term of phase distinction especially when

dealing with polymorphic zirconia phases. Since not all the phases can be identified with Raman but easily achieved by XRD as has been claimed elsewhere [159].

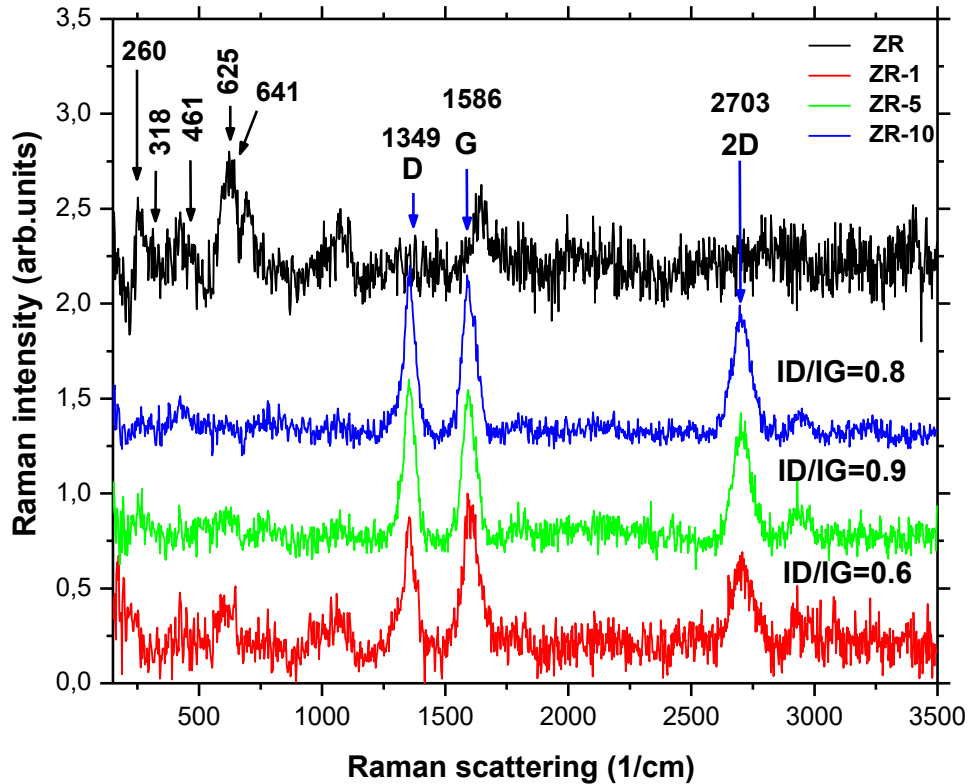


Fig. 4.11. Raman spectra of the sintered composites confirming the structural integrity of MWCNTs into 8YSZ matrix and quantitative evaluation of MWCNT damages during sintering process based on ID/IG ratio calculation.

Typical Raman spectrum bands are arising from multi-wall carbon nanotubes in ZR-1, ZR-5 and ZR-10 composites as indicated in Fig. 4.11. The G band is observed around 1586 cm^{-1} while D band at 1349 cm^{-1} . G and D bands are assigned to crystal quality and MWCNTs disordering due to the presence of vacancies, grain boundaries, agglomerations or other types of defects respectively (see chapter 4.1.3). Further, the 2D band originate in a two-phonon, second-order Raman scattering process appears at 2703 cm^{-1} . The intensity ratio of D and G band (ID/IG) increased by 0.1 after SPS process in ZR-5 (0.9) and ZR-10 (0.8) while ID/IG remain constant at 0.6 in case of ZR-1. This increase is most likely related to CNT damage or structural defect during

SPS process which is highly influenced by the temperatures and pressures applied during the SPS or by residual thermal stresses of the matrix that appears during the cooling stage[167].

4.2.4 Conclusion

In this chapter, different characterization techniques such as SEM, TEM, EDS, XRD and Raman spectroscopy were used to examine the effect of high energy milling, microstructural features and phase transformation of 8YSZ composites containing 1 – 10 wt% of MWCNTs at powder as well as sintered state. The majority of the as received pure 8YSZ grains exhibited an irregular particle shape with significant sharpness at the edges and a coarse microstructure with mixed particles size ranged from bigger size with an average of $33.48 \pm 7.45 \mu\text{m}$ to smaller ones with an average of $16.22 \pm 3.5 \mu\text{m}$. The powder morphology of pure 8YSZ has been significantly modified after wet milling to a refined and homogeneous microstructure sized of approximately 400 nm with soft grain edges that tends to form low-angle grain boundaries due to repeated welding, which was the aim of the milling. Further grain refinement has been well recognized to increase proportionally with MWCNT content. In case of ZR-1 powders, the MWCNT fibers were dispersed uniformly along the contact edges of 8YSZ grains, while the high MWCNT content (5 and 10 wt%) results in the formation of small zirconia grains of ($< 100 \text{ nm}$) and particles ($> 200 \text{ nm}$) embedded into MWCNTs agglomerations and networks. Additionally, it is worth noting that minor MWCNT spherical agglomerations with diameters of about $1.42 \pm 0.41 \mu\text{m}$ has been observed in the sample with 1 wt% compared to 5 wt% and 10 wt% where the agglomerations increased to approximately $1.87 \pm 0.39 \mu\text{m}$ and $2.5 \pm 0.2 \mu\text{m}$, respectively. The structural integrity and non-destructive milling of MWCNT has been proved by both Raman spectroscopy and HRTEM images respectively. Density measurements and microstructural investigation conducted upon the cross section surfaces of the well-polished and sintered composites, indicated an extensive structural dissimilarity which draw a clear picture of MWCNTs indirect effect on 8YSZ matrix. In fact, density and porosity measurements showed a moderate improvement from 6.02 g/cm^3 to 6.76 g/cm^3 , and remarkable reduction from 33 % to 16.5 % respectively in favor of ZR-1 composite compared to the monolithic composite (ZR). Whereas, up to 5 wt% MWCNTs the density dropped to lower values and therefore the porosity followed inversely proportional trend. In addition, ZR-1 composite has a smooth and homogeneous surface predominated by nanometric

dark spots which reflects a good MWCNTs distribution and a high interfacial bonding. Inversely, the interfacial bonding has been severely reduced at higher amounts due to the inevitable agglomerations of MWCNTs. Monolithic sintered composite revealed the formation of new phase (tetragonal) with high quantity (about 75.2 %) with only a small fraction of cubic phase round 24.8 %. This fact illustrates a clear influence of sintering process by SPS at high temperature of 1400 °C to enhance the growth of tetragonal phase as compared with composites at powder state in which the dominant phase was mainly cubic. Indeed, the tetragonal phase has been retained to room temperature, thereby can influence the improvement of the comprehensive mechanical properties of monolithic composite based on transformation toughening zirconia mechanism. However, ZR-5 and ZR-10 composites showed an increase in the monoclinic phase. In fact, during the cooling phase transformation from t→m occurs associated with a large volume expansion which promotes the risk of brittle failure.

4.3. Mechanical properties of the sintered 8YSZ / MWCNTs composites

4.3.1. Crack propagation modes and toughening mechanisms in the sintered 8YSZ/MWCNTs composites

Ceramic based conductive nanosized material resist differently to a compressive and uniform stress as reported by the literature. The number of studies are currently available on zirconia reinforced with MWCNTs, SWCNTs, double-walled carbon nanotubes (DWCNTs) or graphene. *Michálek.et.al* studied the mechanical properties of composites incorporated with 1 vol% of MWCNTs into alumina, and alumina/zirconia matrices [168].

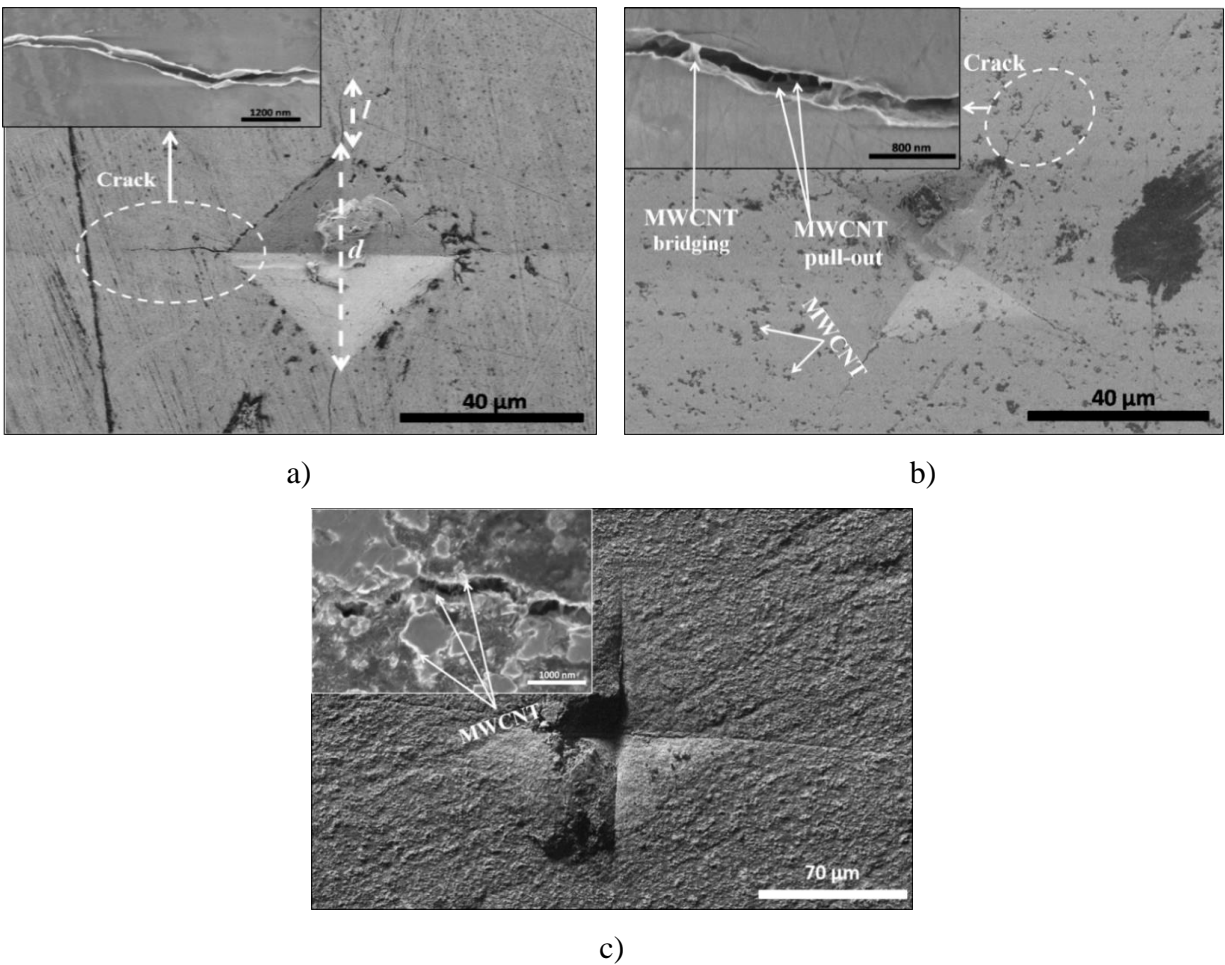


Fig. 4.12. Crack patterns and indentation produced by Vickers hardness.

a) ZR, b) ZR-1 and c) ZR-10.

They found an increase of about 8 % and 35 % in fracture toughness for both composites, respectively, compared to the monolithic alumina [168]. *Shin. et. al* fabricated yttria stabilized zirconia (YSZ) ceramics reinforced with reduced graphene oxide (RGO) by spark plasma sintering (SPS) [169]. The composite hardness decreased with RGO addition, while the fracture toughness underwent an increase from 4.4 to 5.9 MPa^{1/2}[169]. *Kasperski et al.* studied the mechanical properties of YSZ /DWCNTs composites sintered by (SPS) with carbon contents up to 6.3 wt%. In that study the highest mechanical properties ($\sigma_f=694$ MPa, $K_{Ic}=7$ MPam^{1/2}) were obtained for the composite with low 1.2 wt.% carbon contents. (σ_f) and (K_{Ic}) refers to the fracture strength and the single-edged notched beam fracture toughness respectively. However, the fracture toughness was inferior to that of standalone 8YSZ ceramic [170]. The behaviour of zirconia matrix under a certain applied compressive load changed with the addition of MWCNTs. In fact, the matrix dissipates the applied stress to MWCNTs. This mechanism played an important role in improving the fracture toughness of the composites. MWCNT pulling-out, crack bridging, crack deflection and branching are among the typical phenomena resulting from toughening zirconia with MWCNTs. The properties of MWCNTs are considered as crucial factors that control the efficiency of stress transferred from the matrix to the fiber.

The indentation and the crack propagation in the different categories of the samples namely closed pore (8YSZ, ZR-1) and open pore (ZR-5, ZR-10) sintered at 1400 °C, have been carefully examined (Fig. 4.12). MWCNTs pulling-out and bridged region are visible in ZR-1 composite (Fig. 4.12b). Two interesting observations were noticed during the crack propagation analysis between the standalone matrix and the reinforced matrix with 1 wt% MWCNTs. Generally, the average crack path length calculated from the indentation center was more or less higher than that of the unreinforced matrix about ~ 50 μm via ~ 46 μm . This could be attributed to the residual porosity induced by the MWCNTs (Fig. 4.12b). Further, the crack widths were narrowed to an average ~ 76 μm compared to that of the standalone matrix ~ 120 μm . Indeed, the observed bridged regions in the reinforced composite form an obstacle that protect the crack from reaching a critical state and consequently prone to failure. Thus, the crack path appears more restrained and tapered. On the other hand, the pull-out of MWCNTs occurs when the transferred stress exceeds the interfacial shear stress, the latter depend largely on the number of MWCNT walls, their thickness, elastic modulus, and volume fraction [171].

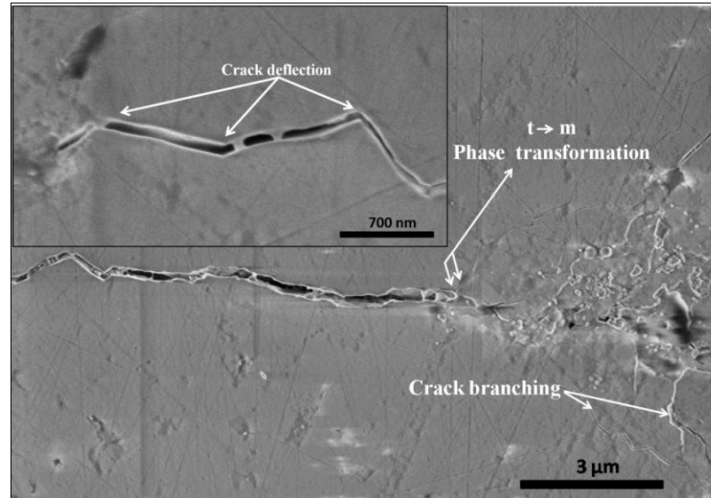


Fig. 4.13. SEM micrograph showing crack deflection, crack branching and the possibility of phase transformation occurrence (tetragonal to monoclinic) in ZR-1 composite.

Conversely, an inconsistent matrix was observed regarding open pore composites (ZR-5, ZR-10). The incoherence in 8YSZ matrix containing 10 wt% MWCNTs composite delineated in (Fig. 4.12c) was attributed to discontinuity of zirconia particles and deep open porosity on surface. Moreover, the inset SEM micrograph in Fig. 4.12c draw clearly the aggregation of MWCNTs that degrades the resistance and lower the fracture toughness resistance. Similar results have been reported in numerous studies [158,167,172]. Indeed, the dispersion of the stress occurs throughout the pores starting from the center of the indentation and ending after a long unrestrained path. Hence, theses composites (ZR-5, ZR-10) exhibited low mechanical properties.

The contribution of crack deflection and crack branching in the toughening mechanism and restoring the matrix of ZR-1 composite was shown in Fig. 4.13. The crack deflection takes place when the crack tends to follow the grain boundaries and therefore reflects the composite microstructure [173]. Furthermore, the possibility of phase transformation occurrence from metastable tetragonal zirconia to monoclinic was highly believed in ZR-1 composite. Effectively, the existence of microcracks along the crack path axes as marked in Fig. 4.13 provides the evidence of lattice volumetric expansion. In Addition, the difference of thermal expansion coefficient (CTE) mismatches between zirconia matrix ($10.3 \times 10^{-6} \text{ }^\circ\text{C}^{-1}$) and MWCNT ($1.6\text{-}2.6 \times 10^{-5} \text{ }^\circ\text{C}^{-1}$) must be taken into account during the estimation of the overall structural phenomenon involved in improving the toughness of ceramic composites. Thermal expansion coefficient depends on several properties of the composite constituent. For instance, micro structural phases, the

distribution and the volume fraction of MWCNTs into ceramic matrix, and finally the interaction features between the grains and the fibers especially at large volume fractions [174]. Therefore, thermal residual stress is often provoked during the cooling state of the composites at room temperature as a result of (CTE) differences [175].

4.3.2 Vickers hardness and indentation fracture toughness measurements of the sintered 8YSZ / MWCNTs composites

Vickers hardness results of 8YSZ / MWCNTs composites sintered at 1400 °C in function of surface displacement are illustrated in Fig. 4.14. The variation of Vickers hardness with surface displacement was practically homogenous and reached high values ~13.49 GPa in ZR composite and ~12.44 GPa in ZR-1.

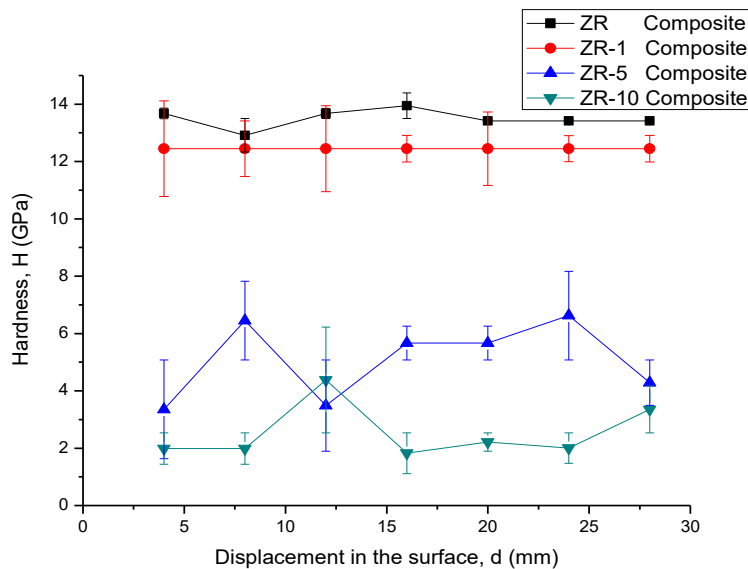


Fig. 4.14. Variation of Vickers hardness with surface displacement for ZR, ZR-1, ZR-5 and ZR-10 composites.

The average hardness for ZR-5 and ZR-10 composites decreased sharply to low values ~5 GPa and ~ 2.7 GPa successively. Fluctuations reflecting the non-homogeneity of Vickers hardness were highly indicated in ZR-5 and ZR-10 curves. The experimental hardness measurements confirmed the previous microstructural investigation shown in Fig. 4.9, Fig. 4.12. and Fig. 4.13.

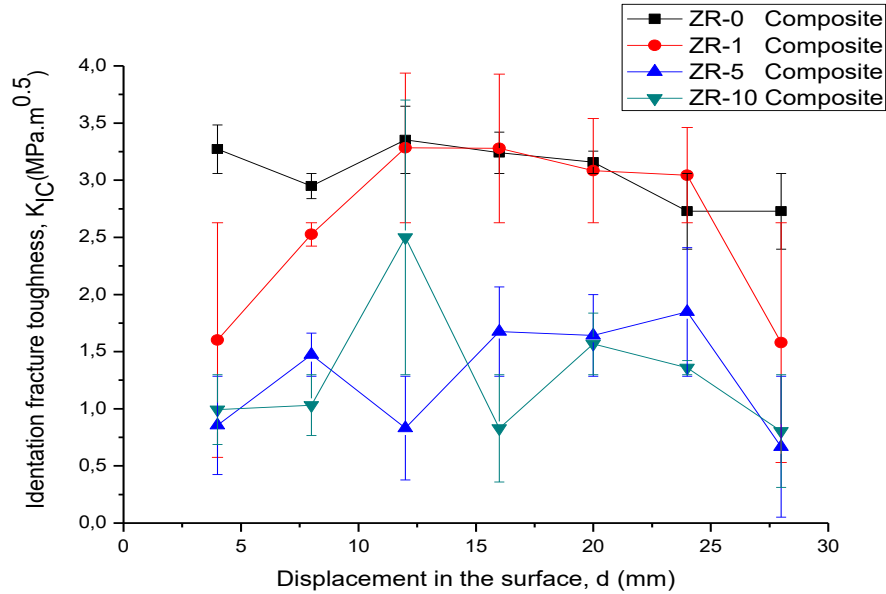


Fig. 4.15. Variation of indentation fracture toughness with surface displacement for ZR, ZR-1, ZR-5 and ZR-10 composites.

The indentation fracture toughness at different positions of 8YSZ / MWCNTs composites were comparable with reference ZR composite (Fig. 4.15). The fracture toughness variation line of ZR-1 had initially an upward trend followed by a flat band region where the two variations lines of ZR-1 and ZR were almost overlapping each other at an average $\sim 3.2 \text{ MPa.m}^{0.5}$. In some positions, we noticed that ZR-1 line slightly exceeds of ZR ($3.2 \text{ MPa.m}^{0.5}$ via $2.6 \text{ MPa.m}^{0.5}$) before it dropped back again to its initial value. On the other hand, the fracture toughness decreased rapidly to low values $\sim 1.5 \text{ MPa.m}^{0.5}$ and $\sim 1.3 \text{ MPa.m}^{0.5}$ when MWCNTs content has been increased to 5 wt% and 10 wt% respectively. The improvement of the fracture toughness in some positions of ZR-1 composites is originated from the previously discussed toughening mechanisms (MWCNT pulling-out, crack bridging, crack deflection, crack branching and phase transformation) confirmed by SEM investigation assessed upon the composite surface before and after the indentation.

4.3.3 Microstructure and fractographic test of the sintered 8YSZ / MWCNTs composites

Morphological investigation was used to quantify the microstructural properties of 8YSZ composites with different amounts of MWCNTs (0 - 10 wt%) after fractographic test (Fig. 4.16). Structural observations of the well milled and sintered standalone zirconia (ZR, Fig. 4.16a) revealed a coarse microstructure with significantly high grain size of approximately $6.11 \pm 4.08 \mu\text{m}$. Subsequently, as presented in Tab. 5.1 grain growth of the zirconia was drastically reduced to $0.96 \pm 0.49 \mu\text{m}$ with the addition of 1 wt% MWCNTs. The later, induced a pinning effect on zirconia grain boundaries where the grains appear mostly plate shaped and sharp at edges (Fig. 4.16b). Hence, the well pinned MWCNTs led the formation of an additive force against fracture propagation along the grain boundaries. As consequence, high amount of fracture energy is required to propagate into the next neighbour grain, displaying transgranular fracture mode as a dominant mechanism. In this mode the fracture occurs through the grains and propagates from one to another. This behaviour is reinforced by the minimal apparent porosity (16.50 %) and the considerable flexural strength obtained in this composite (ZR-1).

By contrast, obvious microstructural transformation induced by increasing MWCNTs content is observed in ZR-5 (Fig. 4.16c) and ZR-10 (Fig. 4.16d). Furthermore, the microstructural modification was illustrated mainly by severe grain refinement $0.54 \pm 0.04 \mu\text{m}$ in ZR-5 and $0.28 \pm 0.01 \mu\text{m}$ in ZR-10, simultaneously with the observation of a considerable increase in the residual porosity to 41.64 % via ZR-5 and to 46.28 % via ZR-10 resulting from inevitable agglomeration of higher amount of MWCNTs in matrix. Indeed, despite the high sintering temperature of 1400°C used during the composites consolidation process, the higher amount of MWCNTs inhibited grain growth and favored intergranular fracture mode occurrence especially for ZR-5 and ZR-10 composites. The arrows of dashed line marked in Fig. 4.16c and Fig. 4.16d show a significant random dispersion of MWCNTs along the grain boundaries within the fine and granular microstructure, suggesting relatively weak surface bonding and easier fracture propagation along the weakest areas (grain boundaries) rather than through the grains, therefore intergranular fracture mode is more remarkable in ZR-5 and ZR-10 composites.

On the other hand, various possible directions of MWCNTs besides the perpendicular direction to sintering pressure is claimed to be possible with an optimum amount added to the

matrix. More importantly, diverse directions of MWCNTs are among the principal key factors responsible of toughening mechanisms in 8YSZ / MWCNTs composites (like crack deflection, bridging and branching) as have been reported in the literature [176]. Furthermore, *Declan et al.* have numerically modelled the influence of second phase features inclusion into ceramics matrix on toughening mechanism using the finite volume (FV) method [177]. The dominance of crack deflection was observed when the modulus of the second phase was increasing resulting in considerable strength enhancement.

The mechanical properties with some additional structural data of all the sintered composites are summarized in Tab. 4.2. The 3-point bending test was carried out at room temperature for all the specimens. The flexural strength shows an increase in favor of ZR-1 compared to the monolithic material (ZR) from 464 MPa to 502 MPa. Meanwhile, ZR-5 and ZR-10 express typical brittle fracture confirmed by critical decline of the flexural strength to 263 MPa and 166 MPa, respectively, which is very consistent with the previously structural investigations. The measured apparent density ρ follows similar behaviour as the flexural strength varying between a maximum and a minimum of 6.75/4.36 g/cm³, respectively. The calculated hardness values shown in (HV, Tab. 4.2) are the average of seven indents measured on the specimen's diagonal with 4 mm displacement. Higher hardness values were achieved in both ZR composite equal to 13.49 ± 0.23 GPa and ZR-1 composite of about 12.44 ± 0.97 GPa compared to similar composition and testing conditions [60, 117]. However, in case of ZR-5 and ZR-10 the average hardness dropped to low values, confirming the influence of high MWCNTs content on the overall strength of ceramic composites [153, 154]. The average indentation fracture toughness (K_{Ic}) obtained along the specimen's surfaces with different MWCNTs content using indentation crack length size are also presented in Tab. 4.2. The calculated indentation fracture toughness K_{Ic} of standalone composite ZR was slightly higher (3.06 ± 0.22 MPa·m^{1/2}) than for ZR-1 (2.63 ± 0.62 MPa·m^{1/2}). It is worth noting that, the latter manifested a fluctuated tendency along the tested surface diagonal, where in some positions a slight improvement was obtained [178]. Hence, this can be mainly attributed to good dispersion of MWCNTs along the grain boundaries after high sintering temperature (1400 °C). In our case, the K_{Ic} decreased further by increase of MWCNTs addition, the ZR-5 and ZR-10 presented 1.28 ± 0.42 MPa·m^{1/2} or 1.30 ± 0.44 MPa·m^{1/2} (Tab. 4.2).

In the same context, *Melk et al.* studied 3Y-TZP composites with 0–2 wt% MWCNTs content with grain size in the range of 177-148 nm, then compared their fracture toughness obtained via single edge V-notch beam (SEVNB) and via indentation size induced by Vickers indenter [155]. As a results, the fracture toughness obtained via indentation increased with MWCNTs content and show relatively higher values in the range of 3.57– 4.97 MPa·m^{1/2}, while the true fracture toughness measured using SEVNB varied independently of the composition, and manifested lower values about 2.8 MPa·m^{1/2}. In a relatively similar finding, *Mazaheri et al.* reported higher fracture toughness using indentation method compared to single edge V-notch beam (SEVNB) technique [60]. However, to the best of my knowledge both methods led to obtain the highest fracture toughness value of 10.9 ± 0.42MPa·m^{1/2} cited in the literature when increasing MWCNTs content to 5 wt%. The controversial results of toughness data reported by several authors under similar composition and processing methods draw clearly the importance to make compromises between accuracy, time consumption and the complexity of the experimental procedure with regard to microstructural features of the composites such as grain size and effective crack lengths while choosing the fracture toughness testing method as discussed in detail elsewhere [179–181]. Therefore, the reliability and suitability of the empirical relationships and different testing techniques must be carefully taken into consideration during the interpretation of the final results devoted to tribological investigation.

Tab. 4.2: Mechanical properties of sintered 8YSZ / MWCNTs composites with some structural data.

Sample notation	MWCNTs content (wt%)	Apparent porosity (%)	Density ρ , (g/cm ³)	Average hardness Hv, (GPa)	Bending strength, (MPa)	Average (IFT, K _{Ic}) (MPa·m ^{1/2})	Grain size (μ m)
ZR	0	32.99	6.02	13.49 ± 0.23	464	3.06 ± 0.22	6.11 ± 4.08
ZR-1	1	16.50	6.75	12.44 ± 0.97	502	2.63 ± 0.62	0.96 ± 0.49
ZR-5	5	41.64	4.97	5.07 ± 1.17	263	1.28 ± 0.42	0.54 ± 0.04
ZR-10	10	46.28	4.36	2.53 ± 0.76	166	1.30 ± 0.44	0.28 ± 0.01

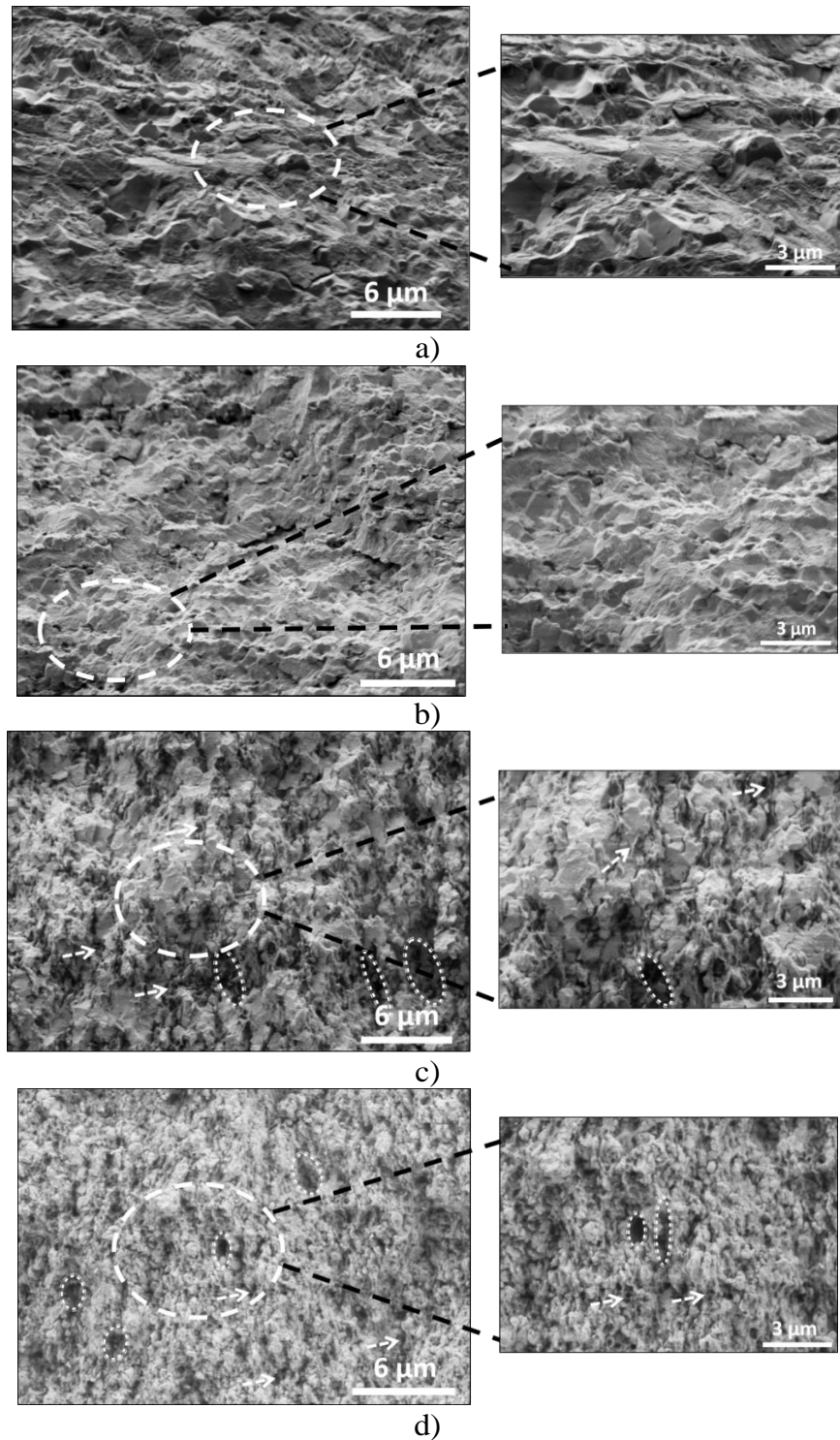


Fig. 4.16. Fracture surfaces of ZR, ZR-1, ZR-5 and ZR-10 composites correspond to a), b), c) and d) respectively at different magnifications. In (c) & (d) the circles of dashed line mark micro-structural defects generated by agglomerations and porosity in the grain boundaries, the arrows show MWCNTs fibers emplacement and dispersion in the microstructure.

4.3.4 Conclusion

This chapter aimed at first to exhibit a comparative evaluation of the Vickers hardness and indentation fracture toughness between 8YSZ / MWCNTs and standalone 8YSZ composite. Further, fractographic analysis has been performed on the composites fractured surfaces after the 3-point bending test to record the fracture modes with respect to the materials microstructure. It was found that the variation of Vickers hardness with surface displacement were practically homogenous and reached high values ~ 13.49 GPa for ZR and ~ 12.44 GPa for ZR-1 composites. The distribution of indentation fracture toughness of ZR-1 was mostly equal or higher than that of ZR in other point positions. In fact, the analysis of the crack propagation modes confirmed the presence of MWCNT pull-out, crack bridging and crack deflections besides more restrained and tapered crack path in the ZR-1 composite compared to ZR. These characteristics are considered as toughening mechanisms and played a vital role to restore the matrix and increase the composite resistance to crack propagation. In case of ZR-5 and ZR-10, both Vickers hardness and indentation fracture toughness have undergone significant degradation and fluctuated distribution. This was mainly associated with incoherent and discontinuous matrix due to the deep open pores on the surface and a long unrestrained crack path. Structural observations based on fractographic test revealed a coarse microstructure with an average grain size of about 6.11 ± 4.08 μm for monolithic 8YSZ. The later decreased to an optimum value of 0.96 ± 0.49 μm in case of ZR-1. In these composites, the dominated fracture mode is transgranular indicating high bonding energy between the grains and additional toughening mechanism due to a uniform dispersion of MWCNTs along the grains. As a result, a slight increase of bending strength from 464 MPa to 502 MPa has been found in favor of ZR-1 over ZR. Meantime, ZR-5 and ZR-10 exhibited further grain refinement to 0.54 ± 0.04 μm and 0.28 ± 0.01 μm respectively, along with random MWCNTs dispersion favoring intergranular fracture mode occurrence and critical decline of the flexural strength to 263 MPa and 166 MPa respectively.

4.4 Wear mechanism of sintered MWCNTs reinforced zirconia composites under dry sliding conditions

4.4.1. Average friction coefficient and wear rate

The average friction coefficient (μ) corresponding to the sliding distance in the range of 0–40 m and 40–400 m of the sintered composites tested under $V1= 0.036$ m/s, $V2= 0.11$ m/s sliding speeds, using ball on disc method and Si_3N_4 balls counterpart are presented in Fig. 4.17. Generally, the steady state friction coefficient (μ_{AFS}) is attained from ~ 40 m of sliding distance in all the composites. Its average values are presented in Fig. 4.17. At low sliding speed ($V1= 0.036$ m/s) μ_{AFS} is seen to be significantly high ~ 0.76 and quit similar to all the tested composites regardless their specific micro-structural properties or MWCNTs content. However, the tribotest carried out at $V2= 0.11$ m/s sliding speed revealed the existence of proportional relationship between (μ_{AFS}) and the mechanical properties evolution as well as the grain size.

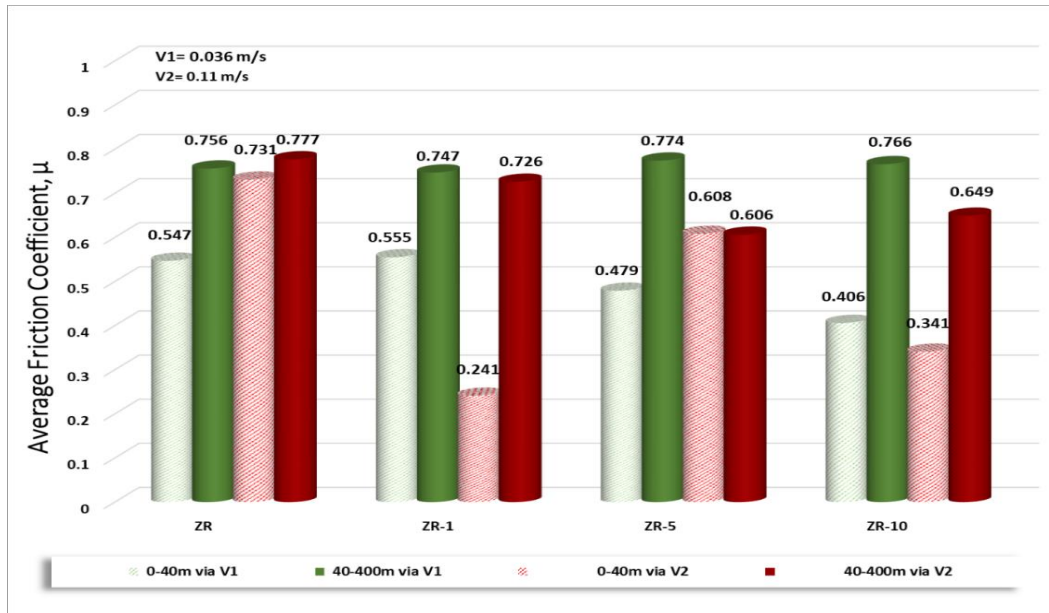


Fig. 4.17. Comparative graph presenting the average friction coefficient (μ) during transitory state (0-40m) and steady state (40-400m) for all the composites tested at fix normal load (5N) and different sliding rates ($V1=0.036$ m/s, $V2=0.11$ m/s).

In fact, this relationship is manifested by decrease in μ_{AFS} regarding the more brittle composites possessing lower grain size as well as mechanical properties (0.608 via ZR-5 and 0.649 via ZR-10). Whereas, ZR and ZR-1 composites owing higher grain size and particular mechanical properties characterized majorly by transgranular fracture mode, the μ_{AFS} recorded at high sliding speed V2 (0.777 via ZR and 0.726 via ZR-1) were found to be quite high and similar to the ones obtained at lower sliding speed. The wear rate results performed on the surface of 8YSZ / MWCNTs composites at both sliding speeds are illustrated with the red and black curves as presented in Fig. 4.18. According to this measurement, ZR composite exhibits an obvious severe wear behaviour confirmed by its highest wear rate of about $5.55 \times 10^{-3} \text{ mm}^3/\text{m}$ recorded at V1 sliding speed. A contrasting trend is marked in ZR-1 composite, where a fascinating improvement of the wear rate was established at low speed $\sim 4.73 \times 10^{-6} \text{ mm}^3/\text{m}$ exceeding all the other composites. This tendency is attributed in fact to its highest flexural strength and apparent density ($\rho = 6.75 \text{ g/cm}^3$).

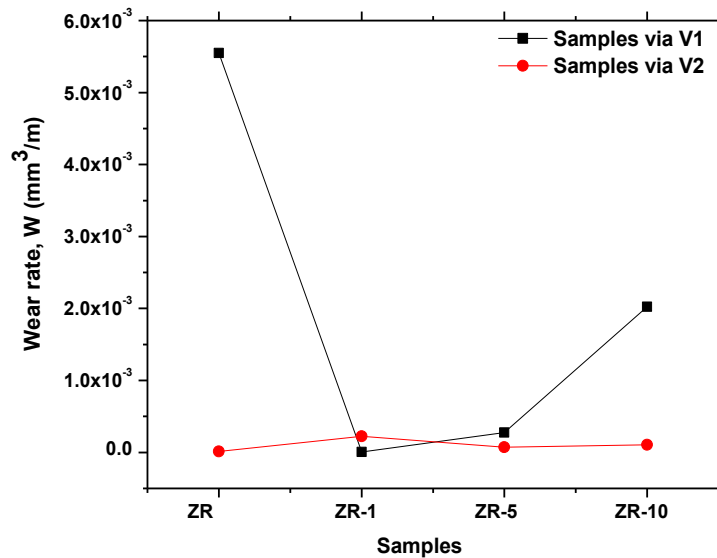


Fig. 4.18. Wear rate (W) of the investigated composites via $V1=0.036 \text{ m/s}$ and $V2=0.11 \text{ m/s}$ sliding speed.

Furthermore, at the same speed quantitatively significant low wear rate is also well recognized with the addition of 5 wt% MWCNTs. This value is seen to increase slightly in ZR-10 composite but remains still lower compared to the severe wear observed in ZR. Applying high velocity ($V2=0.11 \text{ m/s}$) resulted in a better wear resistance. In fact, the wear

rate results were closely similar or occasionally high in all the composites, therefore the influence of structural properties was not recognized as MWCNTs content increased. A particularly similar decreasing tendency of the wear rate and steady state friction coefficient (μ_{AFS}) in ZR-5 and ZR-10 composites as the speed increase was observed (Fig. 4.17 and Fig. 4.18). This is obviously linked to the previous microstructural evolution due to MWCNTs content increase as reported previously. According to the current study I deduce that grain size, density, mechanical properties or even sliding speed play a major role to beneficially or adversely affect the tribological performance of the structural ceramic composites. Indeed, these parameters vary dependently to MWCNTs content in the matrix, where high content led to a huge grain refinement and an obvious lubricant effect at the contacts areas between ball/surface. Thus, decreasing the friction coefficient. In fact, I conclude, that MWCNTs plays an indirect factor influencing the overall tribological behaviour of the composites. In addition, another important factor which mostly reflects a direct insight into friction behaviour consists in the evaluation of the average arithmetic surface roughness (Ra) of the composites inside the wear track after tribotest at both sliding speed.

In similar context, *Nieto et al.* reported an inversely proportional relationship (at high GNP content) between the applied load and surface roughness [182]. The latter is supposed to increase with the friction. However, in their work the effect of surface roughness on friction behavior was not evaluated with respect to sliding speed variation. Quite similar approach is developed in the current study but at increased sliding speed instead of applied load variation[183]. The corresponding results shown in Tab. 4.3 reveal a remarkable decrease of Ra from 1.5 to 0.2 μm in ZR-5 and from 0.7 to 0.2 μm in ZR-10 inside the wear track passing from V1 sliding speed to V2. Therefore, applying high sliding velocity can be considered as another key factor also inversely proportional to the roughness in 8YSZ / MWCNTs composites extensively at high MWCNTs content (5 wt% and 10 wt%). On the other hand, the measured roughness inside the wear track of ZR decreased only by 0.1 μm at low sliding speed V1 from its initial value after polishing process (0.6 μm). Additionally, slightly higher roughness decrease was also noticed in ZR-1 from 0.6 μm to 0.3 μm , which match well with the proportional high friction tendency obtained in these two composites (ZR, ZR-1) at the speed of V1.

By contrast, the fine roughness values found in ZR-5 and ZR-10 tested at V2 were systematically increased inside the wear track at lower speed V1. In effect, the high surface fluctuation induced by MWCNTs agglomeration and could not be suppressed at low sliding speed V1 is supposed to arise another factor responsible of roughness increase. The measured values of the roughness are in good agreement with the low friction response (Fig. 4.17).

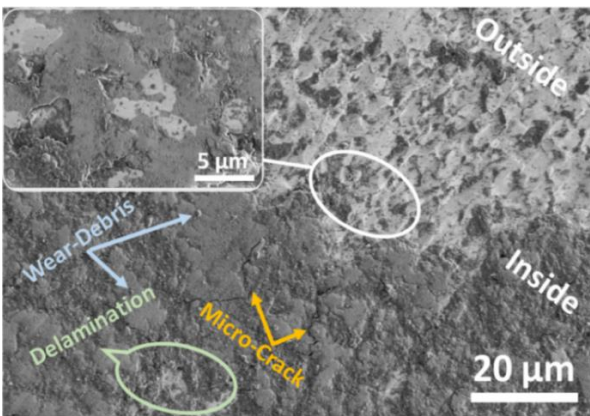
Tab. 4.3. Average roughness measured inside and outside the wear track at V1 and V2 sliding speed.

Sample notation	Roughness outside the track <i>Ra</i> , (μm)	Roughness inside the track via V1 <i>Ra</i> , (μm)	Roughness inside the track via V2 <i>Ra</i> , (μm)
ZR	0.6	0.5	0.3
ZR-1	0.6	0.3	0.4
ZR-5	0.6	1.5	0.2
ZR-10	0.6	0.7	0.2

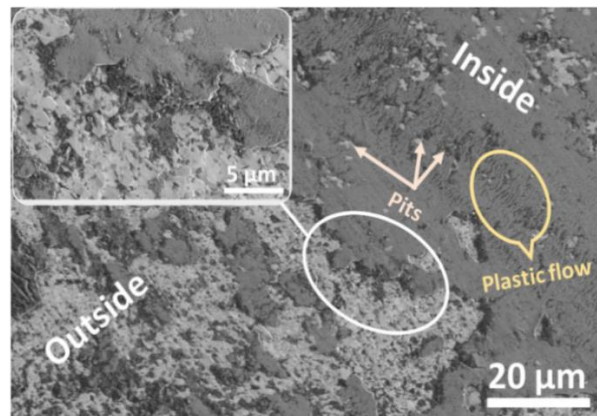
4.4.2 Wear (W) damage mechanism

The wear mechanism and the induced damage remained after tribo test carried out at V1 and V2 speed were assessed using SEM measurements as presented in Fig. 4.19. According to the previous results (Fig. 4.17 and Fig. 4.18), ZR composite manifested high steady state friction coefficient (μ_{AFS}) as well as high wear rate at low sliding speed V1. This behavior is effectively shown to be very coherent with the morphological features inside the wear track profile shown in SEM micrograph (Fig. 4.19a). Indeed, the morphological study illustrates clearly the formation of a fractured ultrathin tribofilm which appears highly incomplete and abrasively damaged during the tribotest. Furthermore, zirconia grain pull-outs, delaminated areas, micro cracks and highly wear debris content are observed on the wear track profile and supposed to act as a main possible wear mechanism in the monolithic material. In fact, the wear debris resulting from tribofilm fracturing is assumed to react as a third body abrasive particle between the rubbing surfaces, leading to a significant rise in the friction and wear rate. Moreover, the high wear rate obtained in ZR at V1 sliding speed can be assigned to its large grain size ($6.11 \pm 4.08 \mu\text{m}$) with a plate shape and to the dry sliding condition, therefore affording high friction behavior. The difference in the mechanical properties of phase composition is

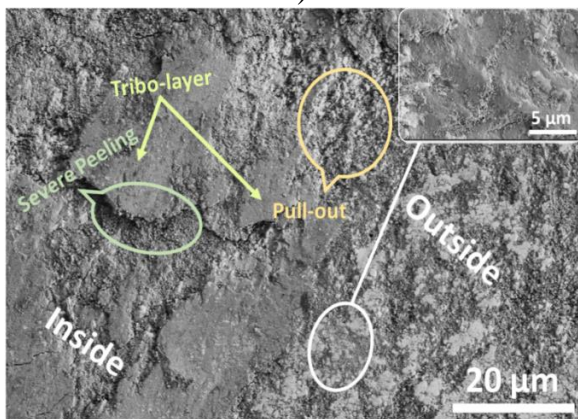
highly believed to act as another key factor, which can entail stress concentrators and creates abrasive grooves on the worn area as depicted in SEM micrographs of ZR composite tested at high sliding speed V2 (Fig. 4.19e). In the case of ZR-1, a perfectly continuous and uniform tribofilm was formed during the test at both sliding speeds (V1 as well as V2) (Fig. 4.19b, Fig. 4.19f). Further, it can be clearly seen that neither severe film fragmentations nor wear debris or micro cracks are observed within the wear track, but only minor plastic flows and light pits. Indeed, the high wear performance manifested in ZR-1 corresponds principally to MWCNTs-induced toughening mechanism and the creation of a protective thin tribofilm.



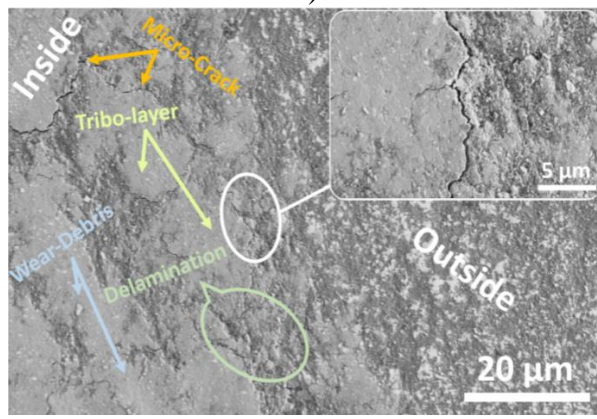
a)



b)



c)



d)

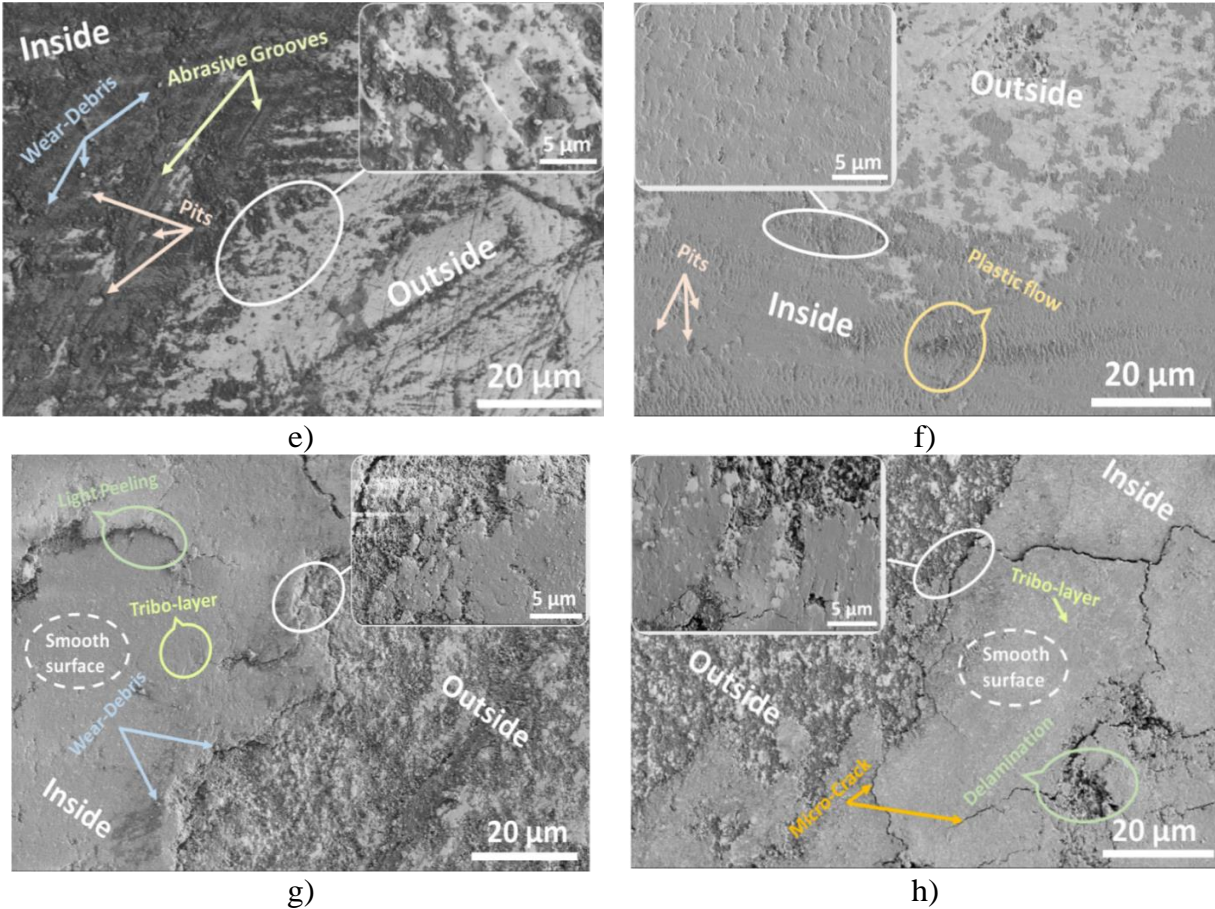


Fig. 4.19: Comparative SEM micrographs inside and outside the wear track profile of composites showing wear mechanism features and tribofilm formation during the test via $V1=0.036$ m/s correspond to a) ZR, b) ZR-1, c) ZR-5 and d) ZR-10, and via $V2=0.11$ m/s correspond to e) ZR, f), ZR-1 g) ZR-5 and h) ZR-10, respectively.

MWCNTs-induced toughening mechanism influenced the wear performance of our material by dissipating energy through deformation, crack bridging, crack branching and crack deflection. These mechanisms restrain cracking on both the track surface and sub-surface. The existence of these toughening mechanisms were confirmed and well explained in chapter 4.4.1. [178]. Similar observations have been obtained by *Li et al.* during the wear test of ZrO_2 -GNP composites [184]. On the other hand, the granular structure of ZR-5 tested at $V1$ sliding speed inhibited the formation of continuous tribofilm (Fig. 4.19c) where only ticks (islands) are observed besides severe peeling that cause surface removal on the track. This specific behaviour is attributed to the increased agglomeration of MWCNTs and the superficial porosity which could not be suppressed under the

applied load and low speed. *Zhang et al.* have reported similar observations with graphene nanoplatelet (GNP)-reinforced alumina (Al_2O_3) composites [185]. However, in the current study MWCNTs pull-out were also noticed in some areas of the wear track (Fig. 4.19c), which is acting as an intrinsic lubricant suggesting the reported improvement in the wear rate. In case of ZR-10, the formed tribolayer appears coherent character. However, some delaminated areas, wear debris and micro cracks were also observed masking the obtained slight wear rate increase in this composite compared to ZR-5.

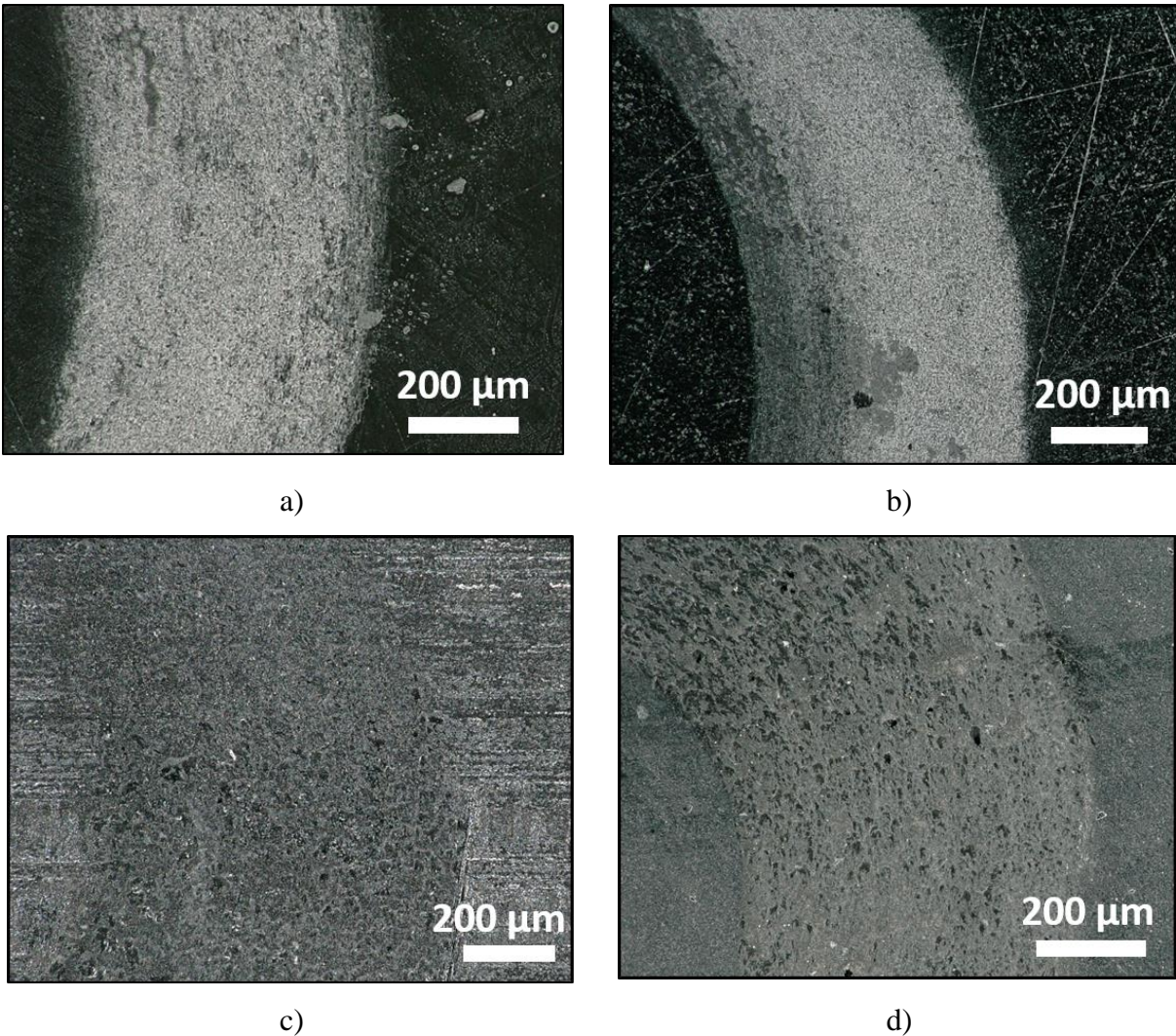


Fig. 4.20. Digital microscope micrographs illustrating the wear track profile after tribotest at $V_1=0.036$ m/s sliding speed. a) ZR, b) ZR-1, c) ZR-5 and d) ZR-10 composites.

The combined effect of applied load and high speed V2 were beneficial to enable the formation of dense, smooth and continuous lubricant areas on the worn surface of ZR-5 and ZR-10 composites (Fig. 4.19g and Fig. 4.19h). Additionally, under load of 5 N the small and rounded particles with a size of about 0.54 and 0.28 μm , respectively were expected to coalesce easily in the asperity valleys, which systematically diminish the superficial porosity and thereby permit the typical established improvement in friction and wear. I investigated the wear tracks at both sliding speeds V1 and V2 using digital microscope.

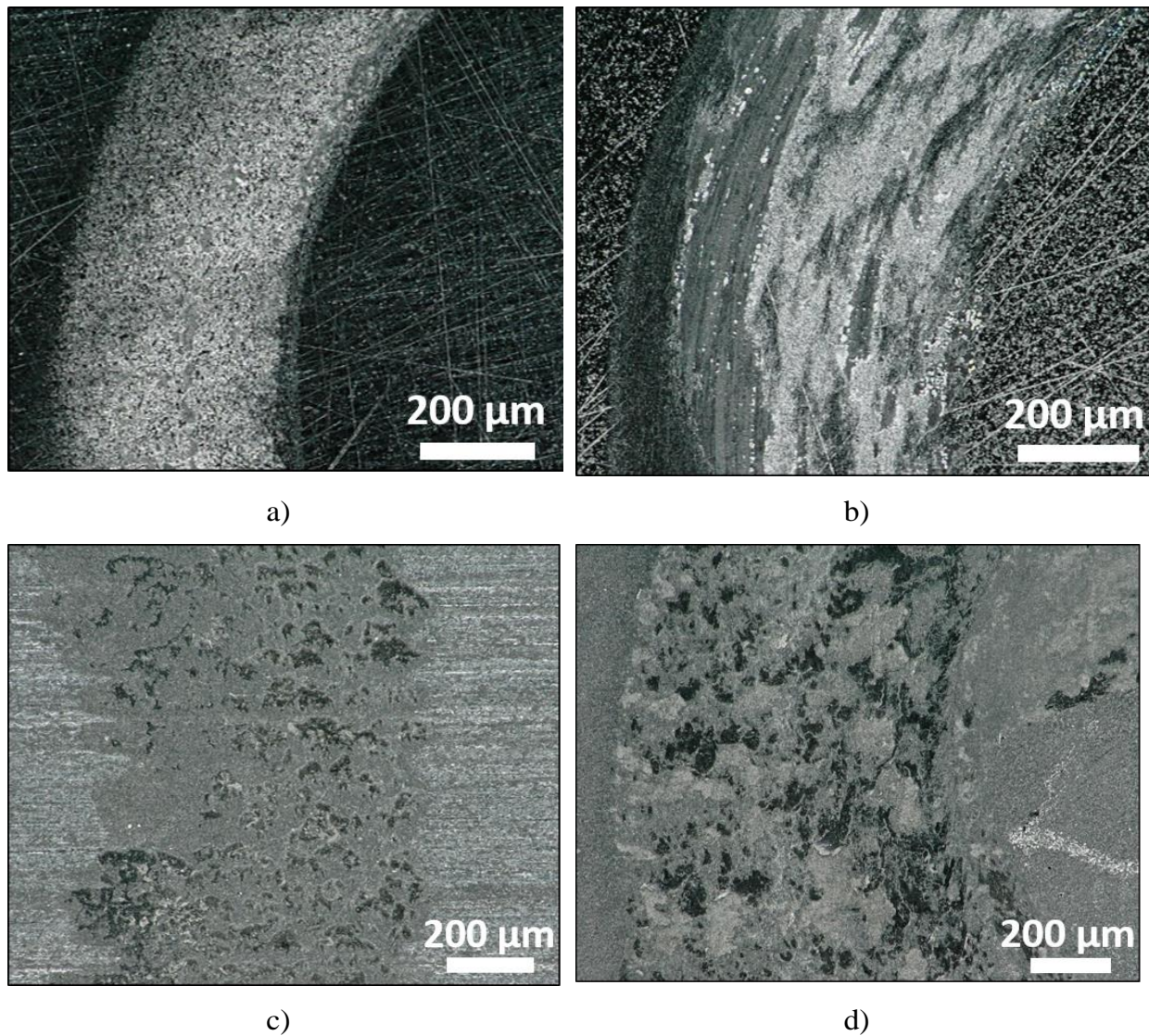


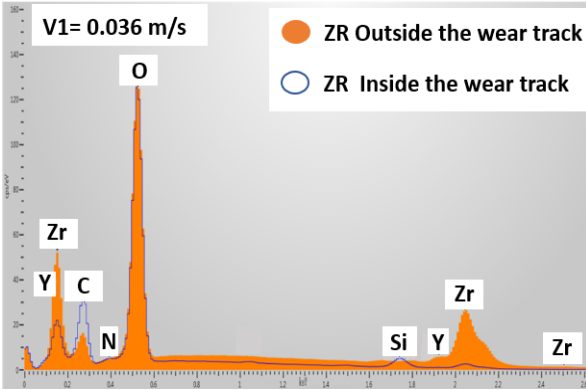
Fig. 4.21. Digital microscope micrographs illustrating the wear track profile after tribotest at $V_2=0.11$ m/s sliding speed. a) ZR, b) ZR-1, c) ZR-5 and d) ZR-10 composites.

From the observations, it is shown an obvious increase in the width of the wear track simultaneously with MWCNT content. The abrasive wear mechanism and amount of wear debris manifested in ZR composite at low sliding speed is confirmed by Fig. 4.20a.

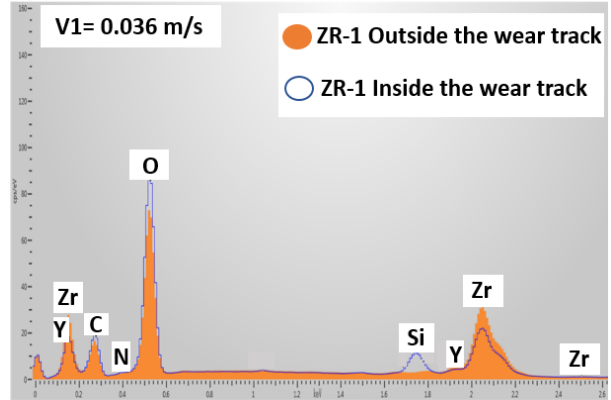
4.4.3 Elemental composition of wear track in 8YSZ / MWCNT composites

In order to identify the microstructural evolution and correlated with the observed wear mechanisms mainly from chemical point of view, EDS analysis was employed inside the worn and unworn surfaces of 8YSZ and 8YSZ / MWCNTs composites (Fig. 4.22). The analysis of EDS spectra conducted mainly to the following results: Zr peak is observed to decrease significantly during the friction test performed at low speed in ZR composite while, the intensity of O peak remained practically identical. In fact, the high hardness and large grain size enable the matrix to support more the contact load during surface rubbing (ball/composite). This led in turn to high abrasion of the matrix. As consequence, the latter undergoes severe pull out followed by scattering along the worn and unworn track profile to form wear debris as seen in the previously (chapter 4.6.2) corresponding with structural observations. As a result, the intensity of Zr peak decreased sharply (Fig. 4.22a) accompanied with high wear and friction response. Contrasting elemental composition tendency is recognized at high speed for ZR composite (Fig. 4.22e). Thus, it's highly believed that de-bonding between O and Zr atoms occurred in the monolithic material tested at high speed, manifested by high increase in O peak and slight decrease in Zr peak inside the wear track, accompanied with appearance of Si peak. The decreased Zr peak intensity is attributed to the possibility of zirconium atoms scattered outside the track, while the O atoms resulted from de-bonding remained inside the track to cluster with Si transferred from the counterpart and therefore enhance the formation of thick SiO₂ layer that which improve the wear performance. In ZR-1 composite the presence of Si peak after tribotest is confirmed by EDS spectra (Fig. 4.22b) despite the low sliding speed. Eventually, in this case neither the zirconia matrix nor MWCNTs have experienced severe abrasive wear, this is well validated by the observation of minor decrease of Zr which systematically induced as light increase of O peak due to zirconia de-bonding mechanism. From structural view of carbon, non-remarkable damage is expected to occur after friction test as confirmed by the unreduced intensity of C peak. As consequence, the formed tribo-layer at V1 consists mainly of Si particles and minor fraction of O. These results are in good agreement with structural investigation showing the formation of a perfectly continuous and

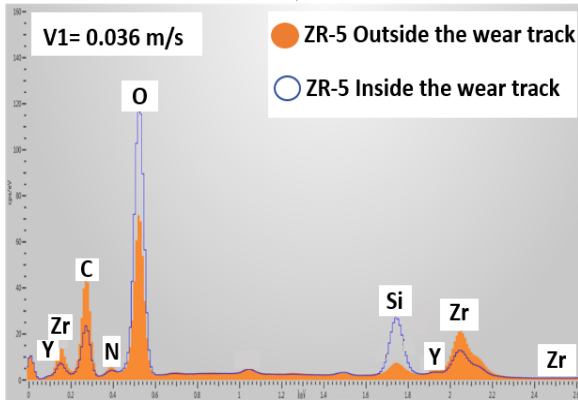
uniform tribofilm without any remarkable surface damage. Similar tendency is approved with increasing speed, however Si and O peaks become more intense and therefore Zr peak lowered due to the supposed de-bonding mechanism.



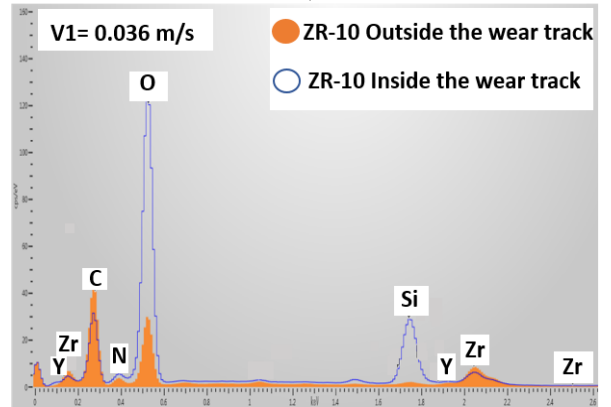
a)



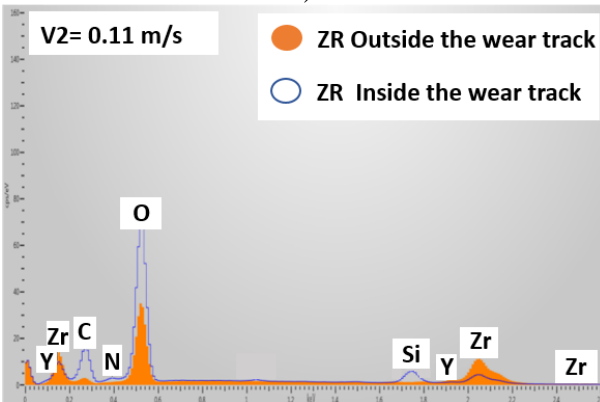
b)



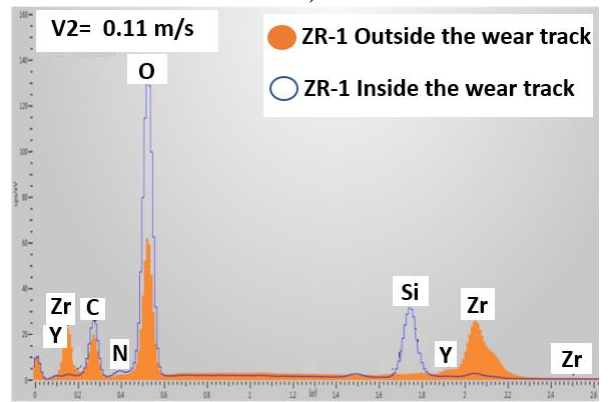
c)



d)



e)



f)

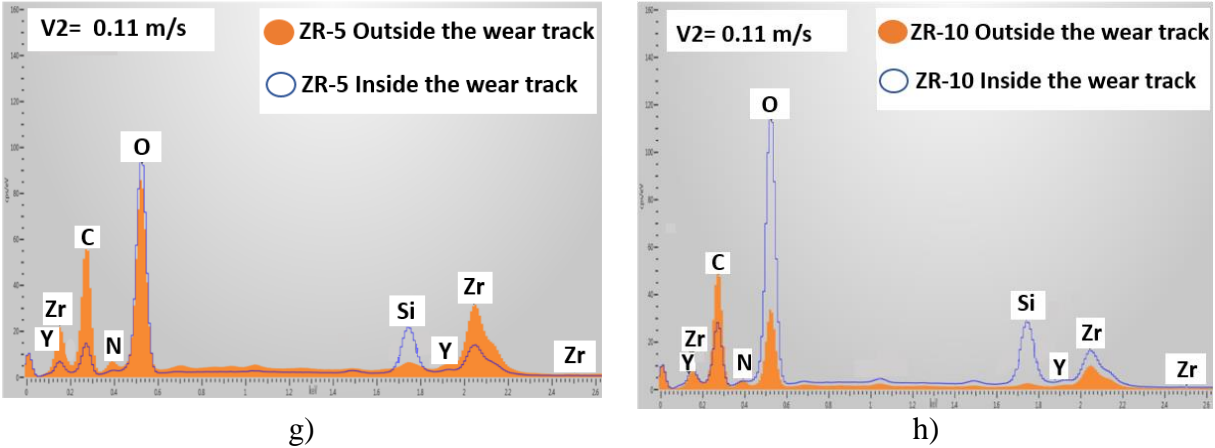


Fig. 4.22. Energy dispersive X-ray spectroscopy (EDS) inside and outside the wear track profile of composites. a) ZR, b) ZR-1, c) ZR-5, d) ZR-10 composites tested via $V1=0.036$ m/s and correspond to e) ZR, f) ZR-1, g) ZR-5 and h) ZR-10 via $V2=0.11$ m/s, respectively.

EDS analysis shows highly dissimilar behaviour between the group composed by (ZR, ZR-1) and (ZR-5, ZR-10). Indeed, the intensities of Si and O peaks are recorded to increase simultaneously with MWCNTs content till attending its highest values in ZR-10 at $V1$ (approximately of three times inside the track). Furthermore, Si peaks corresponding to the group of (ZR, ZR-1) were intensified essentially by the increase of sliding speed. More importantly, the main difference clearly displayed in the spectra of ZR-5 and ZR-10 compared to ZR and ZR-1 consists in a sharp decrease of C peak intensity obtained inside the worn surface. This is supposed to be linked with MWCNTs exfoliation, giving rise to appreciable lubricant effect. In fact, from the spectra displayed in (Fig. 4.22g) it's well noted that ZR-5 composites manifested the largest decrease of C peak after tribotest justifying the improved friction response at high sliding speed. On the other hand, besides the observed lubricant effect due to MWCNTs exfoliation, the friction decrease in ZR-10 at high sliding speed is thought to be the result of the high Si particles transfer from the counterpart to the surface and its adherence to O resulted from the easier 8YSZ matrix de-bonding under friction test. In addition, despite the high increase of O peak intensity and contrary to monolithic material, Zr peak is increased slightly suggesting less scattering of zirconium to form wear debris but were instead induced into the so-formed SiO_2 layer giving rise to compacted and dense areas in the tribolayer of ZR-10.

4.4.4 Conclusion

This chapter discussed the results from tribological investigation of the 8YSZ / MWCNTs composites performed using ball on disk method, Si_3N_4 balls as a counterpart, total sliding distance of 400, dry sliding conditions, low ($V_1= 0.036$ m/s) and high ($V_2= 0.11$ m/s) sliding speed. At the speed of $V_1= 0.036$ m/s, ZR-1 exhibited 99.9 % improvement in the wear rate followed by 95 % in ZR-5 and 64% in ZR-10 composite compared to pure 8YSZ. Furthermore, the observation of grain pull-outs, micro cracks and high amount wear debris in pure 8YSZ give the evidence of abrasives wear behaviour as main wear mechanism. This is shown to be linked with its coarse microstructure and the dry sliding condition. The outstanding wear improvement marked in ZR-1 is in good agreement with the formation of continuous and uniform tribofilm on the worn surface. However, in ZR-10 the tribofilm is discontinuous and does not protect from the brittle fracture due to the structural defects such as agglomeration and porosity. At the speed of $V_2= 0.11$ m/s, minimal wear rate values have been recorded in all the composites regardless MWCNTs content. According to the roughness measurements, high sliding velocity was systematically inversely proportional to the roughness in 8YSZ / MWCNTs composites at high MWCNTs content namely 5 wt% and 10 wt%. This was in line with the reduced friction at V_2 in ZR-5 and ZR-10 composites tested under V_2 , reflecting easier sliding between the rubbing surfaces. In fact, this friction improvement is shown to be linked with the appearance of intrinsic solid lubricant effect due to MWCNTs exfoliation (carbon peak decrease) and high Si incorporation as confirmed by EDS spectrum. Further, the combined effect of applied load and high speed V_2 were beneficial to enable the formation of dense, smooth and continuous lubricant areas on the worn surface of ZR-5 and ZR-10 composites.

5. GENERAL CONCLUSION

Multiwall carbon nanotube (MWCNT) reinforced zirconia (ZrO_2) composites are attracting growing interest thanks to their ability of self-healing of the crack, the possibility to tailor the desired nanostructured properties and their outstanding wear behavior.

The aim of my PhD work is the experimental synthesis of 8 mol% yttria-stabilized zirconia (8YSZ) containing 1, 5 and 10 wt% MWCNTs. I also have aimed to explore how the microstructure affect their mechanical and tribological properties. Thus, affording the possibility to extend their wide use in technical applications with excellent efficiency.

The first part of my work was devoted to the investigations of the effect of the milling process performed at rotational speed of 4000 rpm and conducted for 5 h on the control of the grain size and morphology of MWCNT dispersion, homogeneity with respect to its concentration at powder state. I accomplished the initial characterization of the microstructure in 8YSZ / MWCNTs powder including MWCNTs agglomeration and MWCNTs fiber structural features. I found that the powder morphology of pure 8YSZ has been significantly modified after milling to a refined and homogeneous microstructure sized of approximately 400 nm with soft grain edges, which tends to form low-angle grain boundaries due to repeated welding. Further 8YSZ grain refinement and MWCNT bundles have been recorded to increase proportionally with MWCNT content, while the later showed practically nondestructive structural milling. The addition of 1 wt% MWCNTs led to uniform dispersion of MWCNT fibers along the contact edges of 8YSZ grains.

In the second part of my PhD work, the microstructural features namely density, porosity, grain growth and phases of the sintered 8YSZ / MWCNT composites by spark plasma sintering (SPS) process at 1400 °C have been subjected to a detailed investigation and connected with the results from Vickers hardness and indentation fracture toughness measurements. In fact, 8YSZ / 1 wt% MWCNTs sintered composite owns the highest density 6.76 g/cm³ and bending strength of 502 MPa besides the lowest porosity of 16.5 % among all the tested composites.

I explain it with several factors mainly:

1. the effect of sintering process at 1400 °C which allowed the suppression of the minor agglomerations reported in the milled composites powder;
2. the optimum MWCNT concentration of 1 wt% enabled an average grain refinement to $0.96 \pm 0.49 \mu\text{m}$ as well as high interfacial bonding between the grains. Furthermore, the analysis of the

crack propagation modes showed the presence of MWCNT pull-out, crack bridging and crack deflections besides more restrained and tapered crack path in the 8YSZ /1 wt% composite compared to the reference. I showed that these toughening mechanisms played a vital role in enhancing the resistance to crack propagation. Quantitative X-rays measurements indicated the presence of considerable tetragonal phase at room temperature in the sintered composites with different proportions, unlike the composites powder in which the cubic phase was dominant. The highest proportion of tetragonal phase was obtained in the monolithic composites. This fact leads to enhanced Vickers hardness values (average ~13.49 GPa) due to the intrinsic property of transformation toughening zirconia. On the other hand, high degradation of the mechanical and Indentation Fracture Toughness was well approved in case of 5 wt% and 10 wt% MWCNTs addition. This was associated with incoherent and discontinuous matrix, reduced interfacial bonding due to the deep open pores on the surface which caused a long unrestrained crack path.

In the last part of my work, I investigated the influence of sliding speed on the tribological properties using Si_3N_4 balls, dry sliding conditions, low ($V_1= 0.036$ m/s) and high ($V_2= 0.11$ m/s) speed values. Outstanding wear improvement at both low/high sliding speed has been reported in case of 1 wt% of MWCNTs. This was most likely attributed to two main factors: 1. the formation of a perfectly continuous and uniform tribo-film; 2. the improved flexural strength and density. I developed the new interpretation of the observed wear mechanism in the studied 8YSZ ceramic composites with respect to MWCNTs content based on a comparative characterization performed inside and outside the wear track using SEM and EDS. Further, the steady state friction coefficient marked significant decrease at high sliding speed with 5 wt% and 10 wt% of MWCNTs content.

6. THESIS

The current investigation resulted into the novel founding summarized as follow:

1. I showed that the attrition milling and spark plasma sintering are appropriate technologies for production of well densified MWCNTs reinforced 8YSZ composites. I proved that the optimized wet milling conditions (4000 rotational speed for 5 hours, in ethanol) and sintering parameters (1400 °C, uniaxial pressure of 50 MPa, dwell time of 5 min, in vacuum) are needed

to achieve non-destructive MWCNT fibers in composites and to maintain the MWCNTs during the all steps of preparation process [1, 2].

2. I proved that the structural properties of final sintered composites are dependent on the amount of MWCNTs addition. The increasing of MWCNTs content from 1 wt% to 10 wt% led to a proportional grain refinement and to the formation of MWCNTs agglomeration.

I proved that the increasing MWCNTs addition resulted in a microstructure consisting of cubic zirconia (~33%), lower amount of monoclinic (m) (~3.5%) and higher amount of tetragonal phase (63.5%) considering the average values of ceramic phases. This fact demonstrates the role of MWCNTs addition to successfully synthesis metastable tetragonal (t) phase and to reduce t→m phase transformation during cooling stage of sintering [2].

3. I proved that only 1 wt% MWCNT addition improved the mechanical properties of final composites. I found that the hardness and indentation fracture toughness were mostly equal with reference, while the bending strength increased for 1 w% MWCNTs content. The structural factors responsible for this improvement are the good distribution of MWCNTs in ceramic matrix, the grain refinement to $0.96 \pm 0.49\mu\text{m}$ and high interfacial bonding among the grains resulting from the dominating transgranular fracture mode. In the case of 5 and 10 wt% MWCNTs addition, hardness and indentation fracture toughness showed lower values and fluctuated distribution characterized by intergranular fracture mode [2].

4. I developed a novel interpretation of the observed wear mechanism in the zirconia ceramic composites with respect to MWCNTs content based on a comparative characterization performed inside and outside the wear track. I showed an outstanding wear improvement of composite with 1 wt% MWCNTs at low (0.036 m/s) and high (0.11 m/s) sliding speeds attributed to the formation of a perfectly continuous, uniform tribofilm and the improved bending strength and density. Further, the steady state friction coefficient marked significant decrease at higher sliding speed with 5 and 10 wt% of MWCNTs content. In fact, this finding was mainly linked with intrinsic lubricant effect due to MWCNT exfoliation and the formation of a thick and dense tribofilm [3].

7. PUBLICATIONS

7.1 Publications related to the thesis

[1] **S. Lamnini**, Z. Fogarassy, Z.E. Horváth, S. Tóth, K. Balázs, C. Balázs, The role of the attrition milling on the grain size and distribution of the carbon nanotubes in YSZ powders, Bol. La Soc. Esp. Ceram. y Vidr. (2018) 126 - 133 (**IF 1.633**).

[2] **S. Lamnini**, Z. Károly, E. Bódis, K. Balázs, C. Balázs, Influence of structure on the hardness and the toughening mechanism of the sintered 8YSZ/MWCNTs composites, Ceram. Int. 45:4 (2019) 5058 - 5065 (**IF 3.450**).

[3] **S. Lamnini**, C. Balázs, K. Balázs, Wear mechanism of spark plasma sintered MWCNTs reinforced zirconia composites under dry sliding conditions, Wear. 430–431 (2019) 280-281 (**IF 2.950**).

7.2 Other publications

[4] **S. Lamnini**, P. Kádár, Survey on perspectives of PV technology and their applications. SAMI 2017 - IEEE 15th Int. Symp. Appl. Mach. Intell. Informatics, Proc., 2017.

7.3 Conferences

S. Lamnini, P. Kádár, Sami 2017Conference, 15th International Symposium on Applied Machine Intelligence and Informatics, 2017, January 26-28, Herlany, Slovakia. (Poster presentation)

S. Lamnini, Z. Fogarassy, Z.E. Horváth, K. Balazsi, C. Balazsi, ECerS 2017, 15th Conference & Exhibition of the European Ceramic Society, 2017, Július7-13, Budapest. (Poster presentation)

S. Lamnini, Z. Fogarassy, Z.E. Horváth, K. Balazsi, C. Balazsi, FEMS Junior EUROMAT 2018, The main Event for Young Material Scientists,2018, July8-12, Budapest. (Oral presentation)

S. Lamnini, Student speech context participation,16th Conference & Exhibition of the European Ceramic Society, 2019, June 16-20, Torino, Italy. (Oral presentation)

S. Lamnini, Z. Fogarassy, Z.E. Horváth, K. Balazsi, C. Balazsi, Woceram 2019, International workshop on Women in ceramic science, 2019, April 7-9, Budapest. (Oral presentation)

S. Lamnini, K. Balazsi, C. Balazsi, 1st “Fine ceramics day” event of Hungarian Scientific Society of Silicate Industry, 2018, 9 April, MTA EK, Budapest, Hungary. (Oral presentation)

S. Lamnini, Z. Károly, E. Bódis, K. Balázs, C. Balázs, 2nd “Fine ceramics day” event of Hungarian Scientific Society of Silicate Industry, 2019, 19 March, Budapest, Hungary. (Oral presentation)

S. Lamnini, Z. Fogarassy, Z.E. Horváth, K. Balazsi, C. Balazsi, 44th International Conference & Exposition on Advanced Ceramics & Composites (ICACC) and ACerS Winter workshop 2020, Jan 26–31, 2020, in Daytona Beach, Florida. (Poster presentation)

8. REFERENCES

- [1] M. Krupka, A. Kienzle, Fiber reinforced ceramic composite for brake discs, in: 18th Annu. Brake Colloq. Eng. Disp., 2000.
- [2] C.U. Hardwicke, Y.C. Lau, Advances in thermal spray coatings for gas turbines and energy generation: A review, *J. Therm. Spray Technol.* 22 (2013) 564–576.
- [3] Z. Cheng, M. Liu, Characterization of sulfur poisoning of Ni – YSZ anodes for solid oxide fuel cells using in situ Raman microspectroscopy, *Solid State Ionics.* 178 (2007) 925–935.
- [4] J. Silvestre, N. Silvestre, J. de Brito, An Overview on the Improvement of Mechanical Properties of Ceramics Nanocomposites, *J. Nanomater.* 2015 (2015) 1–13.
- [5] J.D. Kuntz, G. Zhan, A.K. Mukherjee, Nanocrystalline- Composites for Improved Fracture, *Mater. Res. Soc.* 29 (2004) 22–27.
- [6] Martin, Sternitzke, Review: Structural ceramic nanocomposites, *J. Eur. Ceram. Soc.* 17 (1997) 1061–1082.
- [7] Sumit, Pramanik, Ashis, Tripathy, Kamal, K. Kar, *Composite Materials: Processing, Applications, Characterizations*, 2017.
- [8] R. Porwal, H. Saggarr, Ceramic Matrix Nanocomposites, in: *Compr. Compos. Mater. II*, Elsevier Ltd., 2018: pp. 138–161.
- [9] Wu, H., Understanding residual stresses and fracture toughness in ceramic nanocomposites, in: *Residual Stress. Compos. Mater.*, 2014: pp. 256–292.
- [10] Sumio Iijima, Helical microtubules of graphitic carbon, *Lett. to Nat.* 354 (1991) 56–58.
- [11] Aqel Ahmad El-nour Abou M Kholoud M Ammar A A Reda, Al-warthan Abdulrahman, Carbon nanotubes , science and technology part (I) structure , synthesis and characterisation, *Arab. J. Chem.* 5 (2012) 1–23.
- [12] A. Navrotsky, Thermochemical insights into refractory ceramic materials based on oxides with large tetravalent cations, *J. Mater. Chem.* 15 (2005) 1883–1890.
- [13] I. Denry, J.R. Kelly, State of the art of zirconia for dental applications, *Dent. Mater.* 24 (2008) 299–307.
- [14] N.P. Padture, Thermal Barrier Coatings for Gas-Turbine Engine Applications, *Sci. Compass.* 296 (2002) 280–284.
- [15] Gebresilassie, Abel, Atomic scale simulations in zirconia : Effect of yttria doping and environment on stability of phases, Lyon University, 2017.
- [16] T. Vagkopoulou, S.O. Koutayas, P. Koidis, J.R. Strub, Zirconia in dentistry: Part 1. Discovering the nature of an upcoming bioceramic., *Eur. J. Esthet. Dent.* 4 (2009) 130–51.
- [17] R.H.J. Hannink, P.M. Kelly, B.C. Muddle, Transformation Toughening in Zirconia-Containing Ceramics, *J. Am. Ceram. Soc.* 83 (2004) 461–487.

- [18] D.R. Mumm, A.G. Evans, Mechanisms Controlling the Durability of Thermal Barrier Coatings, *Prog. Mater. Sci.* 46 (2001) 505–553.
- [19] C. Piconi, G. Maccauro, Review Zirconia as a ceramic biomaterial, *Biomaterials.* 20 (1999).
- [20] Li, Ping, Chen, -W, I-Wei, Penner-Hahn, E., James, Effect of Dopants on Zirconia Stabilization—An X-ray Absorption Study: I, Trivalent Dopants, *J. Am. Ceram. Soc.* 77 (1994) 1289–1295.
- [21] D.J. Green, R.H.J. Hannink, M. V Swain, Toughening, CRC Press Taylor & Francis Group, an Informa business, Boca Raton London New York, 1998.
- [22] H.G. Scott, Phase relationships in the zirconia-yttria system, *J. Mater. Sci.* 10 (1975) 1527–1535.
- [23] Y. Zhu, L. Shi, J. Liang, D. Hui, K. Lau, Synthesis of zirconia nanoparticles on carbon nanotubes and their potential for enhancing the fracture toughness of alumina ceramics, *Compos. Part B.* 39 (2008) 1136–1141.
- [24] R. Darolia, Thermal barrier coatings technology: critical review, progress update, remaining challenges and prospects, *Int. Mater. Rev.* 58 (2013) 315–348.
- [25] C. Mercer, J.R. Williams, D.R. Clarke, A.G. Evans, On a ferroelastic mechanism governing the toughness of metastable tetragonal-prime (t') yttria-stabilized zirconia, *Proc. R. Soc. A Math. Phys. Eng. Sci.* 463 (2007) 1393–1408.
- [26] E.P. Butler, Transformation-toughened zirconia ceramics, *Mater. Sci. Technol.* 1 (1985) 417–432.
- [27] G.M. WOLTEN, Diffusionless Phase Transformations in Zirconia and Hafnia, *J. Am. Ceram. Soc.* 46 (1963) 418–422.
- [28] B. Budiansky, J.W. Hutchinson, J.C. Lambropoulos, Continuum theory of dilatant transformation toughening in ceramics, *Int. J. Solids Struct.* 19 (1983) 337–355.
- [29] D.J. GREEN, P.S. NICHOLSON, J.D. EMBURY, Fracture Toughness of a Partially Stabilized ZrO₂ in the System CaO-ZrO₂, *J. Am. Ceram. Soc.* 56 (1973) 619–623.
- [30] A.G. EVANS, K.T. FABER, Crack-Growth Resistance of Microcracking Brittle Materials, *J. Am. Ceram. Soc.* 67 (1984) 255–260.
- [31] Z. Xiao, R.A. Kerner, L. Zhao, N.L. Tran, K.M. Lee, T.W. Koh, G.D. Scholes, B.P. Rand, Efficient perovskite light-emitting diodes featuring nanometre-sized crystallites, *Nat. Photonics.* 11 (2017) 108–115.
- [32] J.R. Kelly, I. Denry, Stabilized zirconia as a structural ceramic: An overview, *Dent. Mater.* 24 (2008) 289–298.
- [33] E.C. Subbarao, H.S. Maiti, K.K. Srivastava, Martensitic transformation in zirconia, *Phys. Status Solidi.* 21 (1974) 9–40.
- [34] P. Manning, The kinetics of oxygen transport in 9.5 mol % single crystal yttria stabilised zirconia, *Solid State Ionics.* 100 (2003) 1–10.

- [35] I. Kosacki, V. Petrovsky, H.U. Anderson, Modeling and characterization of electrical transport in oxygen conducting solid electrolytes, *J. Electroceramics*. 4 (2000) 243–249.
- [36] C. Haering, A. Roosen, H. Schichl, Degradation of the electrical conductivity in stabilised zirconia systems Part I: Ytria-stabilised zirconia, *Solid State Ionics*. 176 (2005) 253–259.
- [37] P.V. Mtsampas, F.Sapountzi, *Catalysis Science & Technology*, Catal. Sci. Technol. (2015).
- [38] R. Wang, J. Tao, B. Yu, Characterization of multiwalled carbon nanotube-polymethyl methacrylate composite resins as denture base materials, *J. Prosthet. Dent*. 111 (2014) 318–326.
- [39] M. Kumar, Y. Ando, Chemical Vapor Deposition of Carbon Nanotubes : A Review on Growth Mechanism and Mass Production, *J. Nanosci. Nanotechnol*. 10 (2010).
- [40] L. Melk, *Processing and Properties of Zirconia-CNT Composites*, Universitat Politecnica de Catalunya, 2016.
- [41] J. Cho, A.R. Boccaccini, M.S.P. Shaffer, Ceramic matrix composites containing carbon nanotubes, *J. Mater. Sci*. 44 (2009) 1934–1951.
- [42] Loos, Marcio, Production of CNTs and Risks to Health, in: *CNTs Risks to Heal. Safe Disposal*, *Environ. Concerns*, 2015: pp. 103–123.
- [43] P. Sharma, S. Sharma, D. Khanduja, On the Use of Ball Milling for the Production of Ceramic Powders, *Mater. Manuf. Process*. 30 (2015) 1370–1376.
- [44] A. Nieto, A. Bisht, D. Lahiri, C. Zhang, A. Agarwal, Graphene reinforced metal and ceramic matrix composites : a review, *Int. Mater. Rev*. 6608 (2016).
- [45] S. Decker, L. Krüger, Influence of high-energy ball milling on Mg-PSZ-reinforced TRIP steel-matrix composites synthesized by FAST / SPS, *Mater. Sci. Eng. A*. 761 (2019) 137974.
- [46] L.B. Kong, J. Ma, W. Zhu, O.K. Tan, Preparation and characterization of PLZT ceramics using high-energy ball milling, *J. Alloys Compd*. 322 (2001) 290–297.
- [47] J. Liu, H. Yan, M.J. Reece, K. Jiang, Toughening of zirconia/alumina composites by the addition of graphene platelets, *J. Eur. Ceram. Soc*. 32 (2012) 4185–4193.
- [48] K. Rajeswari, U.S. Hareesh, R. Subasri, D. Chakravarty, Comparative Evaluation of Spark Plasma (SPS), Microwave (MWS), Two stage sintering (TSS) and Conventional Sintering (CRH) on the densification and Micro structural Evolution of fully Stabilized Zirconia Ceramics, *Sci. Sinter*. 42 (2010) 259–267.
- [49] M.O.H.N.A.G.I. Ya, The effect of electric field and pressure on the synthesis and consolidation of materials : A review of the spark plasma sintering method, *J. Mater. Sci*. 41 (2006) 763–777.
- [50] K. Inoue, Electric-discharge sintering, 3 241 956, 1963.
- [51] O. Guillon, J. Gonzalez-Julian, B. Dargatz, T. Kessel, G. Schierning, J. Räthel, M. Herrmann, Field-assisted sintering technology/spark plasma sintering: Mechanisms,

- materials, and technology developments, *Adv. Eng. Mater.* 16 (2014) 830–849.
- [52] M. Suárez, A. Fernández, J.L. Menéndez, R. Torrecillas, H.U. Kessel, J. Hennicke, R. Kirchner, T. Kessel, Challenges and Opportunities for Spark Plasma Sintering: A Key Technology for a New Generation of Materials, *INTECH*. (2013) 25.
- [53] J.E. Garay, Z.A. Munir, Spark plasma sintering and characterization of bulk nanostructured fully stabilized zirconia : Part I . Densification studies, *J. Mater. Res.* 19 (2004) 3255–3262.
- [54] J.E. Garay, Z.A. Munir, Fast low-temperature consolidation of bulk nanometric ceramic materials, *Scr. Mater.* 54 (2006) 823–828.
- [55] P. Asoka-Kumar, K. O'Brien, K.G. Lynn, P.J. Simpson, K.P. Rodbell, Detection of current-induced vacancies in thin aluminum-copper lines using positrons, *Appl. Phys. Lett.* 68 (1995) 408.
- [56] G. Baldinozzi, A. Addad, Spark plasma sintering of a commercially available granulated zirconia powder — II . Microstructure after sintering and ionic conductivity, *ACTA Mater.* 56 (2008) 4658–4672.
- [57] G. Skandan, H. Hahn, B.H. Kear, M. Roddy, W.R. Cannon, The effect of applied stress on densification of nanostructured zirconia during sinter-forging, *Mater. Lett.* 20 (1994) 305–309.
- [58] W. Chen, J.E. Garay, J.R. Groza, Z.A. Munir, Fundamental investigations on the spark plasma sintering / synthesis process I . Effect of dc pulsing on reactivity, *Mater. Sci. Eng. A.* 394 (2005) 132–138.
- [59] K.D. Robles Arellano, L. Bichler, K. Akkiraju, R. Fong, K. Mondal, Densification behavior of Spark Plasma Sintered La₂O₃-YSZ ceramic composites, *Ceram. Int.* 40 (2014) 715–722.
- [60] M. Mazaheri, D. Mari, R. Schaller, G. Bonnefont, G. Fantozzi, Processing of yttria stabilized zirconia reinforced with multi-walled carbon nanotubes with attractive mechanical properties, *J. Eur. Ceram. Soc.* 31 (2011) 2691–2698.
- [61] A. Karanam, L. Bichler, R. Fong, On the Densification Behavior of (0.2, 0.5, and 1 Wt Pct) CNT-YSZ Ceramic Composites Processed via Spark Plasma Sintering, *Metall. Mater. Trans. B Process Metall. Mater. Process. Sci.* 46 (2015) 1666–1673.
- [62] D. Munz, T.Fett, *Ceramics Mechanical Properties, Failure Behaviour*, Material Section, Springer-Verlag Berlin Heidelberg GmbH, 1999.
- [63] H. Chandler, ed., *Hardness Testing*, 2nd ed., ASM International, 1999.
- [64] P.A. Sable, J. LaJeunesse, C. Sullivan, V. Kamavaram, J.P. Borg, Dynamic compaction of yttria-stabilized zirconia with the addition of carbon-nanotubes, *AIP Conf. Proc.* 1793 (2017) 1–7.
- [65] s.Timoshenko, J.. Goodier, *Theory of Elasticity*, 2nd ed., McGraw-Hill, United States of America, 1951.
- [66] J. Maynard, RESONANT ULTRASOUND, *Phys. Today.* 49 (1996) 26–31.

- [67] G.M. Guttman, Y. Gelbstein, *Mechanical Properties of Thermoelectric Materials for Practical Applications*, Intech open, 2018.
- [68] J. Wei, G. Pe, J. Malzbender, Review of mechanical characterization methods for ceramics used in energy technologies, *Ceram. Int.* 40 (2014) 15371–15380.
- [69] A. D2845-00, *Standard Test Method for Laboratory Determination of Pulse Velocities and Ultrasonic Elastic Constants of Rock*, ASTM International, West Conshohocken, PA, 2000.
- [70] C. Aksel, F.L. Riley, Young ' s modulus measurements of magnesia – spinel composites using load – deflection curves , sonic modulus , strain gauges and Rayleigh waves, *J. Eur. Ceram. Soc.* 23 (2003) 3089–3096.
- [71] N. Mahato, A. Nisar, P. Mohapatra, S. Rawat, S. Ariharan, K. Balani, N. Mahato, A. Nisar, P. Mohapatra, S. Rawat, S. Ariharan, Effect of far-field stresses and residual stresses incorporation in predicting fracture toughness of carbon nanotube reinforced yttria stabilized zirconia, *J. Appl. Phys.* 122 (2017).
- [72] A. Gallardo-lópez, I. Márquez-abril, A. Morales-rodíguez, A. Muñoz, Dense graphene nanoplatelet / yttria tetragonal zirconia composites : Processing , hardness and electrical conductivity, *Ceram. Int.* (2017) 0–1.
- [73] A.M. Zahedi, J. Javadpour, H.R. Rezaie, M. Mazaheri, Analytical study on the incorporation of zirconia-based ceramics with carbon nanotubes: Dispersion methods and mechanical properties, *Ceram. Int.* 42 (2016) 1653–1659.
- [74] L. Melk, M. Antti, M. Anglada, Material removal mechanisms by EDM of zirconia reinforced MWCNT nanocomposites, *Ceram. Int.* 42 (2016) 5792–5801.
- [75] J. Xu, Y. Bai, W. Wang, S. Wang, F. Han, Y. Qi, J. Bi, Toughening and reinforcing zirconia ceramics by introducing boron nitride nanotubes, *Mater. Sci. Eng. A.* 546 (2012) 301–306.
- [76] A. Duszová, J. Dusza, K. Tomášek, J. Morgiel, G. Blugan, J. Kuebler, Zirconia / carbon nanofiber composite, *Scr. Mater.* 58 (2008) 520–523.
- [77] J. Ping, Q. Ming, K. Yi, J. Jun, The effects of multiwalled carbon nanotubes on the hot-pressed 3 mol % yttria stabilized zirconia ceramics, *Mater. Sci. Eng. A.* 520 (2009) 153–157.
- [78] N. Garmendia, S. Grandjean, J. Chevalier, L.A. Diaz, R. Torrecillas, I. Obieta, Zirconia-multiwall carbon nanotubes dense nano-composites with an unusual balance between crack and ageing resistance, *J. Eur. Ceram. Soc.* 31 (2011) 1009–1014.
- [79] Gelbstein, Tmann, Yaniv, Additional, G.M.G. and Y. Gelbstein, *Mechanical Properties of Thermoelectric Materials for Practical Applications*, in: *Bringing Thermoelectr. into Real.*, 2018: p. 78.
- [80] R. Danzer, T. Lube, R. Morrell, P. Supancic, *Mechanical Properties of Ceramics*, Second Edi, Elsevier, 2013.
- [81] F. Sergejev, M. Antonov, Comparative study on indentation fracture toughness measurements of cemented carbides, *Proc. Est. Acad. Sci. Eng.* 12 (2006) 388–398.

- [82] S. Sheikh, R. M'Saoubi, P. Flasar, M. Schwind, T. Persson, J. Yang, L. Llanes, Fracture toughness of cemented carbides: Testing method and microstructural effects, *Int. J. Refract. Met. Hard Mater.* 49 (2015) 153–160.
- [83] D.K. Shetty, I.G. Wright, P.N. Mincer, A.H. Clauer, Indentation fracture of WC-Co cermets, *J. Mater. Sci.* 20 (1985) 1873–1882.
- [84] T. Aleksandrov Fabijanić, D. Ćorić, M. Šnajdar Musa, M. Sakoman, Vickers Indentation Fracture Toughness of Near-Nano and Nanostructured WC-Co Cemented Carbides, *Metals (Basel)*. 7 (2017) 143.
- [85] Norman E. DOWLING, *Mechanical Behavior of Materials Engineering Methods for Deformation, Fracture, and Fatigue*, 4th ed., International Edition, London, 2012.
- [86] K.J. Anderson, Hardness Testing, *MRS Bull.* 19 (1994) 76–77.
- [87] Y.P. Li, X.F. Zhu, G.P. Zhang, J. Tan, W. Wang, B. Wu, Investigation of deformation instability of Au/Cu multilayers by indentation, *Philos. Mag.* 90 (2010) 3049–3067.
- [88] P. Zhang, S.X. Li, Z.F. Zhang, General relationship between strength and hardness, *Mater. Sci. Eng. A.* 529 (2011) 62–73.
- [89] N. Cuadrado, D. Casellas, L. Llanes, I. González, J. Caro, Effect of crystal anisotropy on the mechanical properties of WC-Co cemented carbides., *Proc. Euro PM2011 Powder Metall. Congr. Exhib.* (2011).
- [90] M. Sebastiani, K.E. Johanns, E.G. Herbert, G.M. Pharr, Measurement of fracture toughness by nanoindentation methods: Recent advances and future challenges, *Curr. Opin. Solid State Mater. Sci.* 19 (2015) 324–333.
- [91] G.D. Quinn, Fracture Toughness of Ceramics By the Vickers Indentation Crack, *Ceram. Eng. Sci. Proc.* (2006) 1–18.
- [92] R.F. Cook, G.M. Pharr, Direct Observation and Analysis of Indentation Cracking in Glasses and Ceramics, *J. Am. Ceram. Soc.* 73 (1990) 787–817.
- [93] T. Lube, Indentation crack profiles in silicon nitride, *J. Eur. Ceram. Soc.* 21 (2001) 211–218.
- [94] J.T. Hagan, M. V. Swain, The origin of median and lateral cracks around plastic indents in brittle materials, *J. Phys. D Appl. Phys.* 11 (1978) 2091–2102.
- [95] J. Liu, H. Guo, Y. Su, L. Wang, L. Wei, G. Yang, Y. Yang, K. Jiang, Spark plasma sintering of graphene platelet reinforced zirconia composites with improved mechanical performance, *Mater. Sci. Eng. A.* 688 (2017) 70–75.
- [96] J. Zimmer, D. Klein, M. Stommel, Experimental and Numerical Analysis of Liquid-Forming, *Key Eng. Mater.* 651–653 (2015) 842–847.
- [97] M.S. Kaliszewski, G. Behrens, A.H. Heuer, M.C. Shaw, D.B. Marshall, G.W. Dransmanri, R.W. Steinbrech, A. Pajares, F. Guiberteau, F.L. Cumbreira, A. Dominguez-Rodriguez, Indentation Studies on Y2O2-Stabilized ZrO2: I, Development of Indentation-Induced Cracks, *J. Am. Ceram. Soc.* 77 (1994) 1185–1193.

- [98] K.M. Liang, G. Orange, G. Fantozzi, Evaluation by indentation of fracture toughness of ceramic materials, *J. Mater. Sci.* 25 (1990) 207–214.
- [99] F.X. Xie, D. Zhang, H. Su, X. Ren, K.S. Wong, M. Grätzel, W.C.H. Choy, Vacuum-assisted thermal annealing of $\text{CH}_3\text{NH}_3\text{PbI}_3$ for highly stable and efficient perovskite solar cells, *ACS Nano.* 9 (2015) 639–646.
- [100] Hansen, J., James, Cutler., A., Raymond, Shetty, K., Virkar, V., Indentation Fracture Response and Damage Resistance of $\text{Al}_2\text{O}_3\text{-ZrO}_2$, Composites Strengthened by Transformation-Induced Residual Stresses, *Am. Ceram. Soc.* 71 (1988) 501–505.
- [101] F. Striations, S. Behavior, Fatigue of Yttria-Stabilized Zirconia: II, Crack Propagation, Fatigue Striations, and Short-Crack Behavior, *J Am Ceram Soc.* 16 (1991) 1206–16.
- [102] V.M. Sglavo, P. Pancheri, Crack decorating technique for fracture-toughness measurement in Alumina, *J. Eur. Ceram. Soc.* 17 (1997) 1697–1706.
- [103] J. Lankford, Threshold microfracture during elastic-plastic indentation of ceramics, *J. Mater. Sci.* 16 (1981) 1177–1182.
- [104] R.L.K. Matsumoto, Evaluation of Fracture Toughness Determination Methods as Applied to Ceria-Stabilized Tetragonal Zirconia Polycrystal, *J. Am. Ceram. Soc.* 70 (2005) C-366-C-368.
- [105] S.L. Jones, C.J. Norman, R. Shahani, Crack-profile shapes formed under a Vickers indent pyramid, *J. Mater. Sci. Lett.* 6 (1987) 721–723.
- [106] A. G. EVANS* and E. A. CHARLES, Fracture Toughness Determinations by Indentation, *Am. Ceram. Soc.* 59 (1976) 7–8.
- [107] D. Marshall, B.R. Lawn, A. Evans, Elastic/Plastic Indentation Damage in Ceramics: The Median/Radial Crack System, *J. Am. Ceram. Soc.* 65 (1982) 561–566.
- [108] Antis, G.R., P.Chantikul, Lawn, B.R., Marsall, B., D., A Critical Evaluation of Indentation Techniques for Measuring Fracture Toughness: I, Direct Crack Measurements, *Am. Ceram. Soc.* 64 (1981) 533–538.
- [109] A. V. Shatov, S.S. Ponomarev, S.A. Firstov, Fracture and Strength of Hardmetals at Room Temperature, *Compr. Hard Mater.* 1 (2014) 301–343.
- [110] B.W. Krenkel, B. Heidenreich, R. Renz, C / C-SiC Composites for Advanced Friction Systems, *Adv. Eng. Mater.* 4 (2002) 427–436.
- [111] M.K. Surappa, Aluminium matrix composites: Challenges and opportunities, *Sadhana - Acad. Proc. Eng. Sci.* 28 (2003) 319–334.
- [112] W. Krenkel, F. Berndt, C/C-SiC composites for space applications and advanced friction systems, *Mater. Sci. Eng. A.* 412 (2005) 177–181.
- [113] Y. Liang, S.P. Dutta, Application trend in advanced ceramic technologies, *Technovation.* 21 (2001) 61–65.
- [114] T.R. Chapman, D.E. Niesz, R.T. Fox, T. Fawcett, Wear-resistant aluminum-boron-carbide

- cermets for automotive brake applications, *Wear*. 236 (1999) 81–87.
- [115] A. Kasperski, A. Weibel, D. Alkattan, C. Estournès, V. Turq, C. Laurent, A. Peigney, Microhardness and friction coefficient of multi-walled carbon nanotube-yttria-stabilized ZrO₂ composites prepared by spark plasma sintering, *Scr. Mater.* 69 (2013) 338–341.
- [116] P. Hvizdoš, J. Dusza, C. Balázs, Tribological properties of Si₃N₄-graphene nanocomposites, *J. Eur. Ceram. Soc.* 33 (2013) 2359–2364.
- [117] L. Melk, J.J.R. Rovira, M.L. Antti, M. Anglada, Coefficient of friction and wear resistance of zirconia-MWCNTs composites, *Ceram. Int.* 41 (2014) 459–468.
- [118] P. Hvizdoš, V. Puchý, A. Duszová, J. Dusza, Tribological behavior of carbon nanofiber-zirconia composite, *Scr. Mater.* 63 (2010) 254–257.
- [119] X. Xu, *Ceramics in solid oxide fuel cells for energy generation*, *Adv. Ceram. Matrix Compos. Second Ed.* (2018) 763–788.
- [120] C.S. Spiegel, *Designing & building fuel cells*, 1st ed., McGraw-Hill Education, New York, 2007.
- [121] E.D. Wachsman, K.T. Lee, Review Lowering the Temperature of Solid, *Science* (80-.). 334 (2011) 935–940.
- [122] N. Laosiripojana, S. Assabumrungrat, Catalytic steam reforming of methane, methanol, and ethanol over Ni/YSZ: The possible use of these fuels in internal reforming SOFC, *J. Power Sources*. 163 (2007) 943–951.
- [123] T. Aloui, K. Halouani, Analytical modeling of polarizations in a solid oxide fuel cell using biomass syngas product as fuel, *Appl. Therm. Eng.* 27 (2007) 731–737.
- [124] A. Alaswad, *Fuel Cell Technologies, Applications, and State of the Art . A Reference Guide*, in: *Ref. Modul. Mater. Sci. Mater. Eng.*, Elsevier Ltd., 2016: pp. 1–18.
- [125] G. Cacciola, V. Antonucci, S. Freni, Technology up date and new strategies on fuel cells, *J. Power Sources*. 100 (2001) 67–79.
- [126] M. Liu, D. Dong, R. Peng, J. Gao, J. Diwu, X. Liu, G. Meng, YSZ-based SOFC with modified electrode/electrolyte interfaces for operating at temperature lower than 650 °C, *Appl. Catal. A Gen.* 180 (2008) 215–220.
- [127] S.P. Jiang, Y.Y. Duan, J.G. Love, Fabrication of High-Performance Ni/Y₂O₃-ZrO₂ Cermet Anodes of Solid Oxide Fuel Cells by Ion Impregnation, *J. Electrochem. Soc.* 149 (2002) A1175.
- [128] H. Koide, Y. Someya, T. Yoshida, T. Maruyama, Properties of Ni / YSZ cermet as anode for SOFC, *Solid State Ionics*. 132 (2000) 253–260.
- [129] E.S. Hecht, G.K. Gupta, H. Zhu, A.M. Dean, R.J. Kee, L. Maier, O. Deutschmann, Methane reforming kinetics within a Ni – YSZ SOFC anode support, *Appl. Catal. A Gen.* 295 (2005) 40–51.
- [130] G. Goula, V. Kioussis, L. Nalbandian, I. V Yentekakis, Catalytic and electrocatalytic

- behavior of Ni-based cermet anodes under internal dry reforming of CH₄ + CO₂ mixtures in SOFCs, *Solid State Ionics*. 177 (2006) 2119–2123.
- [131] T. Takeguchi, R. Kikuchi, T. Yano, Effect of precious metal addition to Ni-YSZ cermet on reforming of CH₄ and electrochemical activity as SOFC anode, *Catal. Today*. 84 (2003) 217–222.
- [132] M. Shirjeel, S. Lee, R. Song, J. Lee, T. Lim, S. Park, Fundamental mechanisms involved in the degradation of nickel – yttria stabilized zirconia (Ni – YSZ) anode during solid oxide fuel cells operation : A review, *Ceram. Int.* 42 (2016) 35–48.
- [133] M. Tanhaei, M. Mozammel, Yttria-stabilized zirconia thin film electrolyte deposited by EB-PVD on porous anode support for SOFC applications, *Ceram. Int.* (2016).
- [134] Y.L. Liu, A. Hagen, R. Barfod, M. Chen, H.J. Wang, F.W. Poulsen, P. V Hendriksen, Microstructural studies on degradation of interface between LSM – YSZ cathode and YSZ electrolyte in SOFCs, *Solid State Ionics*. 180 (2009) 1298–1304.
- [135] J. Cho, J. Park, J. An, Low thermal conductivity of atomic layer deposition yttria-stabilized zirconia (YSZ) thin films for thermal insulation applications, *J. Eur. Ceram. Soc.* 37 (2017) 3131–3136.
- [136] X. Ren, M. Zhao, J. Feng, W. Pan, Phase transformation behavior in air plasma sprayed yttria stabilized zirconia coating, *J. Alloys Compd.* 750 (2018) 189–196.
- [137] C.U. Hardwicke, Y. Lau, Advances in Thermal Spray Coatings for Gas Turbines and Energy Generation : A Review, *J. Therm. Spray Technol.* 22 (2013) 564–576.
- [138] B. Berger, The Importance and Testing of Density / Porosity / Permeability / Pore Size for Refractories, in: *South. African Inst. Min. Metall. Refract.*, 2010: pp. 111–116.
- [139] S.A.R. Junior, J.L. Ferracane, Á. Della Bona, Flexural strength and Weibull analysis of a microhybrid and a nanofill composite evaluated by 3- and 4-point bending tests, *Dent. Mater.* 24 (2008) 426–431.
- [140] L. Vandewalle, Recommendations of RILEM TC 162-TDF: Test and design methods for steel fibre reinforced concrete, *Mater. Struct. Constr.* 33 (2000) 3–5.
- [141] P. Hou, H. Zhao, Z. Ma, S. Zhang, J. Li, X. Dong, Y. Sun, Z. Zhu, Influence of punch radius on elastic modulus of three-point bending tests, *Adv. Mech. Eng.* 8 (2016) 1–8.
- [142] K.D. Vernon-Parry, Microscopy : an introduction, *Analysis*. 13 (2000) 40–44.
- [143] M.A. Sutton, N. Li, D.C. Joy, A.P. Reynolds, X. Li, Scanning electron microscopy for quantitative small and large deformation measurements Part I: SEM imaging at magnifications from 200 to 10,000, *Exp. Mech.* 47 (2007) 775–787.
- [144] W. Zhou, R. Apkarian, Z.L. Wang, D. Joy, Fundamentals of scanning electron microscopy (SEM), *Scanning Microsc. Nanotechnol. Tech. Appl.* (2007) 1–40.
- [145] D.A. Moncrieff, P.R. Barker, Secondary electron emission in the scanning electron microscope, *J. Appl. Phys.* 55 (1983) 195–197.

- [146] J.D. Jain, An Introduction To Electron Microscope, IETE J. Educ. 18 (2015) 65–82.
- [147] D.J. Barber, Transmission Electron Microscopy. Physics of Image Formation and Microanalysis, Opt. Acta Int. J. Opt. 31 (2007) 848–848.
- [148] D.B. Williams, C.B. Carter, 5th, Transmission Electron Microscopy: A Textbook For Materials Science : Basics, Diffraction, Imaging, Spectrometry, (2008) 95.
- [149] A.K. Chatterjee, Handbook of Analytical Techniques in Concrete Science and Technology, Handb. Anal. Tech. Concr. Sci. Technol. (2001) 275–332.
- [150] J. Epp, X-Ray Diffraction (XRD) Techniques for Materials Characterization, in: Mater. Charact. Using Nondestruct. Eval. Methods, Elsevier Ltd, 2016: pp. 81–124.
- [151] H. Toraya, Introduction to X-ray analysis using the diffraction method, Rigaku J. 32 (2016) 35–43.
- [152] D.K. Smith, G.G. Johnson, A. Scheible, A.M. Wims, J.L. Johnson, G. Ullmann, Quantitative X-Ray Powder Diffraction Method Using the Full Diffraction Pattern, Powder Diffr. 2 (1987) 73–77.
- [153] W.E. Smith and G. Dent, Modern Raman Spectroscopy – A Practical Approach, John Wiley & Sons, 2005.
- [154] S. Lamnini, Z. Fogarassy, Z.E. Horváth, S. Tóth, K. Balázs, C. Balázs, The role of the attrition milling on the grain size and distribution of the carbon nanotubes in YSZ powders, Bol. La Soc. Esp. Ceram. y Vidr. (2018) 1–8.
- [155] L. Melk, J.J. Roa Rovira, F. García-Marro, M.L. Antti, B. Milsom, M.J. Reece, M. Anglada, Nanoindentation and fracture toughness of nanostructured zirconia/multi-walled
- [156] A. Gallardo-López, A. Morales-Rodríguez, J. Vega-Padillo, R. Poyato, A. Muñoz, A. Domínguez-Rodríguez, Enhanced carbon nanotube dispersion in 3YTZP/SWNTs composites and its effect on room temperature mechanical and electrical properties, J. Alloys Compd. 682 (2016) 70–79.
- [157] A. Duszová, J. Dusza, K. Tomášek, J. Morgiel, G. Blugan, J. Kuebler, Zirconia/carbon nanofiber composite, Scr. Mater. 58 (2008) 520–523.
- [158] A. Duszová, J. Dusza, K. Tomášek, G. Blugan, J. Kuebler, Microstructure and properties of carbon nanotube/zirconia composite, J. Eur. Ceram. Soc. 28 (2008) 1023–1027.
- [159] A. Ghosh, A.K. Suri, M. Pandey, S. Thomas, T.R. Rama Mohan, B.T. Rao, Nanocrystalline zirconia-yttria system—a Raman study, Mater. Lett. 60 (2006) 1170–1173.
- [160] J. Cai, Y.S. Raptis, E. Anastassakis, Stabilized cubic zirconia: A Raman study under uniaxial stress, Appl. Phys. Lett. 62 (1993) 2781–2783.
- [161] L. Bokobza, J. Zhang, Raman spectroscopic characterization of multiwall carbon nanotubes and of composites, Express Polym. Lett. 6 (2012) 601–608.
- [162] M.S. Dresselhaus, G. Dresselhaus, R. Saito, A. Jorio, Raman spectroscopy of carbon nanotubes, Phys. Rep. 409 (2005) 47–99.

- [163] E. Bódis, I. Cora, C. Balázsi, P. Németh, Z. Károly, S. Klébert, P. Fazekas, A.M. Keszler, J. Szépvölgyi, Spark plasma sintering of graphene reinforced silicon carbide ceramics, *Ceram. Int.* 43 (2017) 9005–9011.
- [164] E.F. Antunes, A.O. Lobo, E.J. Corat, V.J. Trava-Airoldi, A.A. Martin, C. Veríssimo, Comparative study of first- and second-order Raman spectra of MWCNT at visible and infrared laser excitation, *Carbon N. Y.* 44 (2006) 2202–2211.
- [165] G. Pezzotti, A.A. Porporati, Raman spectroscopic analysis of phase-transformation and stress patterns in zirconia hip joints, *J. Biomed. Opt.* 9 (2004) 372.
- [166] S.N. Basahel, T.T. Ali, M. Mokhtar, K. Narasimharao, Influence of crystal structure of nanosized ZrO₂ on photocatalytic degradation of methyl orange, *Nanoscale Res. Lett.* 10 (2015).
- [167] I. Akin, Investigation of the microstructure, mechanical properties and cell viability of zirconia-toughened alumina composites reinforced with carbon nanotubes, *J. Ceram. Soc. Japan.* 123 (2015) 405–413.
- [168] M. Michálek, J. Sedláček, M. Parchoviansky, M. Michálková, D. Galusek, Mechanical properties and electrical conductivity of alumina/MWCNT and alumina/zirconia/MWCNT composites, *Ceram. Int.* 40 (2014) 1289–1295.
- [169] J.H. Shin, S.H. Hong, Fabrication and properties of reduced graphene oxide reinforced yttria-stabilized zirconia composite ceramics, *J. Eur. Ceram. Soc.* 34 (2014) 1297–1302.
- [170] A. Kasperski, A. Weibel, D. Alkattan, C. Estournès, C. Laurent, A. Peigney, Double-walled carbon nanotube/zirconia composites: Preparation by spark plasma sintering, electrical conductivity and mechanical properties, *Ceram. Int.* 41 (2015) 13731–13738.
- [171] N. Mahato, A. Nisar, P. Mohapatra, S. Rawat, S. Ariharan, K. Balani, Effect of far-field stresses and residual stresses incorporation in predicting fracture toughness of carbon nanotube reinforced yttria stabilized zirconia, *J. Appl. Phys.* 122 (2017).
- [172] J.P. Zhou, Q.M. Gong, K.Y. Yuan, J.J. Wu, Y. fang Chen, C.S. Li, J. Liang, The effects of multiwalled carbon nanotubes on the hot-pressed 3 mol% yttria stabilized zirconia ceramics, *Mater. Sci. Eng. A.* 520 (2009) 153–157.
- [173] A. Celli, A. Tucci, L. Esposito, C. Palmonari, Fractal analysis of cracks in alumina-zirconia composites, *J. Eur. Ceram. Soc.* 23 (2003) 469–479.
- [174] K. Makarian, S. Santhanam, Z.N. Wing, Coefficient of thermal expansion of particulate composites with ceramic inclusions, *Ceram. Int.* 42 (2016) 17659–17665.
- [175] W. Wu, Z. Xie, W. Xue, L. Cheng, Toughening effect of multiwall carbon nanotubes on 3Y-TZP zirconia ceramics at cryogenic temperatures, *Ceram. Int.* 41 (2015) 1303–1307.
- [176] E. Cui, J. Zhao, X. Wang, J. Sun, X. Huang, C. Wang, Microstructure and toughening mechanisms of Al₂O₃/(W, Ti)C/graphene composite ceramic tool material, *Ceram. Int.* 44 (2018) 13538–13543.
- [177] D. McNamara, P. Alveen, D. Carolan, N. Murphy, A. Ivanković, Micromechanical Study

- of Strength and Toughness of Advanced Ceramics, *Procedia Mater. Sci.* 3 (2014) 1810–1815.
- [178] S. Lamnini, Z. Károly, E. Bódis, K. Balázs, C. Balázs, Influence of structure on the hardness and the toughening mechanism of the sintered 8YSZ/MWCNTs composites, *Ceram. Int.* (2018) 0–1.
- [179] INTERNATIONAL STANDARD, 23146, ISO, Fine ceramics (advanced ceramics, advanced technical ceramics) — Test methods for fracture toughness of monolithic ceramics — Single-edge V-notch beam (SEVNB) method, 1st ed., ISO, 2008.
- [180] ISO18756:2003(E), Fine Ceramics (Advanced Ceramics, Advanced Technical Ceramics) — Determination of Fracture Toughness of Monolithic Ceramics at Room Temperature by The Surface Crack in Flexure (SCF) Method, 2005 (2003) 1–36.
- [181] Y. Optaha, O.I.D.E. Normalisation, International standard, 2003 (2015).
- [182] A. Nieto, J.M. Zhao, Y.H. Han, K.H. Hwang, J.M. Schoenung, Microscale tribological behavior and in vitro biocompatibility of graphene nanoplatelet reinforced alumina, *J. Mech. Behav. Biomed. Mater.* 61 (2016) 122–134.
- [183] S. Lamnini, C. Balázs, K. Balázs, Wear mechanism of spark plasma sintered MWCNTs reinforced zirconia composites under dry sliding conditions, *Wear.* 430–431 (2019).
- [184] Li, Hongqing, Xie, Youtao, Li, Kai, Huang, Liping, Huang, Shansong, Zhao, Bizeng, Zheng, Xuebin, Microstructure and wear behavior of graphene nanosheets-reinforced zirconia coating Hongqing, *Ceram. Int.* (2014).
- [185] C. Zhang, A. Nieto, A. Agarwal, Ultrathin graphene tribofilm formation during wear of Al₂O₃–graphene composites, *Nanomater. Energy.* 5 (2016) 1–9.